Modeling and Control of Liquid Crystal Elastomer Based Soft Robots

Jundong Wu

A Thesis
In the Department
of
Mechanical & Industrial Engineering

Presented in Partial Fulfilment of Requirements
For the Degree of
Doctor of Philosophy (Mechanical Engineering) at
Concordia University
Montreal, Quebec, Canada

Septemper 2021

Abstract

Modeling and Control of Liquid Crystal Elastomer Based Soft Robots

Jundong Wu, Ph.D.

Concordia University, 2021

Soft robots are robotic systems which are inherently compliant, and can exhibit body deformation in normal operations. This type of systems has unprecedented advantage over rigid-body robots since they can mimic biological systems to perform a series of complicated tasks, work in confined spaces, and interact with the environment much more safely. Usually, the soft robots are composed of subsystems including the actuator, the sensor, the driving electronics, the computation system, and the power source. In these subsystems, the actuator is of great importance. This is because in most situations the actuator works to carry out the operations of the soft robot. It decides the functionalities and physical features of the whole system. Meanwhile, other subsystems work to aid the successful functioning of the actuator. Thus, the study on soft robot actuators, especially the modeling and control of soft robot actuators is the key to soft robot applications.

However, characteristics of soft robot actuators vary greatly due to the usage of different actuator materials. These materials include the variable length tendons, rubbers, smart materials, etc.. Among these different materials, smart material based actuators have the advantage of fast response, light weight, and can respond to various types of external stimuli such as electrical signal, magnetic signal, light, heat, etc.. As a result, smart material based actuators have been studied widely for possible soft robot applications.

Recent years, among smart materials, the liquid crystal elastomer (LCE) starts to catch researchers' attention. LCE is a type of smart material which can deform under the stimulation of light. Unlike conventional actuators, the LCE actuator can be separated from the power source, suggesting a simpler and lighter design, possible for applications that are total-

ly different from conventional electro-driven or magneto-driven actuators. However, just like other smart materials, the deformation characteristics of the LCE actuator exhibits a complicated hysteretic behavior highly dependent on environmental factors, which brings difficulty to the modeling and control. Furthermore, the deformation of the photo-responsive LCE actuator is a multi-step process, resulting greater inaccuracy when compared with conventional smart material based actuators. These are huge challenges that need to be overcome for the modeling and control of the LCE actuator, which is still in its preliminary stage.

This dissertation aims to develop suitable modeling and control strategies for the photo-responsive LCE actuator with the purpose of using it in soft robot applications. Here, by looking into the physical nature of the light-induced deformation of the LCE actuator, it can be concluded that LCE's deformation is inherently the macroscopic shape change resulted from the microscopic phase change of LCE molecules. Based on this deformation mechanism, an experimental platform including a computer, an I/O module, a programmable laser, the LCE actuator, a thermal camera, and a laser distance sensor is established to study the modeling and control of the photo-responsive LCE actuator. Experiments are performed and the results show that the deformation characteristics of the LCE actuator indeed exhibit obvious hysteresis, which is dependent on environmental factors.

Based on the deformation mechanism of LCE, basic modeling scheme and positioning control scheme for the photo-responsive LCE actuator are established. For the modeling of the LCE actuator, the goal is to obtain its temperature-deformation relationship and describe the hysteresis with small errors. Here, the average order parameter is introduced to give a quantitative description of the macroscopic average phase of LCE molecules. Then, the key to obtain the temperature-deformation relationship is to first find the relationship between the temperature of the LCE actuator and the average order parameter, and then find the relationship between the average order parameter and the macroscopic deformation. The overall model is the combination of the above two relationships.

According to this modeling scheme, a basic physical model for the photo-responsive LCE actuator is established. This model aims to develop a quantitative model that reflects the ac-

tual physics of the LCE actuator. By assuming that the phase transition of LCE molecules is under dynamic equilibrium at each specific moment, a simple analytical relationship between the temperature and deformation of the LCE actuator can be obtained. For this model, the Landau-de Gennes expansion of free energy for nematic LCEs is utilized to calculate the average order parameter. First, under the above assumption, the relationship between the temperature and the average order parameter is obtained. Meanwhile, thermal dynamic analysis gives the relationship between the average order parameter and the deformation. The above two relationships are then combined together to give the overall model. Model parameters are calculated based on nonlinear least squares method. Experimental results show that this model works to give a good prediction of the deformation characteristics.

Based on the above basic model, an improved model is then established to give a more detailed description on the hysteresis by considering the actual dynamic process of the phase transition of LCE molecules. In order to reflect the actual dynamic process, a small variation of the temperature is considered, and the corresponding number of LCE molecules that undergo phase transition is calculated based on thermal dynamic analysis and a polynomial expansion of the transition rate. As a result, a dynamic equation that gives the temperature-deformation relationship is obtained. To obtain the values of model parameters with efficiency, a two-step parameter identification method based on the differential evolution algorithm and nonlinear least squares method is established. Experiments show that the improved model can describe the hysteretic deformation characteristic of the photo-responsive LCE actuator with high accuracy.

Meanwhile, based on the physical nature of the LCE actuator, the positioning control of the photo-responsive LCE actuator is studied. Analysis on the deformation of the LCE actuator from the energy perspective shows that the positioning control of the photo-responsive LCE actuator is a multi-step process, which brings difficulties in control accuracy. To reduce the positioning control errors, a double closed-loop control structure with a feed-forward module is designed for the positioning control of the photo-responsive LCE actuator. Utilizing positioning control scheme together with the developed models, controllers are designed

for the positioning control of the photo-responsive LCE actuator. For the proposed double-closed loop structure, the inner loop uses a PID controller to control the temperature of the LCE actuator, the parameters of the inner loop controller are tuned using a stimulation-experiment combined method based on the Hammerstein-Wiener model. Meanwhile, the outer loop consists of a PID controller and a feed-forward controller, the feed-forward controller is a numerical inverse model of the simple physical model that is established in the modeling part, and calculates the target temperature for the inner loop based on the positioning control objective. Parameters of the outer loop controller are directly tuned through experiments. Based on the proposed control strategy, experiments with different control targets are carried out to prove that the proposed controller can achieve the positioning control target with high accuracy. Comparison experiments also show that the proposed double closed-loop structure is faster in response, and has smaller control errors than conventional single closed-loop control structure.

In the end, design guidelines for LCE based soft robots are discussed from the application perspective. Designs of a two-legged walking robot and a light-controlled rolling robot based on the photo-responsive LCE actuator are introduced, conclusions are made together with possible working directions for future studies.

Acknowledgement

Plain words are never enough to express a heart filled with gratitude, but I would still like to take some time to express my appreciation for those who have crossed on my path of pursuing the Ph.D degree. Thank you all.

First of all, I want to say thank you to my supervisor, Dr. Chun-Yi Su. It was him who brought me to the path I'm walking on right now, and it was him who has always been like a guiding star that shines above. I'm always inspired by his share of insightful wisdom, and I'm always encouraged by his delightful personality. He has taught me to learn, to discover, to think deeply, and to live a meaningful life. Thank you, grateful to have you.

I also want to say thank you to my parents, for their love and support on my study in a foreign country. If Dr. Su is the star ahead of my path, then my parents are always the solid that gives me courage. I will never feel lonely carrying wishes from the family, and every single word from you two will become the power that push me forward, forward, forward...but it doesn't hurt to stop for a while and look back to say, thank you, lucky to have you.

I want to thank my colleagues, Dr. Wenjun Ye, he is always there to share the thoughts and answer my doubts. Dr. Yawu Wang, his attitude toward life always gives me inspirations. Dr. Yaowei Wang, his optimism always inspires me to look forward. And Dr. Pan Zhang, Dr. Qun Lu, Dr. Tao Peng, Dr. Yilong Zhang, Mr. Fan... There are so many people to be thankful to. Thank you all, grateful to have you.

Three years might be long for a person who is on his own outside his original country. But for me, it's not. Thanks to everyone that I have encountered, thanks to the moments that we share, the words of care. Thank you, great to have you all.

Contents

List of Figures

List of Tables

Nomenclature

n	average order direction
P	laser power efficiency
T	temperature of the liquid crystal elastomer actuator
d	displacement of the liquid crystal elastomer actuator
L_0	total length of the LCE actuator before deformation
L	total length of the LCE actuator after deformation
T_h	total stimulation time
d_d	target displacement
v	control signal
T_d	target temperature corresponding to d_d
λ	deformation coefficient
Q	order parameter
$\bar{Q}$	average order parameter
F	free energy of liquid crystal elastomer molecule
T^*	supercooling temperature
T_1	temperature at the boundary of F at which LCE becomes isotropic
T_2	temperature at the boundary of F at which LCE becomes nematic
T_3	temperature value when the two local minimums of F are the same
Q_1	Q corresponding to a local minimum of F
F_1	value of F corresponding to Q_1
Q_2	Q corresponding to the local maximum of F
F_2	value of F corresponding to Q_2
Q_3	Q corresponding to a local minimum of F
F_3	value of F corresponding to Q_3
ΔE_{21}	free energy difference between (Q_1, F_1) and (Q_2, F_2)
ΔE_{23}	free energy difference between (Q_3, F_3) and (Q_2, F_2)

x	proportion coefficient
W_{13}	transition rate from (Q_1, F_1) and (Q_3, F_3)
W_{31}	transition rate from (Q_3, F_3) and (Q_1, F_1)
k_B	Boltzmann constant
σ	root mean square error
Amp	amplitude of input P
p	model parameter vector
Σ	experimental data set
F_p	filter function
K_f	gain of the filter
T_f	time constant of the filter
C_{in}	inner loop controller
C_{out}	outer loop controller

Abbreviations

LCE	Liquid crystal elastomer
KP	Krasnoselą́rskii-Pokrovskii
PI	Prandtl-Ishlinskii
RMSE	Root mean square error
LM	Levenberg-Marquardt
SMAPE	Symmetric mean absolute percentage error
NRMSE	Normalized root mean square error
DE	differential evolution
HW	Hammerstein-Wiener

Chapter 1

Introduction

This dissertation presents a systematic study on modeling and control of photo-responsive liquid crystal elastomer (LCE) soft robots. Current researches on photo-responsive LCE for soft robot applications are still preliminary. Therefore, in this chapter the state of art of soft robots is firstly introduced. Among soft robot subsystems, the dissertation mainly focuses on the soft robot actuator for its importance to soft robot functionalities. Different actuators based on different selection of materials briefly introduced. Among soft robot actuator materials, smart materials has fast response time, light weight, and can respond to various types of stimuli. These features have attracted scientists' attentions, and so far various studies have been made with conventional electro-driven smart materials such as magnetostrictive materials and electro-active polymers. Recent years, scientists have started to pay attention to soft robot applications based on LCE, which can be chemically modified to deform under the stimulation of light. This property has suggested a whole new direction in soft robot applications. When compared with conventional electro-driven applications, light-driven soft robots can have their stimulation source and actuator totally separated, which offers more freedom in system design. Meanwhile, safety issues brought by high voltage environment can also be avoided. Inspired by the new possibilities LCE brings, my colleagues and I have established an experimental platform of our own to study the deformation of the LCE actuator under light stimulation, with the hope of developing

modeling and control strategies for the photo-responsive LCE actuator to allow light-driven soft robot applications that can achieve high precision locomotion and perform complicated tasks. This is the main objective of this dissertation.

1.1 Soft robot and Smart Materials Based Actuators

The application of robotics has long been an important topic in industrial assembly line, manufacturing, field exploration, medical health care, and everyday life [2–4]. Conventionally, engineers use rigid-body robots to achieve tasks with precise, predictable performance. This type of systems usually uses rigid materials such as plastics and metals, which can be modeled with high accuracy [5,6]. So far, the researches on rigid body robots have been widely carried out, and the results have been useful and fascinating, with applications that can go far beyond one's imagination, beneficial for both scientific studies and human societies.

However, due to the inherent nature of rigid-body robots, they have huge limitations in their interactions with the environments [7, 8]. That is, the hardness of the body and the frictions in the system would often bring safety and adaptation issues, bringing constraints on the task. As a matter of fact, nowadays scientists tend to design structures and functions inspired by existing biological systems. These systems have the features of body softness and compliance, which allow them to interact with the environment more freely. This study on biological inspired robotic systems have lead to a whole new branch of robotic systems, known as soft robots [9–11].

Soft robots are robotics systems which are inherently compliant, and can exhibit large strains in normal operations [12, 13]. Unlike conventional rigid-body robots, soft robots have the feature that they can perform large deformations during their interactions with the environment [14, 15]. This type of systems have a large number of degrees of freedom, and can usually deform their body to interact with the environment more freely and safely, and to mimic the behavior of existing biological systems more accurately. Unlike conventional rigid-body robots, whose actuators are usually located at every joint, soft robots have actuators

made of soft materials which are integrated into and distributed throughout the system [16, 17]. These materials usually have modulus in the range of soft biological materials, which is in the order of $10^4 - 10^9$ Pa [7]. Here, Table 1.1 gives a comparison between characteristics of conventional rigid-body robots and soft robots.

Table 1.1: Comparison between rigid-body robots and soft robots

Type	Rigid-body	Soft
Degrees of freedom	Limited	Large
Actuators	Discret	Continuous
Accuracy	High precision	Relatively low
Safety	Dangerous	Safe
Adaptation	Low	High
Materials	Plastic, metal, etc.	Rubber, polymer, etc.

Usually, the soft robot system is composed of subsystems just like conventional rigid-body robots, this includes the actuation system [18,19], the perception system [20,21], the driving electronics [21, 22], the computation system [23], and the power supply [24, 25]. However, although the composition of soft robots is similar to rigid body robots, huge differences still exist. For conventional rigid body robots, subsystems are usually separated, and each one of them can be studied independently. Meanwhile, for soft robots, all subsystems are integrated together with the actuator to function as a whole. Thus, studying of the soft robots is the studying of soft robot actuators.

For actuation, the selection of the material used for the soft body of the system is of great importance, since it settles the the physical basis of the whole system as well as possible functionalities. Existing actuator materials include the variable length tendons, either using tension cables [26] or shape-memory alloy actuators [27, 28], which are usually embedded in segments to perform a continuous deformation. These type of soft robots are usually composed of small segments, which can be controlled separately to perform a

complex bending. Pneumatic actuation based on rubbers is also very popular [29, 30]. In these systems, a certain fluid is inflated into channels made from elastomers, the asymmetry in the design or constituent materials will cause the system to deform in a desired way. This type of actuation method is straight-forward, and can be miniaturized due to their simplified structure. However, pneumatic networks might require high strains for actuation, which might cause low actuation rates and rupture failures.

Nowadays, more and more studies focus on actuators made from smart materials [31–33]. Smart materials are materials that can deform under various external stimuli, such as stress, electric or magnetic fields, light, temperature, etc. [34]. These smart materials usually have fast response suitable to work under high frequency inputs, and light weight, which allows miniaturization of the system. Smart materials are various, including magnetostrictive materials [35, 36], electro-active polymers [37, 38], liquid crystal elastomers [39–41], etc.. These materials usually deform with a fast response time, and can be miniaturized due to light weight, showing great potential in soft robot applications. Current studies on smart material based actuators for soft robot applications are various. For example, [42] presents soft robots made of dielectric elastomer that can perform simple crawling locomotion. In [43], a swimming soft robot is fabricated using a polymer film containing azobenzene chromophore. [44] utilized the shape memory alloys to design and fabricate a smart modular structure to achieve locomotion such as gripping.

In real applications, in order to perform various tasks and to achieve different functionalities, the study on the modeling and control of the soft robot actuator is an important topic. While smart materials offer promising features, their modeling and control are very challenging. This is because smart materials usually have highly nonlinear hysteretic behaviors [45, 46], this means that the system's current state will be dependant upon its history. Further more, this hysteresis is highly coupled with system's dynamics, resulting a very complicated dependency on factors including the environment, the input, etc.. bringing difficulties in the modeling and control of smart material based actuators.

1.2 Photo-responsive Liquid Crystal Elastomers

While the majority of the studies on smart material based soft robot actuators has been focusing on electro-driven or magneto-driven smart materials [47,48], recent years, scientists start to pay attention to another type of smart material named liquid crystal elastomer (LCE) due to its unique features. LCEs are rubbers consisted of molecules with a certain orientation order. Microscopically, the aligned LCE molecules are incorporated into the backbones of weakly crosslinked polymers. Due to its structure, LCE has the property of elastomers (elasticity) as well as liquid crystals (anisotropy) [49,50]. A very important feature of LCE is that, during the fabrication process, it can be chemically adjusted with certain materials to become photo-active, resulting in a photo-responsive deformation property (Figure 1.1). This photo-responsive deformation can generate large deformation with fast speed [1,51]. So it offers possibilities for fast response applications. Meanwhile, this photo-responsive feature makes it possible to create applications which is different from conventional electro-driven soft robots, which brings novelty in design. Unlike conventional smart material whose power source and actuator are usually integrated together, the photo-responsive LCE actuator can be separated from its power source, which suggests a lighter system with a more flexible design. Moreover, this application does not require a high-voltage environment, so it can avoid safety issues caused by high voltage, which is often seen in applications based on other smart materials such as the dielectric elastomers. Thus, this material provides promising photo-responsive applications with advantages that conventional electrically driven systems do not have.

However, just like most smart materials, the deformation of LCE also exhibits a strong nonlinear behavior such as hysteresis, as well as a high dependency on environmental factors [49]. Details of the LCE's deformation will be discussed in Chapter 3. Roughly speaking, the deformation nature of LCE is the macroscopic shape change caused by the phase transition of LCE molecules, and this phase transition is controlled by the temperature variation of LCE, which is dependent on the incident light. This is deformation process is a complicated

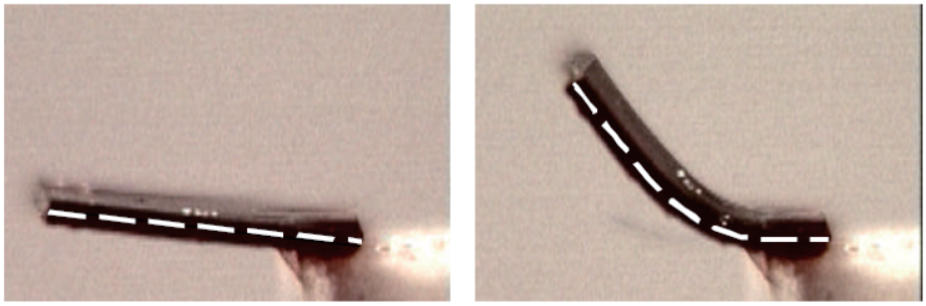

(a) Before deformation (b) After deformation

Figure 1.1: Deformation of LCE under light stimulation, adapted from [1]

multi-step process, which brings in uncertainties and modeling errors, making the modeling and control of photo-responsive LCE actuator a challenging issue. As a matter of fact, the state of art on this subject is still sparse, even though there has been some works on the modeling of the photo-responsive LCE actuator, the study on the modeling and control of the photo-responsive LCE actuator is still at its beginning, and has a long way to go.

To sum up, the study of the photo-responsive LCE actuator is a promising topic due to its novelty in power source, which brings new possibilities in design level. It can avoid safety issues that are often seen in conventional electro-driven applications, and can provide a large deformation with fast response. However, the deformation of the photo-responsive LCE actuator is complicated with highly nonlinear behavior, bringing challenges to its modeling and control. Thus, it is necessary to figure out suitable strategies for the quantitative modeling and precise control of the photo-responsive LCE actuator.

1.3 Objectives and Contributions

Based on the current state of LCE-based soft robots, the objectives of the dissertations as well as the main contributions are summarized.

1.3.1 Objectives of the Dissertation Research

Figure 1.2 gives the temperature-deformation response for the photo-responsive LCE actuator under input signals with different stimulation duration. It clearly shows that LCE's deformation has a highly nonlinear dependency on its temperature, which is mainly caused by its complicated physical nature of the system. Based on Figure 1.2 together with background research, the study on the modeling and control of LCE soft robots faces the following difficulties and challenges:

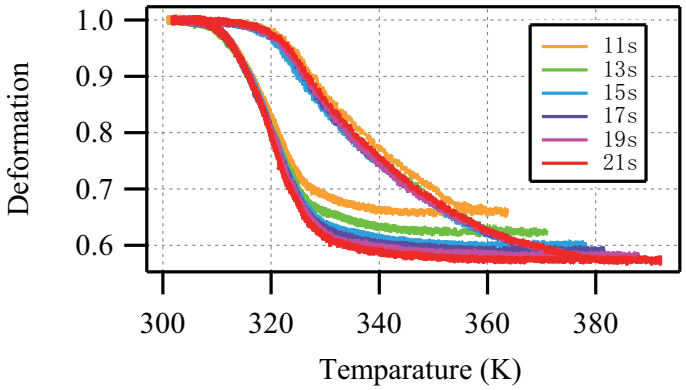

Figure 1.2: Temperature-deformation response under different total stimulation duration

(1) Due to the complicated physical nature of LCE's deformation, so far, works on modeling for the photo-responsive LCE actuator mostly utilize the finite-element method to calculate the deformation characteristic numerically. This numerical method can model the LCE actuator to some extend, but is not quite suitable to be utilized in control problems. In order to study and understand the deformation of the LCE actuator and utilize it for control purposes, it is essential to look into the deformation of the photo-responsive LCE actuator from the physics perspective to develop a basic model that can reflect its physical nature. To establish such a model, a combined study on physics, mathematics and control theories is needed, which is a challenging issue.

(2) The key part in modeling of the photo-responsive LCE actuator is the modeling of its hysteresis. As shown in Figure 1.2, LCE's deformation has a highly nonlinear hysteretic

characteristic, which means that its state is dependant upon its history. This hysteresis is asymmetric. Meanwhile, it is a rate-dependent hysteresis: the temperature-deformation curves with different input stimulation durations, which corresponds to different input frequencies, show very obvious differences. More specifically, curve with an input current of a shorter stimulation duration shows in a much smaller hysteretic loop. Describing this hysteresis nonlinearity with asymmetry and rate-dependency brings great challenges to the modeling and control of the LCE actuator.

(3) The deformation of the photo-responsive LCE actuator is a complicated multi-step process which involves optics, thermal dynamics, electronics and mechanics. Unlike conventional actuators based on electro-driven or magneto-driven materials, whose output can be directly controlled by the input. The input of the photo-responsive LCE actuator only effects its deformation indirectly. This feature brings in more errors in modeling and more external disturbances to the actual device, so it is an issue that has to be considered for the control of the photo-responsive LCE actuator. Besides, for an actual device, the frictions in the system as well as external disturbances cannot be neglected. These realistic factors can strongly effect the control accuracy, and thus need to be considered during controller design.

(4) Model parameters need to be identified and controller parameters requires tuning based on experimental results. Due to the computation complexity of LCE's deformation, it is essential to establish effective strategies for model parameter identification and controller parameter tuning. Meanwhile, the tradeoff between the efficiency and accuracy of model parameter identification and controller parameter tunings should be carefully considered to make both strategies effective. Thus, finding suitable methods for these two issues is of great challenge.

Taking the above addressed challenges into consideration, this dissertation proposes modeling and control strategies suitable for the photo-responsive LCE actuator. By studying the physical nature of LCE's deformation, a basic modeling scheme and a positioning control scheme are presented to give guidance for the modeling and controller design. Then, a basic model is proposed to give a relatively simple analytical temperature-deformation rela-

tionship of the LCE actuator and to reflect the actual physics of the LCE actuator. Based on this basic model, by analyzing the hysteresis with thermodynamics, an improved model is proposed to give the temperature-deformation relationship with high precision. This dissertation also designs controllers with a double closed-loop structure and a feed-forward controller to achieve the positioning control of the photo-responsive LCE actuator with small control errors. Regression methods and intelligent optimization methods are used for model parameter identification, and controller parameter tunings are realized based on experiment and simulation results. Design guidelines for possible LCE soft robots are discussed, and designs for a two-legged walking robot and a light-controlled rolling robot based on the photo-responsive LCE actuator are presented.

1.3.2 Contributions of the Dissertation Research

Based on the presented work in this dissertation, the main contributions of the dissertation are highlighted as follows:

(1) This dissertation proposes a basic modeling scheme for the photo-responsive LCE actuator based on its deformation mechanism. It introduces the average order parameter to give a quantitative representation of the macroscopic average phase of LCE molecules, and points out that the temperature-deformation relationship of the photo-responsive LCE actuator is a combination of the relationship between the temperature of the LCE actuator and the average order parameter, and the relationship between the average order parameter and the macroscopic deformation. Such a modeling scheme provides a basis for developing a model to describe LCE's deformation as well as control strategy design.

(2) This dissertation proposes a basic positioning control scheme for the positioning control of the photo-responsive LCE actuator. Considering that LCE's deformation is a multi-step process with nonlinear characteristics, a feed-forward controller is utilized to compensate the nonlinearity of LCE based on its inverse model, and a double closed-loop control structure is designed to mitigate errors produced in the multi-step deformation process.

(3) Based on the modeling scheme, this dissertation establishes a basic model that gives a relatively simple analytical temperature-deformation relationship for the LCE actuator. This model also works to provide the reflection of the essential physics of the LCE actuator, and can be used as a guidance to predict the deformation of the LCE actuator. This model can also be utilized as a basis for developing more advanced models or control strategies. Here, nonlinear least squares method is utilized for model parameter identification based on experimental results.

(4) Based on the basic physical model, this dissertation studies the hysteresis of the LCE actuator by looking into the dynamic process of the phase transition of LCE molecules. An improved model is proposed to provide a dynamic equation to describe the temperature-deformation relationship of the LCE actuator. This model works to give a detailed description of LCE's hysteresis, and can describe the deformation characteristics with high accuracy. Here, a two-step parameter identification strategy based on differential evolution algorithm and nonlinear least squares method is established for the effectiveness of model parameter identification.

(5) Based on the basic physical model, controllers are designed for the positioning control of the photo-responsive LCE actuator. The basic model in (3) is utilized to construct a numerical inverse as a feed-forward controller to compensate the nonlinearities of LCE, and two PID controllers with a double closed-loop structure are designed to reduce control errors. Filters are designed to reduce measurement noises. Here, controller parameters are tuned based on experimental and simulation results. The designed controller can control the LCE actuator with a faster response time and a smaller control error when compared with single loop controller.

(6) By analyzing the unique features of the photo-responsive LCE actuator, this dissertation provides design guidelines for possible soft robot applications driven by light. As a demonstration of the guidelines, designs of a two-legged walking robot and a light-controlled rolling robot are presented and discussed.

1.4 Organization of the Dissertation

This dissertation consists a total of eight chapters. The topic of each chapter is briefly introduced as follows.

In Chapter 2, an overview on the modeling and control over hysteretic systems, as well as the state of art of the LCE actuator will be provided.

In Chapter 3, the basic deformation mechanism of the photo-responsive LCE actuator will be firstly introduced. Then, based on the deformation mechanism, experimental platform for the photo-responsive LCE actuator is established. Schematic of the LCE actuator and its related basic concepts are presented.

In Chapter 4, a basic modeling scheme for the modeling of the LCE actuator is firstly established based on the deformation nature of LCE. Then, based on this basic modeling scheme, by assuming that LCE molecules' phase transition process at each moment satisfies dynamic equilibrium, a basic model is established to give a relatively simple temperature-deformation relationship. Model parameters are identified using nonlinear least squares method. This model can reflect the essential physics of the LCE actuator, which can be used for developing more advanced models and control strategies.

In Chapter 5, based on the basic model presented in Chapter 4, by looking into the dynamic process of the phase transition process of LCE molecules, an improved model is established to give a dynamic equation for the temperature-deformation relationship of the LCE actuator. A two-step parameter identification strategy is established for model parameter identification. This model provides a full physical description of LCE's hysteresis and can predict the deformation of the LCE actuator with high accuracy.

In Chapter 6, a positioning control scheme with a double closed-loop structure and a feed-forward controller to realize the positioning control of photo-responsive LCE actuator is established. Controllers based on this scheme are designed to achieve the positioning control target with precision. Controller parameters are tuned based on simulation and experiments. Comparisons are made with conventional single closed-loop control structure

to show that the proposed controller that is specifically designed for the LCE actuator has faster response and smaller control error than conventional single loop structure.

In Chapter 7, unique features of the photo-responsive LCE actuator are reviewed to provide a design guideline for LCE-based soft robots. As a demonstration of the guideline, two possible soft robot applications are proposed for the photo-responsive LCE actuator. Their structures are introduced, and the basic mechanisms are presented.

Finally, Chapter 8 gives the conclusions of this dissertation with possible suggestions of future works on this subject.

Chapter 2

Literature Review

In this chapter, literature review is carried out on the modeling and control of LCE soft robots. Studies on LCE soft robots are relatively scarce, so we look into the modelling and control of smart materials with hysteresis. While different types of smart materials differ greatly, they still have one thing in common: most of their input-output characteristics are dominated by a magic called hysteresis. Thus, it is only reasonable to look into this subject and ask what hysteresis is, and how hysteretic systems are modeled and controlled.

2.1 Hysteretic Systems

As has been discussed, hysteresis is the dominant feature of the deformation of LCE, as well as most smart materials. Generally speaking, hysteresis happens when the current state of the system is not only dependant upon the current input, but also the trace of the state's history. It can be regarded as a dynamic lag of the effect of the input on the system [52]. Interestingly enough, this topic expand to a wide spread of different areas, including physics [53], chemistry [54], engineering [55], biology [56] and even economics [57]. Such a phenomenon is often seen, but still mysterious in various ways.

Here, the definition of hysteresis is introduced based on the concept in control theory [58],

consider a transducer HT with an input $u(t)$ and an output $f(t)$, as shown in Figure 2.1(a). This transducer is a hysteresis transducer if its input-output relationship is a multi-branch nonlinearity for which branch-to-branch transitions occur after the input reaches the extremal, as shown in Figure 2.1(b).

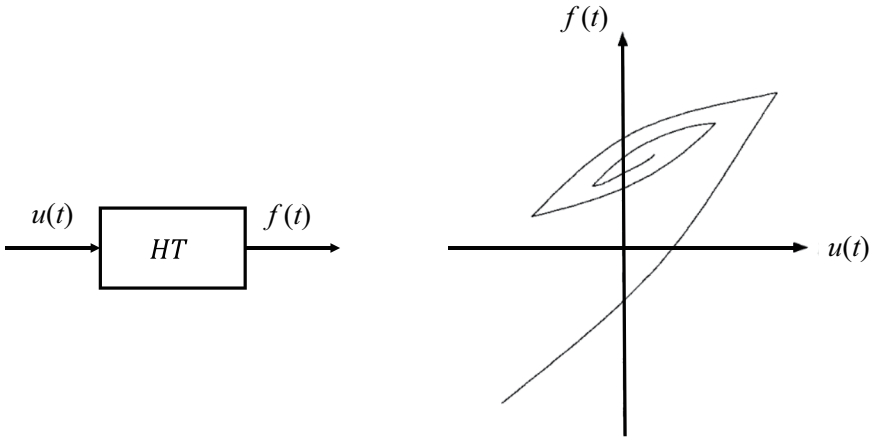

(a) a hysteresis transducer (b) hysteresis nonlinearity

Figure 2.1: Definition of Hysteresis

Hysteresis exhibits different characteristics. It can be classified into rate-dependent hysteresis, or rate-independent hysteresis. This is based on whether or not its input-output curve will change depending on the input frequency [59]. As for the situation in soft robots, for smart materials with hysteresis, the hysteresis is always highly coupled with the system dynamics, which results in the rate dependency of hysteresis, as well as dependencies on other parameters, bringing difficulties to the modeling of the soft robot system.

Besides the rate dependency, hysteresis loops can be classified into symmetric hysteresis loops, or asymmetric hysteresis loops, based on the shape of the loop. Certain smart materials based actuators, such as some piezoelectric actuators, exhibit symmetric hysteresis loops [60]. As for the photo-responsive LCE actuator, which is the focus of this dissertation, the hysteresis loop is asymmetric. This feature should be taken into consideration during the modeling of the hysteresis of the photo-responsive LCE actuator.

2.2 Modeling of Hysteretic Systems

The deformation characteristic of LCE is dominated by hysteresis. Thus, in order to learn how to characterize this hysteresis, it is only reasonable to review modeling methods for smart materials with hysteresis [61, 62]. Usually, modeling methods for smart materials are classified into two types: physics based models and phenomenological based models.

The physics based model is usually built based on physical phenomena and first principles. This modeling method describes the deformation characteristics of different smart materials from different physical nature. For example, the Jiles-Atherton model aims for the hysteresis of magnetostrictive materials [63, 64]. The domain wall model studies the hysteresis and nonlinearities corresponding to the domain structure inherent to the piezoelectric materials [65]. The Stoner-Wohlfarth model describes the hysteresis by regarding the ferromagnetic material as a single magnetic domain [66, 67]. This type of modeling method tells the actual physical process related to a specific material's deformation, and it usually has complicated calculation, and cannot describe the hysteresis well.

The phenomenological based model is proposed to describe the hysteretic nonlinearity without the need to introduce detailed physical meanings of the deformation process. Compared with the physics based model, this modeling method is relatively more analytically computable. This type of models are further classified into two different classes: the differential equation based models, and the operator based models. The differential equation based models include the Duhem model, the Bouc-Wen model, etc.. The Duhem modeling method uses mass-spring-damper system to describe magnetic hysteretic nonlinearities of the model [68, 69]. The Bouc-Wen model is a half-physics model based on Duhem model, and has versatility by producing a variety of hysteretic patterns [70]. For these differential equation based models, the computation complexity is relatively simple. However, these models are finite dimensional, which may lead to large modeling errors.

Operator based models describe hysteresis by mathematical operators [71]. These models are usually more convenient in calculation, and are currently quite popular in industrial

applications. For example, the Preisach model [72, 73] is a commonly used operator based model, it can be considered as a superposition of elementary hysteretic relay operators, and is proposed for ferromagnetic materials. The Krasnoselą́rskii-Pokrovskii (KP) model uses the kernel functions for the description of hysteresis, and has been used to model the hysteresis in various smart material based actuators including the shape memory alloy actuators and piezoelectric actuators [74, 75]. The Prandtl-Ishlinskii (PI) model [76, 77] is constructed based on continuous play or stop hysteresis operators, and can be used to describe hysteresis of a certain type, such as the symmetric hysteresis, the rate-independent hysteresis, etc.. Meanwhile, the PI model has the advantage that it is analytically invertible, and this analytical inverse model will be very useful in the inverse compensation scheme for control purposes [78]. Operator based models can provide high precision of the hysteresis description. However, since the modeling accuracy is basically proportional to the total number of operators, a high precision means a large number of operators, leading to heavy computation. Thus, the trade-off between modeling accuracy and computation complexity must be taken into consideration.

Overall, the phenomenological based model is relatively convenient in calculation when compared with physics based model. This type of modeling method is usually developed to describe the hysteresis only, so it cannot reflect other physical process of the deformation. The classification of the existing modeling methods for hysteresis is given in Figure 2.2.

Based on the above two methods, another way of modeling the hysteretic system is the combined modeling strategy of both methods. Eg. In [79], the researchers use an operator based model to describe the hysteretic part of the system, while the mechanical part of the system is still established by physical description. These two parts are then connected together based on the relationship between model parameters. This combined modeling method can effectively simplify the calculation involving hysteresis, and can also reflect the physical nature of the system to some extent. So it is a promising modeling method that can be utilized for smart material based actuators.

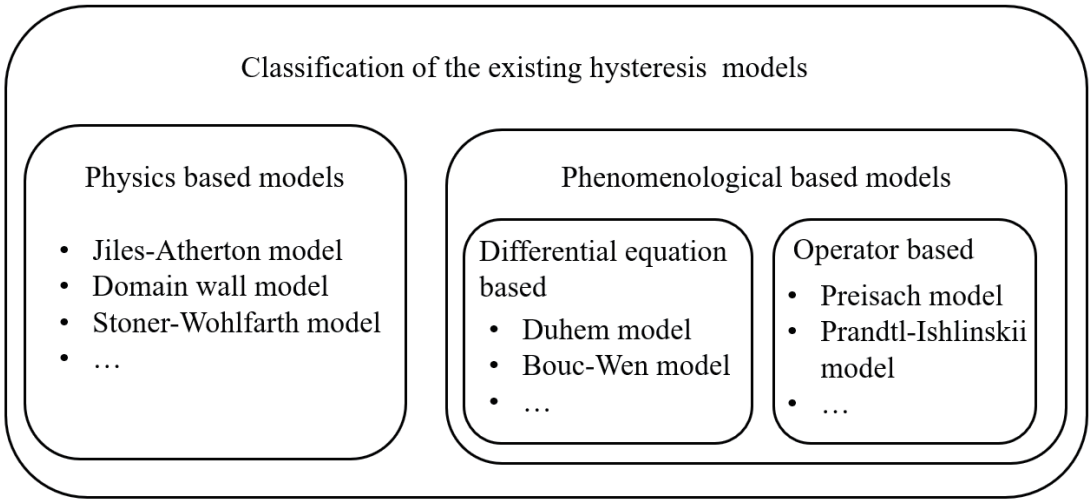

Figure 2.2: Classification of the existing modeling methods for hysteresis

2.3 Control of Hysteretic Systems

As mentioned in the previous chapter, the actuator of the soft robot usually carries out most of the operations. Thus, in most cases, the control of a soft robot is equivalent to the control of its actuator. Meanwhile, as the dominant feature of the deformation characteristics of smart materials, hysteresis has always been a very challenging issue which might lead to inaccuracy, or even instability during the control of the smart material based actuators [80]. It is very important to mitigate such hysteresis during the control of the smart material based actuator. So far, ways of dealing with the hysteresis in control problems can be classified into two methods: the direct method and the inverse compensation.

2.3.1 Direct Method

In this type of method, the unknown hysteresis is usually divided into linear and nonlinear parts, in which the latter parts are treated as a disturbance and gets mitigated. Typical examples include using the sliding mode control [81,82], the adaptive control method [83–85], the energy based approach [86], etc.. In [82], sliding mode control strategy with perturbation

estimation is established for the tracking control of a piezoelectric actuator based system. By introducing various adaptive rules to update the controller parameters online, the excitation of high frequency unmodeled dynamics leading to the increase of the oscillations in the control signal is mitigated ensure stability. In [83], an adaptive variable structure control strategy is fused with the PI model to ensure the global stability as well as the tracking control precision of the system. In this work, one crucial point is that the uncertain term in the PI model is not bounded. To solve this issue, this uncertain term is treated as a parameter from the hysteresis model and adaptive law can be utilized to obtain its estimation. [86] looks up the energy properties of the Preisach hysteresis model and derives a passivity property for controller design to mitigate the hysteresis nonlinearity. These methods have the advantage to avoid the computational complexity of obtaining an inverse model for the hysteresis when compared with the inverse compensation method. However, this type of methods might face computational burdens in determining the values of the parameters related to the controller [85], it might also lead to large control errors [80].

2.3.2 Inverse Compensation Method

Another common control scheme for dealing with hysteresis is the inverse compensation. In this situation, an inverse model of the hysteresis model is constructed as an feed-forward module to be inserted in front of the hysteresis model, such an inverse model can compensate for the nonlinearities brought by the hysteresis in the system, and the output should be a linear tracking of the input signal, as shown in Figure 2.3. Here, the inverse model of the hysteresis can be constructed either numerically, or analytically. Eg. [87] develops the inversion procedures for the two-input and three-input Preisach model to obtain an open-loop control strategy for electromagenetic actuator. [88] achieves inverse compensation for Preisach model using an inverse multiplicative structure, which is established by reformulating the Preisach model into an explicit expression of the input. In [89], the inverse of a KP model for piezoelectric stack actuator is developed and verified through simulation. Here, it should be noted that the above presented examples of inverse compensation on Preisach

model and KP model are all numerical models. The numerical computation of the inverse models usually brings computation complexity as well as modeling errors.

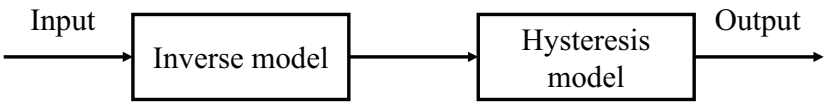

Figure 2.3: Inverse compensation for hysteretic systems

The PI model has the advantage that it has a analytical inverse [90–92]. Thus, inverse compensation of the PI model usually has the advantage of less computation complexity and smaller modeling errors. [93] applies the inverse of a rate-dependent PI model to perform feed-forward inverse compensation on the rate-dependent hysteretic characteristic of a piezomicropositioning stage. [94] adapts this inverse of PI model perform the precise tracking control of a piezoelectric-actuated system. To mitigate remaining unknown nonlinearities and disturbances, a sliding-mode controller is adapted. [95] presents the analytical inverse of a generalized PI model, which works for both symmetric and asymmetric hysteresis, and was presented in [96].

Besides the above presented methods, the inverse compensation can also be achieved based on other strategies such as the neural network method [97] or fuzzy logics [98]. Furthermore, this method can be applied to physics-based model as well. eg. [99] presents an inverse-based model predictive controller for piezoelectric actuators. Experiments showed that the hysteresis of piezoelectric actuators can be effectively compensated.

In a real control system, there will always exist a modeling error, for both the hysteresis model and the inverse model. Thus, the inverse model alone is not enough to realise the precise control of actuators with hysteresis. To mitigate the errors from inverse compensation, an effective way is to utilize the feedback control strategy together with inverse compensation (Figure 2.4). Normally, for a feedback control structure without inverse compensation, the existence of hysteresis will lead to control errors that cannot be neglected. On the other hand, an open-loop inverse compensation structure has modeling errors that will also cause

inaccuracy of the control results. This inverse-based feedback control strategy utilizes these two methods together to overcome each others' drawbacks to obtain a strategy in which the inaccuracies brought by the nonlinearities and the modeling errors are both mitigated. [100] gives a typical example of this strategy for the control of a piezoelectric positioning stage, in which a neural-network based robust adaptive output-feedback motion controller with inverse hysteresis compensation is adopted.

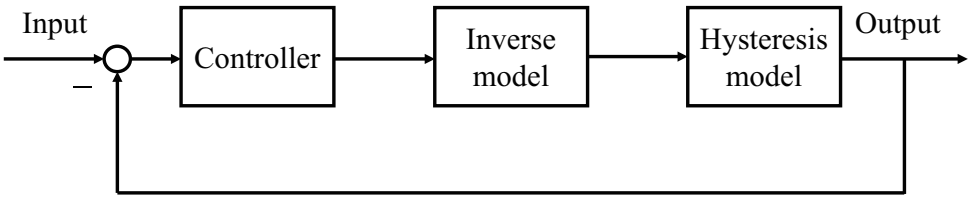

Figure 2.4: Inverse-based feedback control strategy

2.4 State of the Art of LCE Actuator

Based on the unique property of the photo-responsive LCE actuator, scientists have established various related actuators designs. [51] presents a natural-scale caterpillar robot that can perform various tasks under the stimulation of light. In this work, LCE films are patterned with a certain molecule orientation, and a laser beam is scanned along the body of the film. The light-induced deformation of the LCE film results in locomotion of moving forward or backward on platforms with different slopes. In [101], polymer-grafted gold nanorods are doped into dynamic azobenzene liquid crystal networks, which allows LCE to responsive to both near infrared and ultra violet light, respectively, with different deformation reactions. Based on this technique, the photocontrol of LCE is enhanced to perform complicated motions. Further more, soft robot arm is designed to perform lifting and gripping. This work suggestss that this material can be further chemically modified to achieve diversity in the locomotion of the soft robot.

In [102], the photo-responsive LCE actuator is integrated with an optical fibre to realize

a flytrap-like device, in which the mechanical motion is achieved by light-induced bending of the LCE actuator. This device can perform bending as well as gripping locomotion to mimic the behavior of the Venus Flytrap. This is a typical realization of soft robots that are inspired by biological systems. In [103], mechanical strain energy is prestored in the polymer to produce force from light-triggered release of the prestored stain energy, based on which a rolling vehicle like device is fabricated to perform rolling locomotion. Such an application is a clear reflection of how flexible the design of LCE-based soft robot applications can be. In [104], an LCE-carbon nanotube-based soft robot is fabricated to perform multi-modal motions including crawling, squeezing, jumping, etc.. Modes of the locomotion are switched from one to another by changing way of the light stimulation. The above studies show that LCE actuators indeed offer a unique and promising light-controlled soft robot application.

However, in actual applications, the realization of a rough locomotion is still not enough. Many scenarios require the soft robot system to achieve more complicated and more precise tasks. Thus, in order to control the LCE actuator accurately, the study on the modeling and control of the photo-responsive LCE actuator is necessary. [105] presents a continuum mechanical model based on finite-element simulation to study the deformation of LCE. However, this work is under isothermal consideration, which does not apply for the photo-responive LCE actuator. In [106] the basic physics underlying in LCE's deformation is analyzed to give a basic physics model, which describes the temperature-deformation relationship with a relatively simple equation. The work of this article can be treated as a special case of this dissertation, and will be presented in Chapter 4. As a matter of fact, besides [106], current existing models for LCE mostly use the finite element method [107, 108]. The study on the modeling and control of the LCE actuator is still very preliminary.

2.5 Concluding Remarks

To sum up, a literature review on the modeling and control of smart materials is given. Modeling strategies for smart materials can be classified into two types, physics based models

and phenomenological based models. The physics based models give a more physical description on the deformation nature of the system, but usually have complicated computation. Meanwhile, the phenomenological based models are relatively convenient in calculation when compared with physics based model, but describing only the hysteretic part of the system. Control methods for smart materials include the direct method and inverse compensation. As for the modeling and control of photo-responsive LCE actuators, the current works mainly use the finite element method, and is still preliminary. This shows that the study on developing modeling and control strategies for LCE actuators is of great importance.

Chapter 3

Experimental Platform and Basic Concepts on LCE Actuator

This chapter introduces the deformation mechanism of the photo-responsive LCE actuator. Based on the deformation mechanism, the experimental platform for measuring and control of the photo-responsive LCE actuator is established. Then, schematic of the studied LCE actuator as well as some basic concepts are introduced.

3.1 Deformation Mechanism of LCE

As introduced in previous chapters, LCE is composed of LCE molecules that are weakly crosslinked into networks. Due to different arrangement of LCE molecules, LCE is usually categorized into three types: nematic, cholesteric or smectic. This dissertation focusses on the most commonly discussed nematic LCE. For nematic LCE, under room temperature, LCE molecules roughly line up along a certain direction n, called the average ordering direction, which is set upon fabrication. In this situation, LCE molecules are in nematic phase. Meanwhile, the macroscopic shape of LCE is coupled with this microscopic order and will exhibit anisotropic properties [109]. For photo-responsive LCE, the stimulation of

light causes the temperature to increase, and LCE molecules gradually lose their order as the temperature goes higher. When they lose their orders, LCE molecules are in the isotropic phase. In this situation, the macroscopic LCE will also lose its order and become isotropic. which results in a macroscopic shape change.

This deformation mechanism can be shown in Figure 3.1. For the macroscopic shape change of photo-responsive LCE, the temperature increases when being stimulated by light. Then, the phase transition from the nematic phase to the isotropic phase will cause LCE to shrink along the average ordering direction n, and expand along directions perpendicular to n. Similarly, when light stimulation is off, the temperature decreases back to room temperature. Correspondingly, the phase transition from the isotropic phase to the nematic phase will cause LCE to elongate along the average ordering direction n, and shrink along directions perpendicular to n.

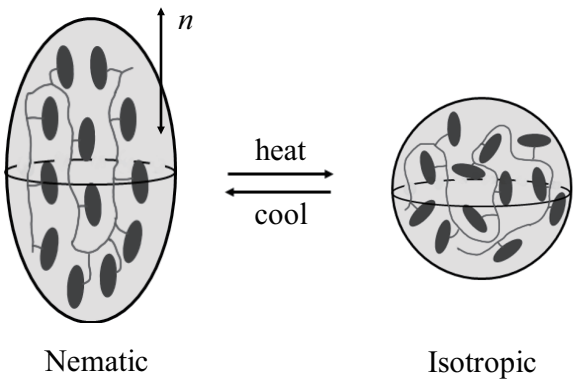

Figure 3.1: Deformation process of nematic LCE

From the above discussion, it can be concluded that the direct reason for LCE's deformation is the microscopic phase change of LCE molecules, caused by the variation of the temperature of LCE, which is controlled by the incident light. This fact suggests that, for the modeling and control of the photo-responsive LCE, it is preferable to introduce a certain variable to quantitatively describe the average phase of LCE molecules. It is also preferable that the temperature of LCE can be measured when setting up the experimental platform

to provide a way of directly evaluating the influence of the temperature on the deformation, as well as the influence of the incident light on the temperature.

3.2 Experimental Platform

Based on the deformation mechanism, an experimental platform is set up to study the deformation of the photo-responsive LCE actuator. The experimental platform for LCE actuator is shown in Figure 3.2. Meanwhile, Figure 3.3 gives a photo of the platform during its operation. The system includes a computer, an I/O module, a programmable laser, the LCE actuator, a thermal camera, and a laser distance sensor. The whole system is surrounded by light-absorbing metal plates for safety considerations.

Details on each device in the experimental platform are introduced as follows.

Computer: this desk top computer works to send out a voltage control signal as the command signal through the I/O module to the programmable laser, and receives measured data from the I/O module. It also works as the computational subsystem in the modeling and control of the photo-responsive LCE actuator.

I/O Module: a MicroLabBox 1202/1302 dSPACE module is employed to send voltage control signal from computer to the programmable laser and collect measured temperature and displacement signals generated by the thermal camera and the laser sensor.

Programmable laser: a personalized programmable laser works as the power source of the LCE actuator. The voltage of the control signal corresponding to the command signal from the computer is directly proportional to the laser's output power efficiency P.

The LCE actuator: the LCE actuator is a 1.0×0.5 cm rectangular strip of LCE. It has one edge fixed and another edge movable, whose displacement d is measured by the laser distance sensor.

Thermal camera: the FLIR A315 thermal camera collects temperature information from the LCE actuator with 0.1 s sampling time. Here, the temperature T is the average temper-

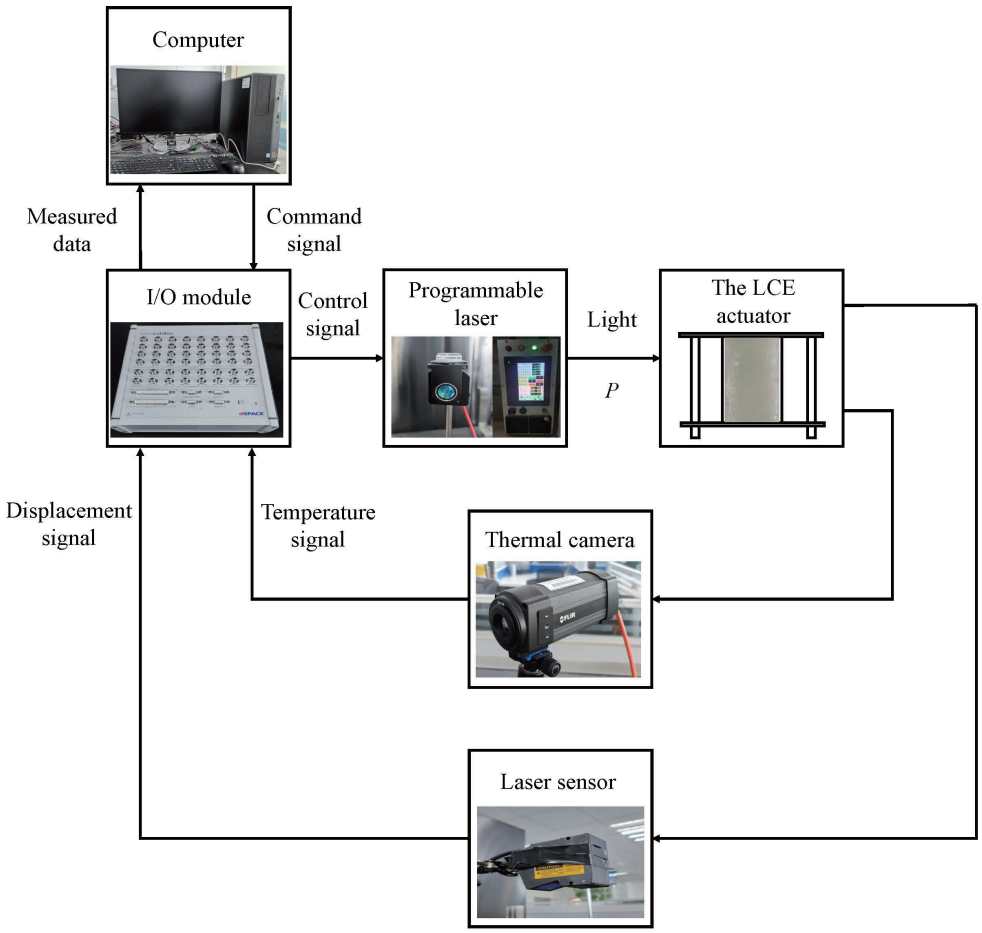

Figure 3.2: The experimental platform

ature of the LCE actuator. Since the LCE actuator in experiments is small enough to be fully covered by the laser light, it is reasonable to assume that its temperature is likely to be evenly distributed. Thus, the measured T can be used to represent its temperature.

Laser distance sensor: a Keyence LK-H152 laser sensor is utilized to measure the deformation of LCE. In the positioning control, this laser emits light on the movable edge of the LCE actuator, by detecting the diffuse reflection signals, the displacement of the movable can be obtained.

As shown in Figure 3.2, in experiments, the computer sends out a command signal as the

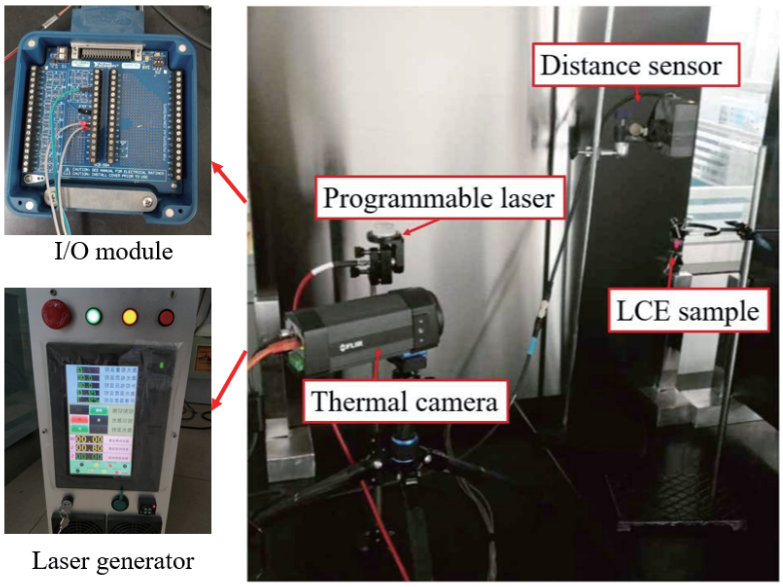

Figure 3.3: A photo of experimental platform during its operation

input, which goes through the I/O module to the programmable laser. The programmable laser then produces a light to stimulate the LCE strip. The power efficiency P of the light is directly proportional to the voltage control signal which corresponds to the command signal. Under light stimulation, the LCE actuator is heated up, and its temperature T increases. Due to the variation in T, the LCE actuator will shrink along the vertical direction. The movable edge of the LCE actuator moves a certain distance, which is represented by the displacement d.

3.3 Schematic of LCE Actuator and Related Basic Concepts

A more detailed schematic of the LCE actuator in the experimental platform is shown in Figure 3.4 to show its deformation. The main axis n of the LCE is along its length, which is the vertical direction. Usually, the deformation along the main axis is much more obvious

than along directions perpendicular to the main axis. Thus, in experiments, the study mainly focuses on deformation of the LCE actuator along in the vertical direction.

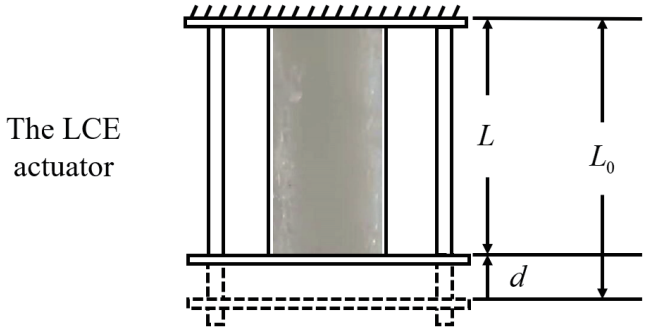

Figure 3.4: Schematic of the LCE actuator

In experimental setup, the upper edge of the LCE actuator is fixed to a metallic stand, while the other edge is movable and is connected to a 5 g weight. Under room temperature, the LCE actuator stretches naturally along n, and its total length is L. When the light stimulation is on, the temperature T of the LCE actuator increases, and the LCE actuator will shrink along n. Its bottom edge moves a distance d, and its total length decreases to L.

While the displacement d can be used to directly represent the deformation of the LCE actuator, in modeling of the LCE actuator, the deformation coefficient λ is a more often used variable. The definition of the deformation coefficient λ is the ratio between the total length after and before deformation. It can be given as:

$$\lambda = \frac{L}{L_0} = \frac{L_0 - d}{L_0} \tag{3.1}$$

In (3.1), d and L_0 are directly measurable. In this dissertation, for the modeling of the LCE actuator, the deformation coefficient λ is used to represent the deformation of the LCE actuator for the convenience of building the model from physical consideration. As for the positioning control of the LCE actuator, the displacement d is used to represent the deformation of the LCE actuator as a direct comparison with the positioning control target.

3.4 Concluding Remarks

In this chapter, it is introduced that the deformation of the photo-responsive LCE actuator is macroscopic shape change coupled to the microscopic phase change of LCE molecules, which is caused by the variation of the temperature of LCE under incident light. Based on the deformation mechanism, an experimental platform for the modeling and control of photo-responsive LCE is established. Details on each part of the experimental platforms are introduced. Schematic of the LCE actuator in experiments is presented, and basic concepts on its deformation are given.

Chapter 4

Modeling for LCE Actuator Based on Dynamic Equilibrium of Phase Transition

In this chapter, a basic modeling scheme for the modeling of the LCE actuator is first presented based on its deformation mechanism. Then, a basic model is established to give a simple analytical relationship to describe the deformation of the LCE actuator based on the proposed modeling scheme. In the model, the state of an LCE molecule is studied based on analysis of the Landau-de Gennes expansion of free energy for nematic LCEs. To study the microscopic phase change of LCE molecules, a commonly used assumption that the transition rates between two phases are always under dynamic equilibrium is made. Then, the coupling relationship between macroscopic deformation of the LCE actuator and microscopic phase change of LCE molecules is obtained based on the second law of thermodynamics. The above studies together give the final basic model that describe the deformation of the LCE actuator. Model parameters are identified with experimental data based on the nonlinear least squares method. Analysis on the experimental results verifies the validity of the proposed model.

4.1 The Development of a Basic Modeling Scheme for LCE Actuator

With the purpose of realizing complex and precise control tasks, it is important to first establish a model that analytically predict the nonlinearities shown in Figure 1.2. In this section, a basic modeling scheme for the photo-responsive LCE actuator is established based on it working principle. This modeling scheme will act as a basis for building specific models to characterize the deformation of the LCE actuator.

4.1.1 Working Principle of LCE Actuator

Based on the deformation mechanism and experimental platform that are introduced in Chapter 3, Figure 4.1 gives a schematic of the basic working principle of the photo-responsive LCE actuator. Based on Figure 4.1, the process of LCE's deformation is can be separated into three independent steps:

(1) Light stimulation

In this step, a control signal is sent to the programmable laser as its input, the laser then send out a light of energy efficiency P, which is proportional to the input control signal.

(2) The light-induced temperature change

In this step, the LCE actuator collects energy from the incident light, this process results in the variation of temperature T. This is a heating process, and can be described by either a heating model or a mathematical model.

(3) Thermal-induced phase change

In this step, the temperature variation of the LCE actuator results in the phase transition of LCE molecules, which causes macroscopic deformation of LCE. This is the step which directly causes the deformation of the LCE actuator, and is where hysteresis takes part. Thus, this step is the focus of the working for the modeling of the LCE actuator.

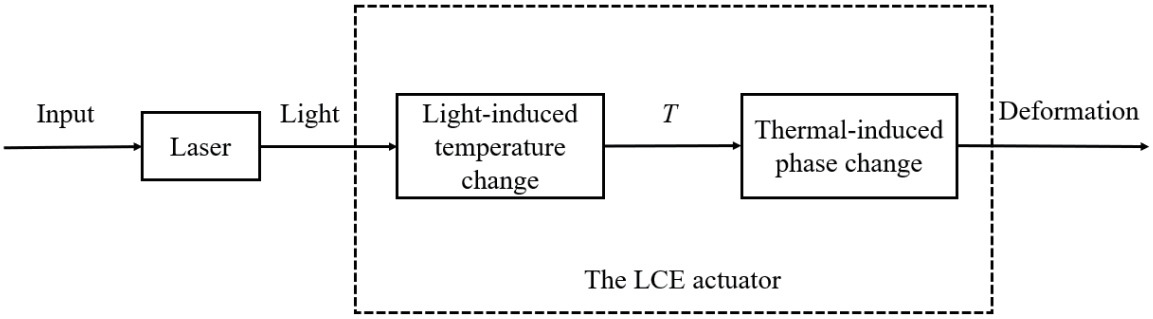

Figure 4.1: The working principle of the LCE actuator

For the above deformation process, the first two steps do not involve hysteresis, and they can be modeled together either with a physical heating model or with a mathematical model. Meanwhile, the third step involves the direct cause of LCE's deformation, and is where hysteresis takes part. Thus, in the modeling of the LCE actuator, we mainly focuses on the study of the third step, and the goal is to obtain a relationship to describe the temperature-deformation response for this step. As for the modeling of the first two steps, it will be dicussed in Chapter 6.

4.1.2 Basic Modeling Scheme for LCE Actuator

According to previous discussions, the main goal of modeling for LCE actuator is to model the temperature-deformation response for the thermal-induced phase change stage. That is, the main goal of modeling the LCE actuator is to derive the relationship between the deformation λ and the temperature T.

As discussed in previous sections, the macroscopic deformation is directly resulted from the phase transition of LCE molecules between the nematic phase and the isotropic phase, and it is preferable to use a certain variable to quantitatively describe this phase transition.

From the physics perspective, the difference of the nematic phase and the isotropic phase is that, in the nematic phase, the LCE molecules line up along n, while in the isotropic

phase there's no order. Usually, researchers use the order parameter Q to describe the order of LCE molecules. According to [49], Q is proportional to the projection of the square of momentum operator of the LCE molecule along the n direction, it has a maximum value $Q = 1$ which corresponds to perfect nematic order, where all molecules align with n. $Q = 0$ represents the isotropic situation. It's minimum value $Q = -1/2$ does not have real physical meanings. Since the order of LCE molecules is closely related to the phase, the average order parameter $\bar{Q}$, which is the average order of all LCE molecules, works as a quantitative reflection of LCE's macroscopic deformation. Hence, $\bar{Q}$ works as a main variable to describe the phase transition of LCE molecules quantitatively.

As a matter of fact, based on thermodynamic analysis. The relationship between $\bar{Q}$ and T, and the relationship between λ and $\bar{Q}$ can be obtained, independently. Thus, these two relationships are combined to establish the overall model that gives the relationship between the deformation λ and the temperature T. Meanwhile, the model parameters are identified through parameter identification based on experimental data. Thus, the whole modeling scheme for LCE actuator is shown in Fig. 4.2.

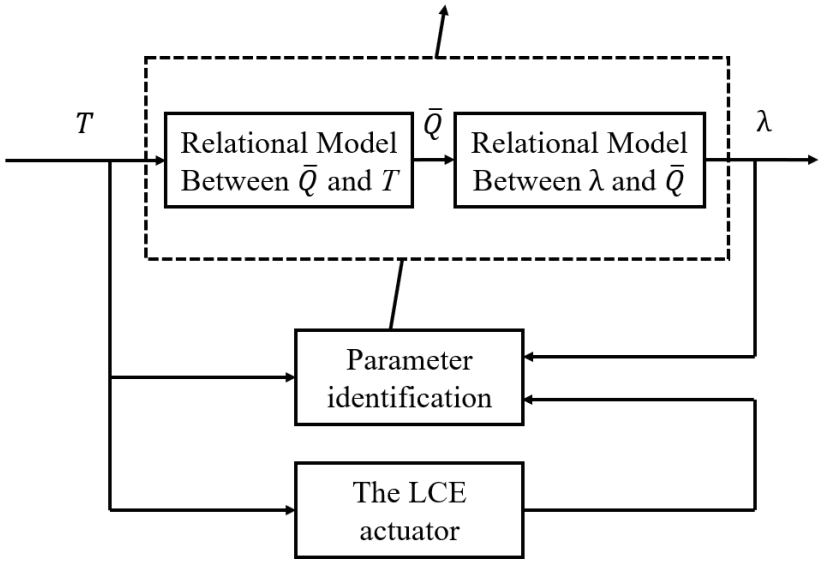

Figure 4.2: The modeling scheme for LCE actuator

4.2 Order Parameter Calculation Based on Free Energy of LCE Molecules

During the deformation process of the LCE actuator, the free energy of a system is an important variable which reflects the energy exchange in the process and can be often used to evaluate the system's thermal equilibrium. According to thermodynamic physics, it always tends to be at its local minimum. Usually, the free energy can be written as an expansion of the system's order parameter [110]. Thus, the order parameter of an LCE molecule is closely related to its free energy. For nematic LCE, the free energy of an LCE molecule can be approximated using the Landau-de Gennes expansion, which is an expansion using Q, and is given by the following equation:

$$F(Q) = \frac{1}{2}AQ^2 - \frac{1}{3}BQ^3 + \frac{1}{4}CQ^4 \tag{4.1}$$

in which A has a temperature dependency given by:

$$A = A_0(T - T^*) \tag{4.2}$$

where A_0, B, C are phenomenological parameters calculated from the partition function of the system, T is the temperature of LCE and T^* is the supercooling temperature [49] of LCE. These parameters can be obtained by parameter identification based on experimental data.

According to equation (4.1), the relation between the free energy F and the order parameter Q under different temperatures T is plotted in Figure 4.3. In this figure, T_1 and T_2 ($T_1 > T_2$) are temperatures corresponding to the boundaries of different situations. T_3 is a special case at which satisfies $F(Q_1) = F(Q_3)$, in which Q_1 and Q_3 are the two local minimums of F. Curve a (the blue line), b (the red line) and c (the green line) correspond to different temperature range. More specifically, curve a corresponds to the temperature $T = T_1$, when $T \geq T_1$, the LCE molecules can only be in the isotropic phase. Curve c corresponds to the temperature $T = T_2$, when $T \leq T_2$, the LCE molecules can only be in

the nematic phase. Curve b corresponds to the temperature in between T_1 and T_2, in this range, the molecules can be either at the isotropic phase or the nematic phase. Curve d (the black line) is a special case that corresponds to temperature $T = T_3$.

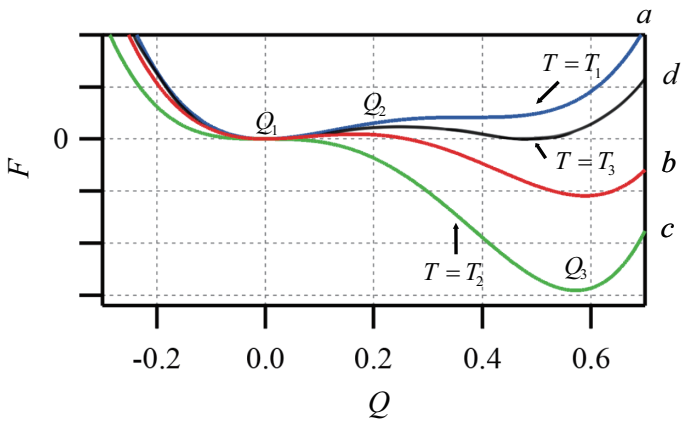

Figure 4.3: Plot of LCE's free energy under different temperatures

Among these curves in Figure 4.3, curve b is the one that corresponds to the most complicated situation. Figure 4.4 gives the enlarged plot of of curve b. For this curve, there are two local minimums points (Q_1, F_1) and (Q_3, F_3). Here, $Q_1 = 0$, so (Q_1, F_1) corresponds to the isotropic phase. (Q_3, F_3) is a stable state with $Q_3 > 0$, so it corresponds to the nematic phase. Meanwhile, there is also a local maximum point (Q_2, F_2). Here, $F_i = F(Q_i)$ $(i = 1, 2, 3)$. The transition rate W_{13} gives the possibility of an LCE molecule transiting from (Q_1, F_1) to (Q_3, F_3), and the transition rate W_{31} gives the possibility of an LCE molecule transiting from (Q_3, F_3) to (Q_1, F_1).

The values of Q_1, Q_2 and Q_3 can be obtained by calculating $\partial F/\partial Q = 0$, which gives

$$\begin{cases} Q_1 = 0 \\ Q_2 = \dfrac{B - \sqrt{B^2 - 4A_0(T - T^*)C}}{2C} \\ Q_3 = \dfrac{B + \sqrt{B^2 - 4A_0(T - T^*)C}}{2C} \end{cases} \tag{4.3}$$

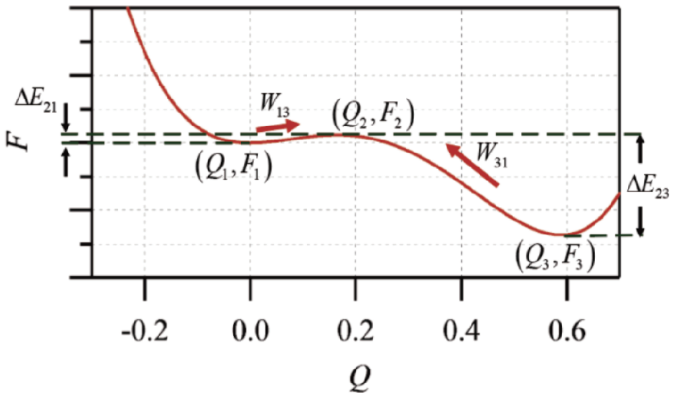

Figure 4.4: An enlarged plot of curve b in Figure 4.3

By setting $Q_2 = Q_3$, which is equivalent to $B^2 - 4AC = 0$, the value of T_1 can be obtained:

$$T_1 = T^* + \frac{B^2}{4A_0C}, \tag{4.4}$$

By setting $Q_1 = Q_2$, which is equivalent to $B - \sqrt{B^2 - 4AC} = 0$, the value of T_2 can be obtained:

$$T_2 = T^*. \tag{4.5}$$

As mentioned, when $T_2 < T < T_1$, which corresponds curve b, an LCE molecule will stay either at (Q_1, F_1) or (Q_3, F_3). Under the influence of thermodynamic fluctuation, the molecule at (Q_1, F_1) has a chance of "jumping over" the energy barrier ΔE_{21} and transits to (Q_3, F_3); vice versa, the molecule at (Q_3, F_3) also has a possibility to overcome the energy barrier ΔE_{23} and transits to (Q_1, F_1). Here, ΔE_{21} and ΔE_{23} are the free energy difference between the two local minimum points and the local maximum respectively, and are calculated as follows:

$$\Delta E_{21} = F(Q_2) - F(Q_1), \Delta E_{23} = F(Q_2) - F(Q_3) \tag{4.6}$$

For the situation of curve b, under the influence of thermodynamic fluctuation, the LCE molecule is either at (Q_1, F_1) or (Q_3, F_3). Use the proportion coefficient x to represent the percentage of LCE molecules that are at $Q = Q_3$, then, the percentage of LCE molecules

that are at $Q = Q_1$ can be given by $(1 - x)$, and the overall average order parameter for the LCE $\bar{Q}$ can be given by:

$$\bar{Q} = (1 - x)\, Q_1 + xQ_3. \tag{4.7}$$

According to equation (4.3), $Q_1 = 0$, thus:

$$\bar{Q} = xQ_3 \tag{4.8}$$

Special cases include the situation in which $x = 0$, such a situation corresponds to curve a. Another special case is the situation in which $x = 1$, this situation corresponds to curve c.

Based on the above free energy analysis, when T changes, the local minimum point (Q_3, F_3) of the free energy changes its position. Meanwhile, the energy barriers ΔE_{21} and ΔE_{23}, as well as the relative position between (Q_1, F_1) and (Q_3, F_3) also change, this will cause the phase transition between one phase to another, which results in the change of x. Thus, the value of $\bar{Q}$ will change based on equation (4.8). The relationship between x and T will be discussed in the following section with the purpose to obtain the relationship between $\bar{Q}$ and T.

4.3 Relational Modeling of Proportional Coefficient and Temperature Based on Dynamic Equilibrium of Phase transition

In this section, transition of LCE molecules between the nematic phase and the isotropic phase is considered to obtain the relationship between x and T. Then, according to equation (4.8), the relationship between $\bar{Q}$ and T can be derived.

Here, consider the transition between the two phases is under dynamic equilibrium, that is, the speed of LCE molecules that transit from the nematic phase to the isotropic phase is equal

to the speed of LCE molecules that transit from the isotropic phase to the nematic phase. From Figure 4.4, the transition rate from (Q_1, F_1) to (Q_3, F_3) is W_{13}, and the transition rate from (Q_3, F_3) to (Q_1, F_1) is W_{31}. Thus, the following relationship can be obtained:

$$(1-x)\,W_{13} = xW_{31} \tag{4.9}$$

From equation (4.9), x is calculated as:

$$x = \frac{W_{13}}{W_{13} + W_{31}} \tag{4.10}$$

Usually, the transition rate W_{13} is proportional to the possibility of an LCE molecule at (Q_1, F_1) overcoming the energy barrier ΔE_{21}. Vice versa, W_{31} is proportional to the possibility of an LCE molecule at (Q_3, F_3) overcoming the energy barrier ΔE_{23}. These two possibilities are usually modelled using the Boltzman distribution [110], so the expression for W_{13} and W_{31} can be given as follows:

$$W_{13} = \delta_{13} e^{-\frac{\Delta E_{21}}{k_B T}},\ W_{31} = \delta_{31} e^{-\frac{\Delta E_{23}}{k_B T}} \tag{4.11}$$

where k_B is the Boltzmann constant, δ_{13} and δ_{31} are two proportional coefficients that will be given later.

Meanwhile, W_{13} and W_{31} should also be proportional to the total numbers of available states at (Q_3, F_3) and (Q_1, F_1), respectively. The total number of available states of a certain phase should be positively proportional to the width of the corresponding potential well (Here, the potential well refers to the region surrounding the local minimum). So the parameter δ_{13} and δ_{31} in equation (4.11) can be further given by:

$$\delta_{13} = \left(\frac{Q_2 - Q_1}{a_1}\right)^2,\ \delta_{31} = \left(\frac{Q_3 - Q_2}{a_3}\right)^2 \tag{4.12}$$

in which a_1 and a_3 are transition parameters to be determined through parameter identification.

Substitute equation (4.11) and (4.12) into (4.10) gives x in the range $T_2 < T < T_1$:

$$x = \frac{\left(\frac{Q_2 - Q_1}{a_1}\right)^2 e^{-\frac{\Delta E_{21}}{k_B T}}}{\left(\frac{Q_2 - Q_1}{a_1}\right)^2 e^{-\frac{\Delta E_{21}}{k_B T}} + \left(\frac{Q_3 - Q_2}{a_3}\right)^2 e^{-\frac{\Delta E_{23}}{k_B T}}} \tag{4.13}$$

Note that for $T > T_1$, $x = 0$. For $T < T_2$, $x = 1$. Substitute x into (4.8) gives the overall order parameter $\bar{Q}$ under different temperature T:

$$\bar{Q} = \begin{cases} 0, \quad T > T^* + \dfrac{B^2}{4A_0C} \\ Q_3, \quad T < T^* \\ \dfrac{\left(\frac{Q_2 - Q_1}{a_1}\right)^2 e^{-\frac{\Delta E_{21}}{k_B T}}}{\left(\frac{Q_2 - Q_1}{a_1}\right)^2 e^{-\frac{\Delta E_{21}}{k_B T}} + \left(\frac{Q_3 - Q_2}{a_3}\right)^2 e^{-\frac{\Delta E_{23}}{k_B T}}} Q_3, \quad \text{others} \end{cases} \tag{4.14}$$

in which Q_1, Q_2, Q_3 are given by equation (4.3), ΔE_{21} and ΔE_{23} are given by equation (4.6).

4.4 Deformation Calculation and the Overall Model

Based on the second law of thermodynamics, [49] discusses the relationship between the deformation λ of the LCE actuator and its average ordering parameter $\bar{Q}$, and gives the following equation:

$$\lambda \propto \left(1 + \alpha \bar{Q}\right)^{1/3} \tag{4.15}$$

where α is a deformation coefficient, and can be obtained through parameter identification. Here, mark the value of Q when $\lambda = 1$ as Q_0, then equation (4.15) can be rewritten as:

$$\lambda = \left(\frac{1 + \alpha \bar{Q}}{1 + \alpha \bar{Q}_0}\right)^{1/3} \tag{4.16}$$

Combining equation (4.16) with (4.14) gives the final expression for this physics based model of LCE:

$$\begin{cases} \bar{Q} = \begin{cases} 0, \quad T > T^* + \dfrac{B^2}{4A_0C} \\ Q_3, \quad T < T^* \\ \dfrac{\left(\dfrac{Q_2 - Q_1}{a_1}\right)^2 e^{-\frac{\Delta E_{21}}{k_B T}}}{\left(\dfrac{Q_2 - Q_1}{a_1}\right)^2 e^{-\frac{\Delta E_{21}}{k_B T}} + \left(\dfrac{Q_3 - Q_2}{a_3}\right)^2 e^{-\frac{\Delta E_{23}}{k_B T}}} Q_3, \quad \text{others} \end{cases} \\ \lambda = \left(\dfrac{1 + \alpha \bar{Q}}{1 + \alpha \bar{Q}_0}\right)^{1/3} \end{cases}, \tag{4.17}$$

In equation (4.17), Q_1, Q_2, Q_3 are the values of Q that corresponds to the local extremum of the LCE molecule's free energy, ΔE_{21} and ΔE_{23} are the energy barrier which prevents the LCE molecule to transit from one phase to another. They all have actual physical meanings, and can be further given by equation (4.3) and equation (4.6), respectively. k_B is the Boltzmann constant, which is a well-known constant in physics.

On the other hand, although the unknown phenomenological parameters $(A_0, B, C, T^*, a_1, a_3, \alpha)$ do have physical meanings, their values are hard to be directly measured. To obtain these values, parameter identification based on experimental data is necessary.

As mentioned in previous chapters, the deformation of the LCE actuator has a hysteretic characteristics highly coupled to environmental factors. This means that some of the unknown phenomenological parameters varies depending on the initial state and deformation history. Here, the unknown phenomenological parameters $(A_0, B, C, T^*, a_1, a_3, \alpha)$ are divided into two types: the non-history-dependant type, and the history-dependant type. The non-history dependant parameters include (A_0, B, α). For a certain LCE actuator, these parameters' values are the same for all deformation processes, and have little impact on the system's hysteresis.

As for the history-dependent parameters, they include (C, T^*, a_1, a_3). As a matter of fact, the free energy in (4.1) does not consider the weak coupling between the nematic polymers

and crosslinks. If we consider this coupling effect as a correction to the original model, there will be an additional quadratic term $C_{add}Q^4$ in the LCE molecule's free energy. Here, C_{add} is dependent on the shape of LCE. As a result, after taking into account this correction, the parameter C should be $C = C_0 + C_{add}$, which is history-dependent. Here, C_0 corresponds to the situation where the coupling is neglected. T^* is the supercooling temperature, which is related to the inner structure of the system. Furthermore, the coupling between the nematic polymers and crosslinks modifies the free energy, so the transition parameters a_1 and a_3 will also be modified, making these two terms history-dependent.

These history-dependent parameters are the reflection of the system's hysteretic nonlinearities. To describe their dependencies on the system's history more precisely, we use the subscript r to represent the process of temperature raising, and use the subscript c to represent the process of temperature cooling, and these parameters can be re-listed as $(C_r, C_c, T_r^*, T_c^*, a_{1,r}, a_{3,r}, a_{1,c}, a_{3,c})$.

4.5 Parameter Identification of the Model

Typical methods for model parameter identification include methods based on separated physical experiments [111], computer aided design techniques [111], regression analysis [112], neural network based methods [113], intelligent optimization [114], etc.. These methods have their own unique features and advantages. Here, the unknown phenomenological parameters $(C_r, C_c, T_r^*, T_c^*, a_{1,r}, a_{3,r}, a_{1,c}, a_{3,c})$ are identified based on the nonlinear least squares method [115] due to its simplicity and good convergence. The nonlinear least squares method is a type of regression analysis, which deals with identifying the parameters for nonlinear models. In this method, the effectiveness of the parameter identification is evaluated by the root mean square error (RMSE):

$$\sigma = \frac{1}{N}\sqrt{\sum_{j=1}^{N}\left(\lambda_j - \lambda_{j,exp}\right)^2} \times 100\% \tag{4.18}$$

in which N is the total number of data. λ_j and $\lambda_{j,exp}$ are the λ corresponding to the jth data point from the theoretical simulation and experiments, respectively.

For the nonlinear least squares method, due to the nonlinearity of the model, the estimation of the parameters cannot use the conventional method of calculating the extreme values of the multivariate function, but rather uses iterative algorithms. The basic idea of the intelligent iterative algorithm is to set the parameters to certain initial values first, and update their values iteratively to ensure that the root mean square error converges to zero.

Typical iterative algorithms include the Gauss-Newton algorithm [116], the gradient descent method [117], the Levenberg-Marquardt algorithm [118], etc.. In our experiment, the Levenberg-Marquardt (LM) algorithm is utilized. The LM algorithm is more like an interpolation of the Gauss-Newton algorithm and the gradient descent method. In this method, a damping factor is introduced to adjust the value of the step size in each iteration based on the current root mean square error σ. Compared with other algorithms, the LM algorithm has better robustness, which means that it can work better to find the final solution when the initial values of the parameters are far away from the actual values.

Specific identification steps are given as follows.

Step 1**:** The parameters $p = (A_0, B, C_r, C_c, T_r^*, T_c^*, a_{1,r}, a_{3,r}, a_{1,c}, a_{3,c}, \alpha)$ are given initial values p_0 to start the iteration.

Step 2**:** The root mean square error σ in equation (4.18) are calculated to evaluate the current parameter values.

Step 3**:** If the root mean square error is small enough, or if the number of iterations reaches a maximum, the iteration stops, and the current p gives the values for the estimated parameters. Otherwise, the process goes to Step 4.

Step 4**:** Update the values of p by $p + \delta p$, in which the variations of the parameter values δp are calculated using the LM algorithm:

$$\left(J^{\mathrm{T}} J + \mu I\right) = J^{\mathrm{T}} \left(ve_{exp} - ve\right). \tag{4.19}$$

In equation (4.19), ve_{exp} is the column vector of all experimental data $\lambda_{j,exp}$, and ve is the column vector of all calculated data λ_j, $j = 1, 2, ..., N$. J is the Jocobian matrix of ve

over parameters p, $J = \partial ve/\partial p$. I is the identity matrix, and μ is the damping factor. After updating the parameters according to equation (4.19), the process goes back to step 2.

In the end, this iteration process gives an estimation of parameters p.

4.6 Experimental Verification

Based on the experimental platform in Figure 3.3, experiments are performed using input signals which sets the power efficiency P of the programmable laser, in the following form:

$$P = \begin{cases} Amp \sin \dfrac{\pi}{2T_h} t + 1.5, & t < T_h \\ 0, & \text{others} \end{cases} \tag{4.20}$$

in which Amp is the amplitude, T_h is the total stimulation time. At $t = 0$, the light is turned on, and will be turned off at $t = T_h$. By setting different values for Amp and T_h, different power efficiency P can be generated.

In actual experiments, we first use a set of experiments to identify the parameters (A_0, B, C, T^*, a_1, a_3, α) in equation (4.17) using the nonlinear least squares method. Since the values of the non-history-dependent parameters (A_0, B, α) should be the same in different experiments. We then use another set of experiments with different Amp and T_h to further compare (A_0, B, α). In these sets of experiments, the search ranges for the non-history-dependent parameters are fixed according to the previous set of experiments. The performances of the proposed model for different experiments are compared to evaluate its effectiveness.

4.6.1 Experimental Results

Experiments are performed using input signals with $Amp = 0.2$ mA and different T_h (30, 40, 50) s, respectively. In all cases, $Q_0 = 1$. Furthermore, the Boltzmann constant $k_B = 1.38 \times 10^{-23}$ m^2 kg s^{-2} K^{-1}.

Parameter identification is performed to obtain the unknown parameters in equation (4.17) based on the nonlinear least squares method introduced in previous sections. For the case in which $Amp = 0.2$ mA and $T_h = 30$ s, the phenomenological parameters are identified as follows:

$$\begin{cases} A_0 = 5.58 \times 10^{-22}\ \mathrm{J \cdot K^{-1}}, B = 7.70 \times 10^{-20}\ \mathrm{J}, \\ T_r^* = 305.0\ \mathrm{K}, T_c^* = 291.9\ \mathrm{K}, \\ C_r = 7.91 \times 10^{-20}\ \mathrm{J}, C_c = 6.76 \times 10^{-20}\ \mathrm{J}, \\ a_{1,r} = 1.68, a_{3,r} = 10.60, a_{1,c} = 0.93, a_{3,c} = 3.53, \\ \alpha = 1.91 \end{cases} \tag{4.21}$$

The historic dependencies of the parameters C, T^*, a_1 and a_3 are complicated, and are beyond the content of this paper, so they will not be given for the other two cases.

For this case, the temperatures T_1 and T_2 which correspond to the boundary situations can be calculated according to equations (4.4) and (4.5). It should be noted that since C and T^* are history-dependent, the values of T_1 and T_2 vary in different process. Here, we use T_{1r} and T_{2r} as the values for T_1 and T_2 in the temperature rising process, and we use T_{1c} and T_{2c} as the values for T_1 and T_2 in the temperature cooling process, their values are:

$$\begin{cases} T_{1r} = 338.6\ \mathrm{K}, T_{2r} = 305.0\ \mathrm{K} \\ T_{1c} = 331.2\ \mathrm{K}, T_{2c} = 291.9\ \mathrm{K} \end{cases} \tag{4.22}$$

The above equation shows that the temperatures at the boundaries T_{ir} for the temperature rising process is around 10 K higher than the corresponding T_{ic} for the temperature cooling process ($i = 1, 2$), this exhibits the hysteresis of the deformation of LCE.

Figure 4.5 gives comparisons of the experimental and theoretical results under input signals with different heating time T_h. Figure 4.5 exhibits a very obvious hysteresis behavior. As T_h becomes larger, LCE exhibits more obvious deformation, that is, the hysteresis loop to become larger. This feature shows that the hysteretic characteristic of the deformation of LCE has a high dependency on input signals.

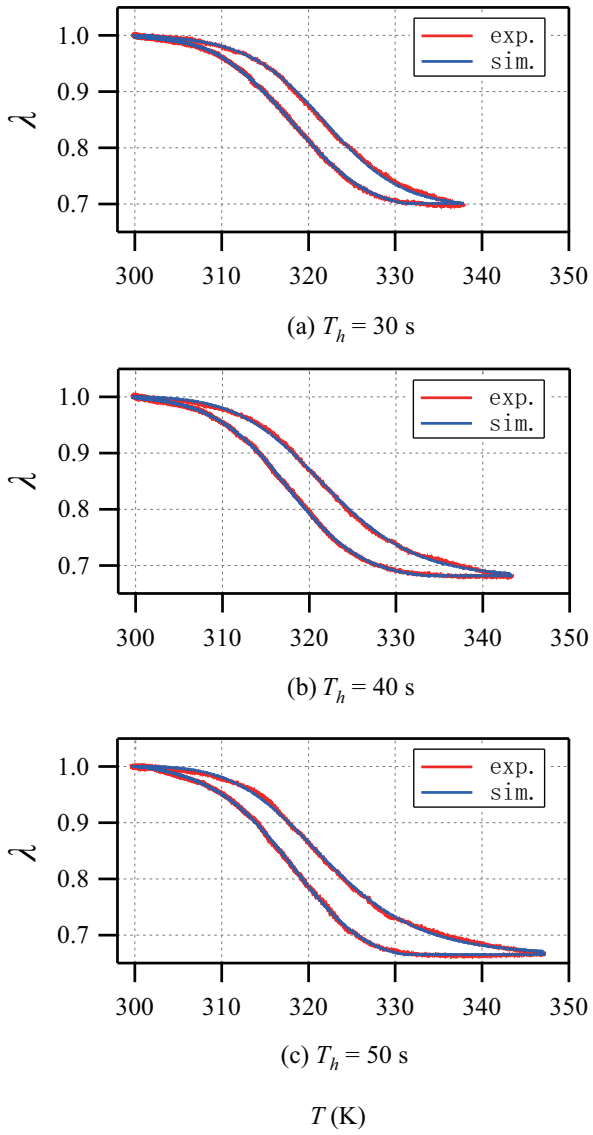

Figure 4.5: Experimental results for $Amp = 0.2$ mA, $T_h = 30, 40, 50$ s

Moreover, in Figure 4.5, it can be seen that in the low temperature range in which $T < T_2$, the deformation comes to saturation. That is, the curves become “flat" in this range. In this situation, the LCE molecules are all in the nematic state. Similarly, in the high temperature range $T > T_1$, there should also be saturation. However, in Figure 4.5(a), saturation in the high temperature range is not very obvious, while in Figure 4.5(b) it is more obvious, and Figure 4.5(c) has the most obvious saturation in the high temperature range. This reason is

that, in Figure 4.5(a), the highest temperature is only around the value of T_{1r}, so the $T > T_1$ region is not obvious. When T_h increases, the highest temperature becomes larger than T_{1r}, and the saturation in the high temperature range becomes more obvious.

On the other hand, we mainly use the root mean square error (RMSE) to give the prediction errors and to evaluate the performance of the proposed model. We also use the symmetric mean absolute percentage error (SMAPE) and the normalized RMSE (NRMSE) to view the prediction errors from different aspects. RMSE gives estimations of the differences between the model and actual experiments, and can be calculated by equation (4.18). SMAPE is an evaluation of the relative accuracy of the model, and can be calculated by:

$$SMAPE = \frac{\sum_{j=1}^{N} |\lambda_j - \lambda_{j,exp}|}{\sum_{j=1}^{N} (\lambda_j + \lambda_{j,exp})} \times 100\% \tag{4.23}$$

The NRMSE is the estimation error related to the observed range of actual data, it facilitates comparison between datasets with different scales, and can be given by:

$$NRMSE = \sqrt{\frac{\sum_{j=1}^{N} (\lambda_j - \lambda_{j,exp})^2}{\sum_{j=1}^{N} \left(\lambda_{j,exp} - \bar{\lambda}_{exp}\right)^2}} \times 100\% \tag{4.24}$$

Table 4.1 gives the RMSE, the SMAPE and the NRMSE for all cases. The RMSEs and SMAPEs for all cases are in the order of 10^{-3}, the NRMSEs for all cases are in the order of 10^{-2}. These results show that the prediction errors for the deformation of LCE are very small, and that the model works well with different input signals. This proves the effectiveness of the proposed model.

From the discussions in previous section, the values of A_0, B and α should be non-history-dependent, which means that they should not depend on the input signal and the deformation process. The values of the parameters A_0, B and α obtained from parameter identification for each case are given in Table 4.2. According to Table 4.2, it is obvious that variations of A_0 and B for each case are small, which match the proposed model. Meanwhile, α shows an increase as T_h becomes higher. This variation is actually still acceptable, a more detailed

Table 4.1: Evaluation of Preformance for $Amp = 0.2$ mA, $T_h = 30, 40, 50$ s

T_h	30	40	50
RMSE (%)	0.22	0.23	0.24
SMAPE (%)	0.10	0.10	0.11
NRMSE (%)	2.5	2.2	2.0

discussion will be given in the following subsection.

Table 4.2: A_0, B and α for each case

T_h	30	40	50
A_0 (10^{-22})	5.58	5.71	5.81
B (10^{-20})	7.70	7.70	7.68
α	1.91	2.16	2.40

4.6.2 Model Verification

In this section, two extra sets of experiments are performed with input signals of amplitudes Amp different from the previous section. These two sets of experiments have a input signal with $Amp = 0.25$ mA, and T_h of (25, 35) s, respectively. Furthermore, when performing parameter identification for these two sets of experiments, we set the searching range of A_0, B and α according to the values given by Table 4.2 to prove that the previous discussions on non-history dependent parameters are theoretically correct.

Figure 4.6 gives results for these two sets of experiments. The results also exhibit high hysteretic nonlinearity. The evaluation of performance for these two sets of experiments are

given by Table 4.3. It can be shown that even though we have fixed the searching range for parameters A_0, B and α during parameter identification, the prediction errors still have the same orders when compared with previous experiments (Table 4.1). This shows the validity and high accuracy of the proposed model.

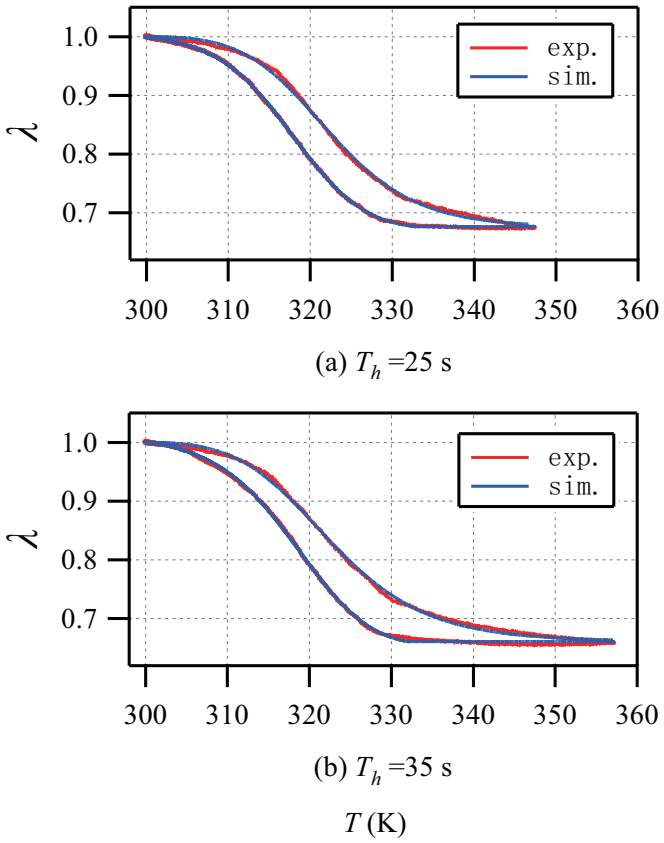

Figure 4.6: Experimental results for $Amp = 0.25$ mA, $T_h = 25, 35$ s

The values of A_0, B and α for each case are provided in Table 4.4. According to both Tables 4.2 and 4.4, we can see that A_0 and B for all five experiments have small variations. Meanwhile, experiments with a larger input energy (larger Amp or higher T_h) has a larger α.

As a matter of fact, based on equation (4.16), even though in these experiments α has a variation from 1.9 to 2.4, such a variation only has small influence on the deformation λ.

Table 4.3: Evaluation of Performance for $Amp = 0.25$ mA, $T_h = 25, 35$ s

T_h	25	35
RMSE (%)	0.23	0.28
SMAPE (%)	0.10	0.12
NRMSE (%)	2.1	2.2

Table 4.4: A_0, B and α for each case

T_h	25	35
A_0 (10^{-22})	5.71	5.51
B (10^{-20})	7.70	7.70
α	2.22	2.46

Take the situation, in which $\bar{Q} = 0.5$, $Q_0 = 1$, as an example, according to equation (4.16), $\lambda(\alpha = 1.9) = 0.876$, and $\lambda(\alpha = 2.4) = 0.865$, this difference has the same order of magnitude as the prediction errors. This shows that the variation in the identification results of α is acceptable within the margin of the prediction error of λ. As a result, in these experiments, we can use an average value $\alpha = 2.2$ to represent the actual value of α, this is reasonable within the margin of the prediction error.

To conclude, by comparing with experimental data, this proposed modeling method is effective and can be utilized to quantitatively describe the deformation process of LCE. Meanwhile, this model can also provide a reflection of the essential physics underlying in the deformation of LCE, the modeling of more advanced model can use this modeling strategy as a basis.

4.7 Concluding Remarks

This chapter proposes basic modeling scheme for the modeling of the LCE actuator. In the modeling scheme, the average order parameter is introduces to quantitatively evaluate the phase change of LCE molecules, and the modeling of the LCE actuator is divided into into two independent steps. This basic modeling scheme works as a guidance for the modeling of the LCE actuator.

Based on the modeling scheme, a basic model to give a relatively simple temperature-deformation relationship of the LCE actuator based on the consideration of dynamic equilibrium during the phase transition process is proposed. The model also reflects the physical nature of the LCE actuator. To build the relationship between the average order parameter and the temperature, the free energy of the system is analyzed using the Landau-de Gennes expansion for nematic polymers, and the phase transition process of LCE molecules is discussed using thermodynamic analysis. The relationship between the deformation and the average order parameter is then given according to thermodynamic analysis. These two relationships are then combined together to constitute a complete model for the LCE actuator.

In this modeling method for LCE, unknown parameters are categorized into history-dependent parameters, whose values vary in different deformation process, and non-history-dependent parameters, whose values should stay the same in different deformation processes. These parameters are all identified using the nonlinear least-squares method with experimental data. The identified values of the non-history-dependent parameters under different experimental sets are compared to show the validity of the proposed method.

However, the assumption that the phase transition of LCE molecule between two phases is under dynamic equilibrium would lead to a lack of details in describing this process, and thus brings modeling errors into the description of LCE's deformation. The obtained relationship (4.17) is a static equation, and has difficulties in describing the dynamic phase transition process. To give a more accurate description of this deformation, the dynamic process of

phase transition of LCE molecules during the deformation process should to be addressed to make further improvements.

Chapter 5

Modeling for LCE Actuator Considering Dynamic Process of Phase Transition

In previous chapter, a basic model for LCE actuator is proposed based on assuming that the phase transition process is under dynamic equilibrium. This is a commonly made assumption to deal with thermodynamic problems, and the model can provide a simple analytical expression to give a rough description on the deformation of the LCE actuator. However, this assumption cannot completely reflect the dynamic phase transition process, and will lead to inaccuracy on the modeling results. Based on the above consideration, the previous model needs to be improved to obtain a model that can give a better description of LCE's hysteresis. By analysing the dynamic process of the phase transition of LCE molecules, an improved model that describes LCE's hysteresis with high accuracy can be obtained.

In this chapter, we deliver a physics based model for LCE actuator by considering the dynamic process of the phase transition of LCE molecules. The modeling scheme for this model is still given by Figure 4.2, and the relationships that are given by equation (4.8) and (4.16) remain the same, but the relationship between the proportion coefficient x and temperature T is re-discussed by taking into consideration the dynamic process of LCE molecules' phase transition.

5.1 Relational Modeling of Proportional Coefficient and Temperature Considering Dynamic Process of Phase Transition

According to Figure 4.3, when $T < T_2$, the free energy of LCE molecules only has one local minimum (Q_3, F_3), in this situation, $x = 1$, and LCE is in the nematic phase. Similarly, when $T > T_1$, the free energy of LCE molecules only has a local minimum (Q_1, F_1), in this situation, $x = 0$, and LCE is in the isotropic phase.

As for $T_2 < T < T_1$, there are two local minimums, and there are possibilities that LCE molecules might transit from one phase to another. As shown in Figure 4.4, the rate of LCE molecules transiting from $Q = Q_1$ to $Q = Q_3$ is W_{13}, and the rate of LCE molecules transiting from $Q = Q_3$ to $Q = Q_1$ is W_{31}.

It should be noted that in this chapter, the dynamic process of the phase transition is considered, it is a totally different approach from the previous chapter, in which dynamic equilibrium of thermal phased transition is considered. Thus, the definitions of transition rates W_{13} and W_{31} are slightly different from W_{13} and W_{31} in the previous chapter.

When the temperature varies by dT, the change of the proportion coefficient x can be written as:

$$dx = W_{13}dT - W_{31}dT \tag{5.1}$$

Take W_{13} as an example, this transition rate should be dependent upon the following factors:

(1) W_{13} should be directly proportional to the total number of LCE molecules at $Q = Q_1$, which means $W_{13} \propto (1 - x)$.

(2) As shown in Figure 4.4, in order to transit from $Q = Q_1$ to $Q = Q_3$, LCE molecules have to overcome an energy barrier ΔE_{21}. Here, we can use Boltzmann distribution to describe the distribution of LCE molecules. Then, according to the Boltzmann distribution,

the transition rate $W_{13} \propto e^{-\frac{\Delta E_{21}}{k_B T}}$.

(3) W_{13} should be related to the total number of available states at $Q = Q_3$. This total number of available states can be quantitatively evaluated by $\Delta_{32} = Q_3 - Q_2$, which is the distance from the local minimum $Q = Q_3$ to the energy barrier $Q = Q_2$. When $\Delta_{32} = 0$, the total number of available states at $Q = Q_3$ is 0, and W_{13} should be 0. Here, we can approximate the relationship between W_{13} and Δ_{32} by a polynomial of Δ_{32} near the zero point.

Based on the above considerations, the final expression for W_{13} can be given as:

$$\begin{aligned} W_{13} = (C_{f1}\Delta_{32} + C_{f2}\Delta_{32}^2 + C_{f3}\Delta_{32}^3 + \\ \cdots)\,(1-x)\,e^{-\frac{\Delta E_{21}}{k_B T}} \end{aligned} \tag{5.2}$$

Similarly, for W_{31}:

$$\begin{aligned} W_{31} = (C_{r1}\Delta_{21} + C_{r2}\Delta_{21}^2 + C_{r3}\Delta_{21}^3 + \\ \cdots)\,x e^{-\frac{\Delta E_{23}}{k_B T}} \end{aligned} \tag{5.3}$$

In equations (5.2) and (5.3), C_{fi}, C_{ri} $(i = 1, 2, 3, \cdots)$ are constants. Meanwhile, Δ_{32}, ΔE_{21},Δ_{21}, ΔE_{32} are given by the following equations:

$$\begin{aligned} \Delta_{32} = Q_3 - Q_2, \Delta E_{21} = F(Q_2) - F(Q_1) \\ \Delta_{21} = Q_2 - Q_1, \Delta E_{23} = F(Q_2) - F(Q_3) \end{aligned} \tag{5.4}$$

When we deal with equations (5.2) and (5.3), some high order terms in the polynomial can be neglected for simplification. When doing so, the following facts should be taken into consideration: although the transitions between the two phases always exist, the overall trend of the proportional coefficient x is to decrease when the temperature T rises. Thus, in this process, the transition from $Q = Q_3$ to $Q = Q_1$ is dominant. Similarly, when T falls, the transition from $Q = Q_1$ to $Q = Q_3$ is dominant. As a result, when we ignore the high order terms in equations (5.2) and (5.3), for the transition that is dominant, we keep the first and second order terms. Meanwhile, for the transition that is not dominant, we only keep the first term.

Take W_{13} as an example, it should be noted that, since the dominant phase transition process is different for temperature rising and falling process at a certain temperature T, values of W_{13} are different for these two processes. Thus, according to equation (5.2), values of parameter C_{fi}, $(i = 1, 2, \cdots)$ are also different for temperature rising and temperature falling process. Similar fact exists for C_{ri} $(i = 1, 2, \cdots)$ in equation (5.3). This results in the hysteresis characteristic of the LCE actuator.

Thus, based on the above consideration, according to equations (5.1), (5.2), (5.3), we can obtain the following equation for dx:

$$dx = \begin{cases} {}^{r}C_{f1}\,{}^{r}\Delta_{32}\,(1-x)\,e^{-\frac{{}^{r}(\Delta E_{21})}{k_B T}}dT - ({}^{r}C_{r1}\,{}^{r}\Delta_{21} + \\ \qquad {}^{r}C_{r2}\,{}^{r}\Delta_{21}^{2})\,xe^{-\frac{{}^{r}(\Delta E_{23})}{k_B T}}dT, \quad dT > 0 \\ \left({}^{f}C_{f1}\,{}^{f}\Delta_{32} + {}^{f}C_{f2}\,{}^{f}\Delta_{32}^{2}\right)(1-x)\,e^{-\frac{{}^{f}(\Delta E_{21})}{k_B T}}dT - \\ \qquad {}^{f}C_{r1}\,{}^{f}\Delta_{21}xe^{-\frac{{}^{f}(\Delta E_{23})}{k_B T}}dT, \quad dT < 0 \end{cases}. \tag{5.5}$$

Equation (5.5) gives the relationship between the temperature T and the proportion coefficient x. Here, the superscript r represents the temperature rising process, and the superscript f represents the temperature falling process. It should be noted that besides C_{fi}, C_{ri} $(i = 1, 2, \cdots)$, values of A_0, B, C are also different in temperature rising and temperature falling process, which is reflected in the values of ΔE_{21} and ΔE_{23}. According to equation (5.5), at the same temperature, dx is different for temperature rising and temperature falling process, this difference results in a hysteretic characteristic in the input-output response of the LCE actuator.

5.2 The Overall Model Considering Dynamic Process of Phase Transition

The relationship between the deformation λ of the LCE actuator and its average ordering parameter $\bar{Q}$ can still be given by equation (4.16). Notice that usually $Q_0 = 1$. The overall

model of the LCE actuator can be given by:

$$\begin{cases} \lambda = \left(\frac{1+\alpha\bar{Q}}{1+\alpha}\right)^{1/3}, \\ \bar{Q} = xQ_3 \end{cases} \tag{5.6}$$

in which

$$Q_3 = \frac{B + \sqrt{B^2 - 4A_0\left(T - T^*\right)C}}{2C} \tag{5.7}$$

and the variation of x should satisfy

$$dx = \begin{cases} {}^rC_{f1}\,{}^r\Delta_{32}\left(1-x\right)e^{-\frac{{}^r(\Delta E_{21})}{k_B T}}dT - ({}^rC_{r1}\,{}^r\Delta_{21} + \\ \quad {}^rC_{r2}\,{}^r\Delta_{21}^2\right)xe^{-\frac{{}^r(\Delta E_{23})}{k_B T}}dT, \quad dT > 0 \\ \left({}^fC_{f1}\,{}^f\Delta_{32} + {}^fC_{f2}\,{}^f\Delta_{32}^2\right)\left(1-x\right)e^{-\frac{{}^f(\Delta E_{21})}{k_B T}}dT - \\ \quad {}^fC_{r1}\,{}^f\Delta_{21}xe^{-\frac{{}^f(\Delta E_{23})}{k_B T}}dT, \quad dT < 0 \end{cases}. \tag{5.8}$$

Expressions (5.6) to (5.8) give the overall quantitative model of the LCE actuator which describes the relationship between LCE's deformation and its temperature.

In the above final expression, terms Δ_{32}, ΔE_{21},Δ_{21}, ΔE_{32} are given by equation (5.4), terms Q_1, Q_2 and Q_3 are given by equation (4.3). k_B is the well-known Boltzman Constant. Meanwhile, the unknown model parameters can be listed by the parameter vector p, given as follows:

$$\begin{aligned} p = ({}^rA_0, {}^rB, {}^rC, {}^fA_0, {}^fB, {}^fC, T^*, \\ {}^rC_{r1}, {}^rC_{r2}, {}^rC_{f1}, {}^fC_{r1}, {}^fC_{f1}, {}^fC_{f2}, \alpha) \end{aligned} \tag{5.9}$$

whose values are determined by parameter identification.

5.3 Two-step Parameter Identification Strategy for Model Parameters

In the overall model (5.6), the values of the parameters given by p are unknown. To obtain these values, one method is to identify the parameters based on experimental data. Since

p has a total of 14 elements, its solution space is relatively large, which brings difficulties in searching for the right solutions. Furthermore, parameter identification needs to be performed for different experimental data set. The above factors bring heavy computational burden during parameter identification process.

In this section, a two-step parameter identification strategy is used to reduce the calculation of parameter identification, and to obtain the values of p for all data sets efficiently.

5.3.1 Two-Step Parameter Identification Strategy

The two-step parameter identification strategy utilizes both DE algorithm and nonlinear least squares method to achieve parameter identification. Here, the DE algorithm is a type of intelligent optimization method in which the parameters start at a set of various initial candidate solutions and evolve through iterations. We can use its strong searching ability to narrow down the solution space to somewhere near the global optimum for finding a rough solution. Meanwhile, the nonlinear least squares method only has one candidate solution, so when compared with the DE algorithm, the nonlinear least squares method does not need multiple solution sets, and has simpler calculation.

Conventionally, if we perform parameter identification for all experimental data based on DE algorithm solely, searching for global optimum for all data sets would be time consuming. On the other hand, using just nonlinear least squares method is hard to obtain the correct values. To solve this, we introduce a two-step parameter identification strategy to utilize the searching ability of the DE algorithm as well as the calculation efficiency of the nonlinear least square method to effectively identify model parameters. For the convenience of description, we use $(p_1, p_2, \cdots)$ to represent a set of the solution candidates of the parameter vector p, and $\Sigma_i = \left\{ \left(T^i_{j,exp}, \lambda^i_{j,exp} \right), j = 1, 2, \cdots, N \right\}$ $(i = 1, 2, \cdots)$ to represent the ith set of experimental data. Here, $\left(T^i_{j,exp}, \lambda^i_{j,exp} \right)$ is the jth data point in the ith data set, and N is the total number of data in this set. In the first step, we select a random data set $\Sigma_o \in \{\Sigma_i, i = 1, 2, \cdots\}$ to perform parameter identification based on the DE algorithm. This parameter identification

process starts from a randomly initialized set of solution candidates $(p_1^0, p_2^0, \cdots)$, in which the subscript 0 represents the initial generation. Through the optimization process, we can find a rough solution p_r. This procedure utilizes the DE algorithm's searching ability to narrow down the solution space to somewhere near the optimum value. In the second step, for any set of experimental data Σ_i, we use parameter identification based on the nonlinear least squares method to obtain the solution for p. For this process, we set p_r as the initial value of the solution candidate. Since this p_r should be near the global optimum, we can obtain the final identified values p_{opt} effectively.

The whole scheme of this two-step parameter identification strategy can be shown in Fig. 5.1. To sum up, the first step of this strategy works to find the approximate range of the global optimum, then the second step of this strategy works to solve the final identified values based on the range given by the first step.

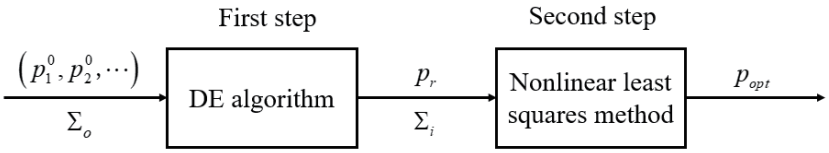

Figure 5.1: Scheme of the two-step parameter identification strategy

For both methods, the solution in each iteration is evaluated by the RMSE σ given by equation (4.18). For a specific set of candidate solutions, the smaller $RMSE$ is, the closer the solutions are to the object values.

5.3.2 Procedure of the Two-step Parameter Identification

The procedure of the two-step parameter identification strategy based on the DE algorithm and nonlinear least squares method are given as follows.

Step 1**:** Select a set of experimental data $\Sigma_o \in \{\Sigma_i, i = 1, 2, \cdots\}$ as the initial reference for parameter identification.

Step 2**:** For Σ_o, initialise a set of candidate solutions $(p_1^0, p_2^0, \cdots)$ for p as the 0th generation of solution candidates. Calculate $RMSE$ for each candidate solutions according to equation (4.18).

Step 3**:** For the kth generation of the candidate solutions $(k = 1, 2, \cdots)$, if the minimum $RMSE$ is smaller than a certain constant ϵ_1, or if the number of iterations k reaches a maximum number M_1, the iteration stops. Set the candidate solution corresponding to the smallest $RMSE$ to be the rough solution p_r that we're looking for. The process goes to *Step* 5. Otherwise, the process goes to *Step* 4.

Step 4**:** Through evolution rules with a crossover probability CR and the differential weight DW, a new set of solution candidates are obtained. The $(k+1)$th generation of the candidate solutions $\left(p_1^{k+1}, p_2^{k+1}, \cdots\right)$ are sorted out from the new set as well as the kth generation of solution candidates. The process then goes back to *Step* 3.

Step 5**:** For any set of experimental data $\Sigma_i = \left\{\left(T_{j,exp}^i, \lambda_{j,exp}^i\right), j = 1, 2, \cdots, N\right\}$ $(i = 1, 2, \cdots)$, use the nonlinear least squares method to identify the values of the unknown parameters. Here, set the initial candidate solution $p = p_r$, which is near the real solution p_{opt}.

Step 6**:** Based on the nonlinear least squares method, the candidate solution is updated and evaluated until its $RMSE$ reaches a minimum value, or until the number of iterations l reaches a maximum number M_2.

Step 7**:** The final solution obtained in *Step* 6 is the solution p_{opt} we're looking for.

Here, ϵ_1, M_1 and M_2 are constants. The obtained p_{opt} gives the final identification results for the model parameters in experimental set Σ_i $(i = 1, 2, \cdots)$. This whole process can be shown in Figure 5.2. For this parameter identification process, we combine the advantages of the DE algorithm and the nonlinear least squares method, respectively, to obtain a strategy with fast convergence to optimum solution and relatively simpler mathematical complexity.

It should be noted that in *Step* 3, if when the iteration time reaches the maximum number M_1 while the minimum $RMSE$ is still much larger than ϵ_1, it is likely that the searching for global optimum has fall into the wrong direction, and the process should re-start from the

beginning with another random set of initial candidate solutions. As for *Step* 6, since the initial candidate solution is around the final value, it is unlikely that there will be situation in which the iteration number reaches the maximum M_2.

5.4 Experimental Verification and Comparisons

Based on the experimental platform in Figure 3.3, experiments are performed using input signals with fixed amplitude of 0.4 mA, and different duration times $T_h = (16, 17, 18, 19, 20, 21)$ s. This range of T_h is selected to ensure that we can observe a complete hysteresis loop as well as its dependency on the variation of input signals. In all cases, $\bar{Q}_0 = 1$, and the Boltzmann constant $k_B = 1.38 \times 10^{-23}$ m^2 kg s^{-2} K^{-1}. For the parameter identification process, we set $\epsilon_1 = 10^{-4}$. For the DE algorithm, we set the crossover probability $CR = 0.9$ and the differential weight $DW = 0.8$. The data set with $Amp = 0.4$ mA and $T_h = 20$ s is selected as the initial set Σ_o.

The values of parameters in the parameter vector p_r is determined based on the DE algorithm for Σ_o:

$$\begin{cases} {}^{r}A_0 = 2.3 \times 10^{-22}\ \mathrm{J \cdot K^{-1}}, \\ {}^{f}A_0 = 6.0 \times 10^{-22}\ \mathrm{J \cdot K^{-1}}, \\ {}^{r}B = 3.5 \times 10^{-20}\ \mathrm{J}, {}^{f}B = 4.5 \times 10^{-20}\ \mathrm{J}, \\ {}^{r}C = 2.0 \times 10^{-20}\ \mathrm{J}, {}^{f}C = 2.6 \times 10^{-20}\ \mathrm{J}, \\ T^* = 307\ \mathrm{K}, \alpha = 4.5 \\ {}^{r}C_{r1} = 29\ \mathrm{K^{-1}}, {}^{r}C_{r2} = 8.6 \times 10^{-5}\ \mathrm{K^{-1}}, \\ {}^{f}C_{f1} = 5.0 \times 10^{-4}\ \mathrm{K^{-1}}, {}^{f}C_{f2} = 0.3\ \mathrm{K^{-1}} \\ {}^{r}C_{f1} = 0.7\ \mathrm{K^{-1}}, {}^{f}C_{r1} = 1100\ \mathrm{K^{-1}} \end{cases} \tag{5.10}$$

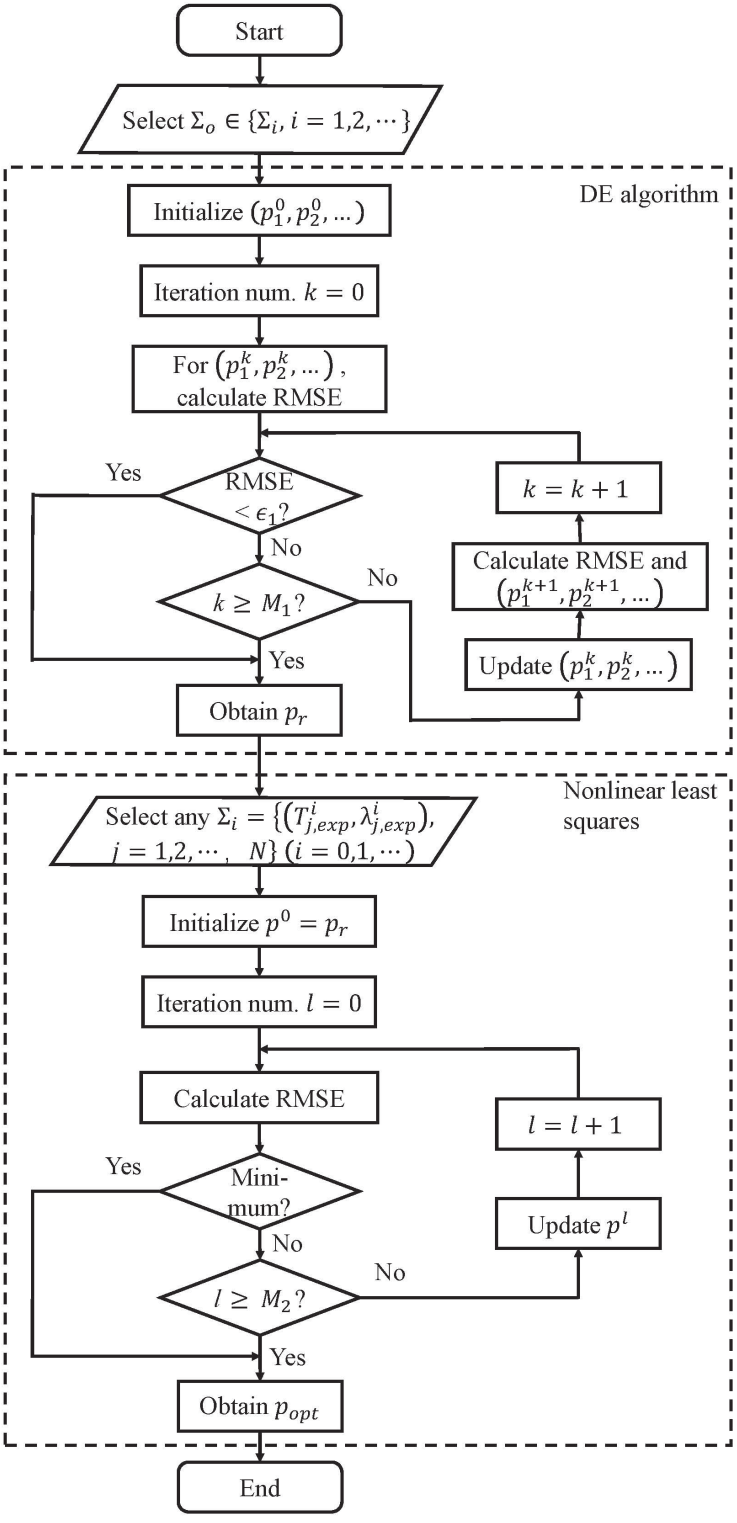

Figure 5.2: The procedure of parameter identification

We use the p_r given by equation (5.10) as the initial solution candidate, and perform parameter identification using the nonlinear least squares method for all experimental data. Figure 5.3 and 5.4 give the results which show the comparisons between the experimental data (exp.) and theoretical simulations (sim.) under different input signals. In these figures, the red line is the experimental data of LCE's deformation, and the blue line is the simulated results based on the proposed model. Figure 5.3 and 5.4 show clear hysteretic loops of LCE's deformation. Also, with larger T_h, which corresponds to lower frequency, the hysteretic loop becomes larger.

Here, we also evaluate the performance of the proposed model based on the RMSE, the SMAPE, and the NRMSE. Table 5.1 gives the RMSEs, the SMAPEs and the NRMSEs for all cases. The RMSEs for all cases are in the order of 10^{-5}, the SMAPEs for all cases are in the order of 10^{-3}, and the NRMSEs for all cases are in the order of 10^{-2}. It can be seen that these values are small and consistent for all cases, which means that the proposed model matches well with experimental data, and works well for different situations.

Table 5.1: Performance evaluation under different inputs

T_h	16	17	18	19	20	21
RMSE ($\times 10^{-3}$%)	6.0	5.4	5.3	5.4	5.6	5.6
SMAPE (%)	0.30	0.27	0.28	0.28	0.30	0.30
NRMSE (%)	4.1	3.6	3.5	3.4	3.6	3.6

So far, besides the work in Chapter 4, no other works have been made to provide an analytical expression to describe the deformation of the LCE actuator. To show that this model indeed improves by considering the dynamic process, we provide a comparison between the proposed model and the previous presented model in Chapter 4 for an input signal of Amp = 0.4 mA and Th = 20 s, as shown in Fig. 5.5. Here, the added green line (pre.) is the simulated results based on the previous model in Chapter 4, in which the dynamic

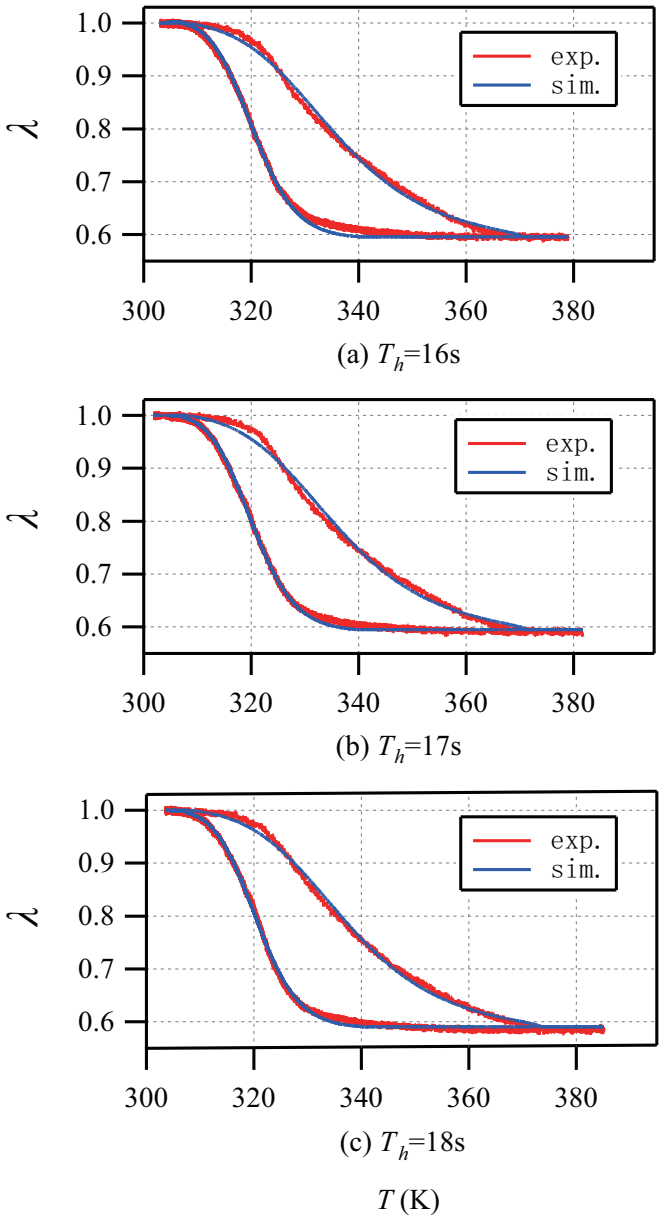

Figure 5.3: Experimental results for T_h = 16, 17, 18 s

process of the phase transition of LCE molecules is not considered. It should be noted that the temperature T in experiments ranges from 300 K to 390 K, and deformation λ ranges from 0.55 to 1, which cover a wide range. As a result, the difference of curves in Fig. 5.5 might seem small. In order to show the improvement of the proposed model more clearly,

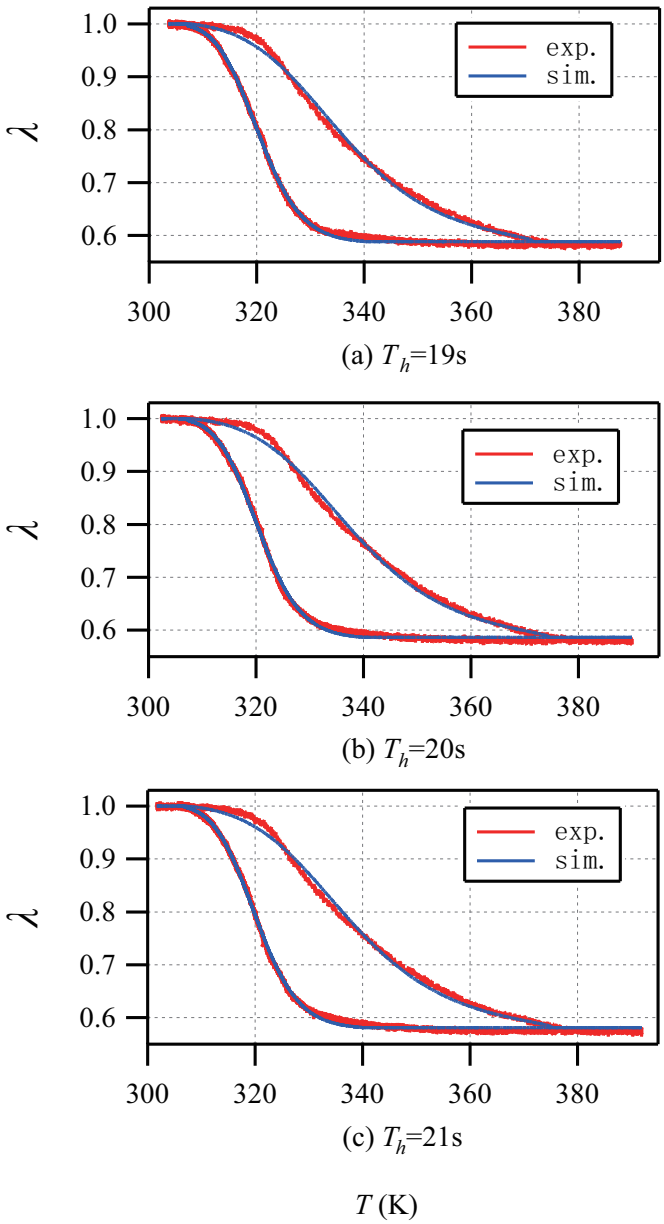

Figure 5.4: Experimental results for $T_h = 19, 20, 21$ s

Fig. 5.6 is provided to give the enlarged plot of the area marked by the green dashed line in Fig. 5.5. This enlarged graph shows that for a certain given T, the proposed model fits much better when compared with model in Chapter 4. To give a quantitative comparison, Table 5.2 provides the RMSEs of the two models for $Amp = 0.4$ mA, $T_h = 16, 17, 18, 19, 20, 21$ s.

The results show that the proposed work in this paper has a better performance when it is compared with a model which does not consider the dynamic process of the phase transition of LCE molecules.

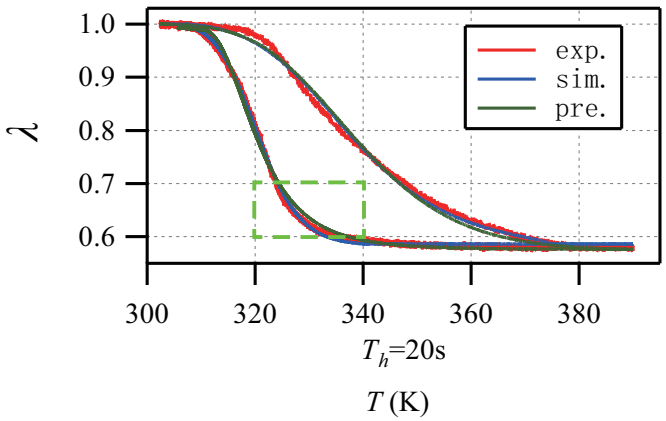

Figure 5.5: A comparison with the model in Chapter 4

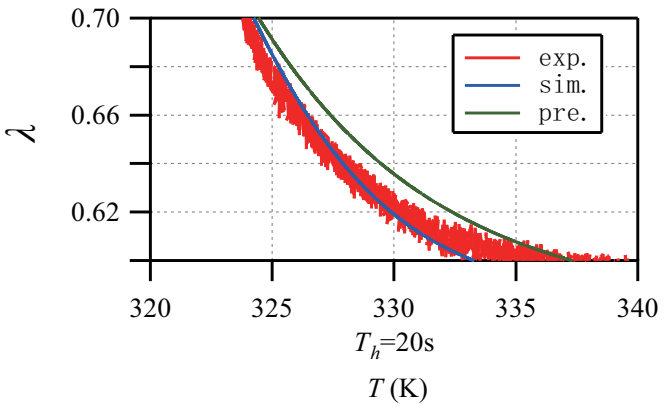

Figure 5.6: An enlarged plot of Figure 5.5

5.5 Concluding Remarks

As has mentioned, hysteresis is the most important feature of LCE's nonlinearity. Thus, to precisely describe the deformation of the photo-responsive LCE actuator, the key point is

Table 5.2: Performance comparison with previous models

T_h	16	17	18	19	20	21
RMSE ($\times 10^{-3}\%$)	6.0	5.4	5.3	5.4	5.6	5.6
RMSE (pre.) ($\times 10^{-3}\%$)	7.4	7.1	9.3	8.4	9.0	9.3

to give a thorough description of its hysteretic behavior. Although the model presented in Chapter 4 can describe the deformation characteristics of LCE with good accuracy, its lack of description on the dynamic process of the phase transition of LCE molecules would still bring inaccuracy. Thus, to solve this problem, this chapter improves the model presented in Chapter 4 by considering the dynamic process of the phase transition. Moreover, a two-step parameter identification strategy adopting the DE algorithm and nonlinear least squares method is provided to identify the unknown model parameters based on experimental data with fast convergence and high accuracy. The experimental results show that the proposed model can describe the hysteresis of LCE with a higher precision, and can provide an effective way in describing LCE's deformation behavior.

Chapter 6

Positioning Control of LCE Actuator Based on Double Closed-Loop System Structure

In this Chapter, based on the deformation mechanism introduced in Chapter 3, positioning control of the photo-responsive LCE actuator is discussed from the energy perspective, and a double closed-loop feedback structure with a feed-forward controller to realize the positioning control of the photo-responsive LCE actuator is designed. Here, the positioning control target is to make the LCE actuator reach a certain target displacement d_d, so the displacement d of the LCE actuator (Figure 3.4) is used to represent the deformation instead of the deformation coefficient λ.

Based on this control scheme, specific controllers are designed to realize the positioning control of the photo-responsive LCE actuator in real experiments. Firstly, filters in the inner and outer loop feedback channels are designed to deal with the measurement noises. Then, designs for the inner loop controller, the feed-forward controller, and the the outer loop controller are presented, respectively. During controller design, the basic physical model established in Chapter 4 is used for the hysteretic part of the system, based on which an inverse

model is built to compensate the hysteresis in the system. Meanwhile, rest of the system which does not involve hysteresis is modeled using based on the Hammerstein-Wiener model, which will be utilized for the parameter tuning of the inner loop controller. Experiments are performed to show the validity of the proposed strategy.

6.1 Positioning Control Scheme for LCE Actuator

With the purpose of developing soft robot applications based on photo-responsive LCE actuator, precise positioning control is a very important topic. As mentioned in Chapter 2, to deal with system with hysteresis, we can either use inverse compensation to construct a feed-forward controller to compensate the hysteretic nonlinearities [119]. Or we can use direct methods to mitigate hysteresis without having to construct its inverse model [120]. These works provide basic strategies that can be utilized in positioning control for systems with hysteresis.

Based on the above two strategies, [100] gave a combined strategy for the control of the electro-driven piezoelectric actuator. In this work, the inverse compensation is combined with a feedback control strategy to ensure that the precise control target can be achieved. This is a control strategy with a single loop control structure for the control of conventional electro-driven smart materials, the availability of the models for the electro-driven piezoelectric actuator makes the controller design possible. However, since the deformation mechanism of the photo-responsive LCE actuator differs greatly from that of the conventional electro-driven smart materials, we need to utilize presented model in previous chapters to aid the design of the positioning control strategy for the photo-responsive LCE actuator.

The difference between conventional electro-driven smart materials and the photo-responsive LCE can be explained based on the deformation mechanism of the LCE actuator. For conventional electro-driven smart materials, the electrical input directly controls the shape of the actuator. However, for photo-responsive LCE, its deformation is directly influenced by its temperature, which is rather an intermediate variable in the deformation process, but

not the direct input of the system. It is clear that the deformation of the LCE actuator is a multi-step process different from conventional electro-driven smart materials.

To deal with this multi-step deformation process, a possible strategy to achieve the positioning control of the LCE actuator is the utilization of the double closed-loop feedback structure. This structure controls both the temperature and the deformation of LCE simultaneously and uses them as feedback signals for inner and outer loop controllers to achieve the overall positioning control of the LCE's actuator. Using this structure can effectively utilize the unique deformation mechanism of LCE to mitigate controlling errors more effectively and accurately than using the conventional single closed-loop control structure.

6.1.1 Positioning Control of LCE Actuator

Figure 3.2 can be used to describe the positioning control of the photo-responsive LCE actuator. Here, the input is a command signal which decides the power efficiency P of the laser, whose value is related to the desired target displacement d_d. P brings variation to the temperature T of the LCE actuator, which then influence the output of the system, which is the measured displacement d. Here we use d instead of λ to describe the deformation of the LCE actuator since it is a parameter that can be directly measured. Meanwhile, it should be noted that, although the modeling of the photo-responsive LCE actuator only needs to consider the thermal-induced phase change in Figure 4.1. For the positioning control of the LCE actuator, the whole process including the light stimulation as well as the light-induced temperature change should still be taken into consideration.

From the energy point of view, we can further analyze the deformation process of LCE with more details. This is given as Figure 6.1. The control signal v carries electrical energy, which converts to the optical energy in the laser. Then, under light stimulation, the LCE actuator receives the optical energy, which converts to its thermal energy that can be evaluated by the temperature T of the LCE actuator. The above energy conversion processes are rather simple and straightforward. When the temperature of the LCE actuator raises due to

light stimulation, the arrangement of LCE molecules will change from aligning to a certain direction to random alignments, this difference in alignments will result in a macroscopic shape change. In this process, the deformation of LCE is dependant on LCE's current state, this dependency leads to the hysteretic characteristic. So this is the process in which the hysteresis takes part.

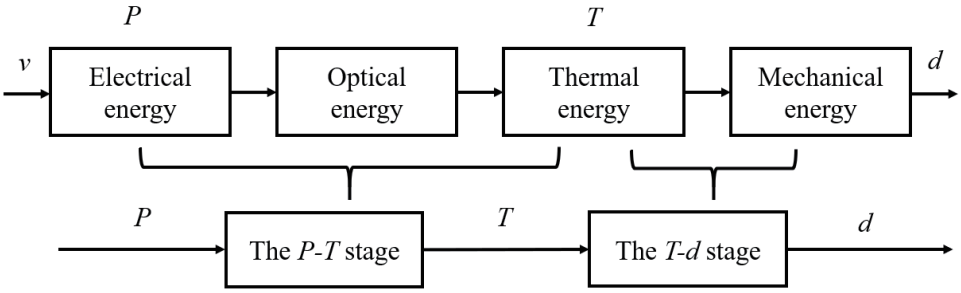

Figure 6.1: The energy conversion in the LCE actuator

Based on the above discussions, the deformation of the LCE actuator can be separated into two stages based on the complicity of each stage, this is also shown in Figure 6.1. For the first stage, the input is the control signal, which sets the power efficiency P of the programmable laser, and the output is the temperature T of the LCE actuator, so we call it the P-T stage. The P-T stage includes the transition from the electrical energy to the optical energy, and the transition from the optical energy to the thermal energy. In this stage, the P-T relationship does not involve hysteresis, and can be modeled either with a physical heating model or with a mathematical model. This model will be used to aid the tuning of controller parameters, and will be discussed in later sections.

As for the second stage, the input is the temperature T of the LCE actuator, and the output is the displacement d, so we call it the T-d stage. This stage is highly nonlinear, and is where hysteresis takes part. Modeling of this part has been introduced in the previous two chapters, and this model will be used to develop an inverse model as a feed-forward controller to compensate the hysteresis in the system. The output of the first stage is the input of the second stage, so these two stages are connected in series, which is also shown in Figure 6.1.

6.1.2 Double Closed-loop Control Structure

Based on discussions from the previous subsection, the deformation of LCE is a multi-step process that can be considered as two stages in series: the P-T stage and the T-d stage. For the P-T stage, we can establish a P-T model to give the relationship between P and T. Similarly, for the T-d stage, we can establish a T-d model to give the relationship between T and d. These two models are established separately, and their respective outputs T and d are both measurable. The complicity of the multi-step deformation process will significantly increase the positioning control difficulties due to certain modeling errors and disturbances that happen in each stage. To overcome these difficulties, we develop a double closed-loop feedback control structure with a feed-forward controller to achieve the positioning control of the photo-responsive LCE actuator, as shown in Figure 6.2, in which the temperature T is the inner loop feedback signal, and the displacement d is the outer loop feedback signal.

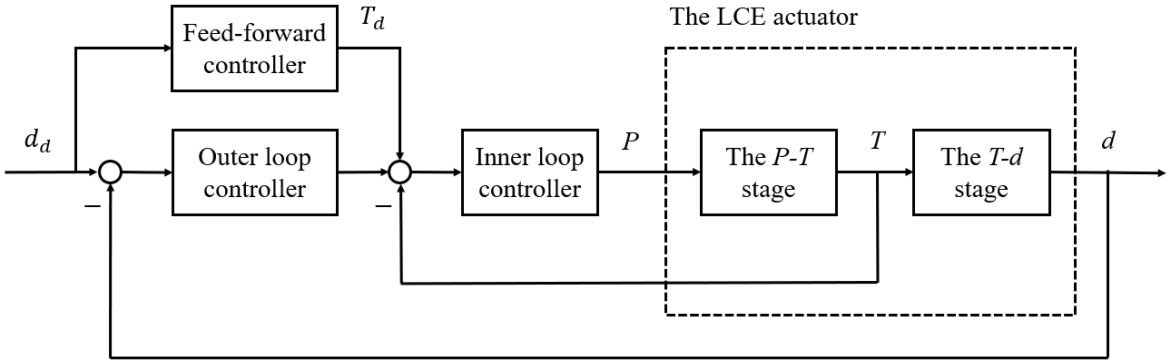

Figure 6.2: Double closed-loop structure for the positioning control of the LCE actuator

In Figure 6.2, the outer loop controller is utilized to ensure that the LCE actuator reaches the positioning control target. Meanwhile, the outer loop controller is in parallel with a feed-forward controller, which is an inverse model of the T-d model that works to compensate the hysteresis of the LCE actuator. Based on the inverse model, the feed-forward controller calculates the temperature value T_d corresponding to the positioning control target d_d. This T_d is then set as the target temperature of the LCE actuator. Then, the difference between

the target temperature T_d and the measured temperature T, adding to the output of the outer loop controller as a compensation value, gives the input of the inner loop controller. Based on this input value, the inner loop controller works to make sure that the temperature T of the LCE actuator reaches its target value T_d with fast response and high efficiency.

This proposed structure controls the temperature of the LCE actuator as well as its deformation simultaneously, which allows the LCE actuator to reach its control target with high precision and speed. In the following sections, this control scheme will be utilized as a basis to develop controllers to realize the positioning control of the photo-responsive LCE actuator.

6.2 Design of Filters

In the positioning control, the measuring data of the laser sensor and thermal camera have measurement noises. To eliminate these noises, two filters are designed to improve the quality of the measured data and to overcome the influences of the measurement noises on the position control of the LCE actuator. By analyzing the measured data, we have noticed that the measurement noises of the laser displacement sensor and thermal camera are mainly high frequency noises. Therefore, we design two low pass filters to process the measured data.

Selectable low pass filter frames are various, eg. the Butterworth filter frame [121], Chebyshev filter frame [122], etc.. Here, we design the low pass filter for the inner and outer loop feedback channel to simplify the design and facilitate the implementation in engineering, which can be given as:

$$F_p(s) = \frac{K_f}{T_f s + 1} \tag{6.1}$$

in which s represents the Laplace operator. K_f is the gain of the filter. T_f is the time constant.

Here, K_f and T_f will be tuned through practical experiments. Meanwhile, we use same values for both filters, which ensures both simplicity and filtering effectiveness. Based on

tuning, the values are $K_f = 1$ and $T_f = 0.1$. The filtering results are shown in Figure 6.3, in which the solid blue line represents the original measured data, and the red dotted line represents the filtered signal. It is shown that the high frequency noises in the measured data of the laser displacement sensor and thermal camera are filtered out effectively, this shows that the performances of the filters with tuned values are suitable for use.

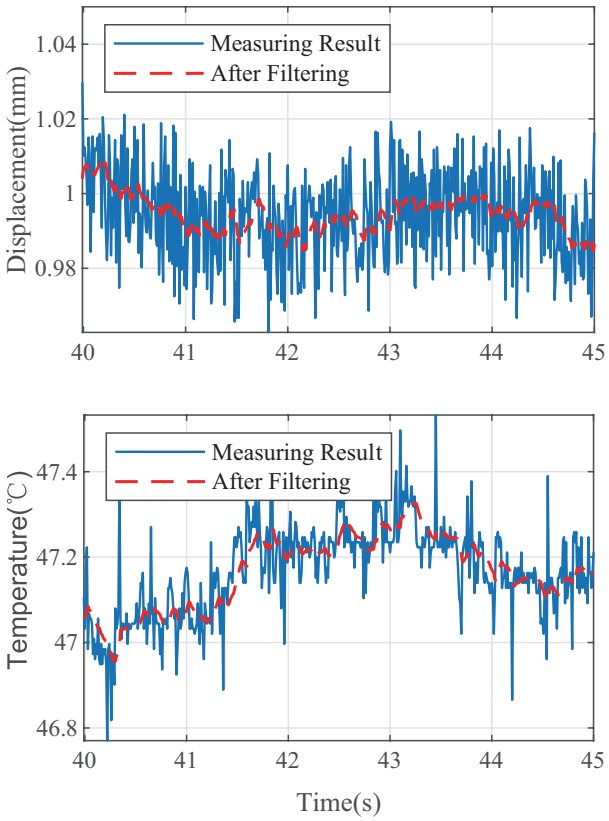

Figure 6.3: Filtering results

6.3 Design of Inner Loop Controller

The inner loop controller is an error feedback controller. This controller generates a control signal to set the power efficiency P of the programmable laser based on the difference between the target temperature and the actual temperature of the LCE actuator, as well as the compensation signal from the outer loop controller. The goal of the inner loop is to control

the temperature of the LCE actuator to reach the target temperature.

Existing error feedback controllers that can be used in this situation are various, eg. the sliding mode controller [123], fuzzy controller [124], PID controller [125], neural network controller [126], etc.. Among them, the PID controller is a widely-used error feedback controller with the advantages of simplicity, strong robustness and high efficiency. Thus, we design a PID controller as the inner loop controller. Considering that it is difficult to obtain the differential of the signal and the differential result often contains noises, a filter should be added when obtaining the differential of the signal. The formula of the inner loop controller is as follows

$$C_{in}(s) = K_p^{in} + K_i^{in}\frac{1}{s} + K_d^{in}\frac{N_{in}}{1 + N_{in}\frac{1}{s}} \tag{6.2}$$

in which K_p^{in}, K_i^{in} and K_d^{in} are the proportion coefficient, integration coefficient and differential coefficient of the inner loop controller, respectively. N_{in} is a filter coefficient used in solving the differential of the error.

Considering that these parameters have a great influence on the control performance, it is significate to propose an effective parameter tuning method to determine their values. Parameter tuning methods include the experimental tuning method, simulation tuning method and simulation-experiment combined tuning method. Here, the simulation-experiment combined tuning method combines the advantages of both the experimental tuning method and the simulation tuning method to provide a superior parameter tuning strategy [127]. For this method, we first build the mathematical model of the controlled plant. Then, the parameters of the controller are tuned based on the established mathematical model by simulation. Finally, based on the tuning result under the simulation environment, the parameters of the controller are re-tuned in the practical experiment.

To tune the parameters of the inner loop controller by simulation, a model describing the relationship between the controlled power and the temperature of the LCE actuator should be built. This P-T model corresponds to the P-T stage of the deformation of the LCE actuator, as shown in Figure 6.1, and can be either based on a physical heating model, or a mathematical model. Since this part of the system is not related to hysteresis, and its

model is only used for rough parameter tuning, we use a mathematical model for calculation simplicity.

Mathematical models for nonlinear systems are various, including the Volterra model [128], the nonlinear autoregressive with exogenous terms model [129], the Hammerstein-Wiener (HW) model [130], etc.. Among them, the HW model has the advantage of flexibility and generalization, and we use the HW model to describe the P-T stage. It should be noted that for the P-T model, any of these models would work, and the main focus is the utilization of the P-T model for parameter tuning, so there we simply select HW model as a demonstration of this idea.

The HW model (see Figure 6.4) is constructed by connecting a static input nonlinear system $\varphi(\cdot)$, a dynamic linear system G and a static output nonlinear system in series $\psi(\cdot)$. The forms of the static input nonlinear system and static output nonlinear system can be specified as the piecewise-linear function, sigmoid network, saturation, dead zone, one-dimensional polynomial, etc.. In these forms, the piecewise-linear function has a simple representation and can approximate the nonlinear characteristics accurately. Therefore, both input nonlinear system $\varphi(\cdot)$ and output nonlinear system $\psi(\cdot)$ are specified as the piecewise-linear functions, which are defined as

$$\varphi(p) = \frac{p - p_l}{p_{l+1} - p_l}(x_{l+1} - x_l) + x_l, \quad p \in [p_l, p_{l+1}] \tag{6.3}$$

$$\psi(w) = \frac{w - w_s}{w_{s+1} - w_s}(T_{s+1} - T_s) + T_s, \quad w \in [w_s, w_{s+1}] \tag{6.4}$$

in which $l = 1, 2, \ldots, l_m$, $s = 1, 2, \ldots, s_m$, $p_1 \leq p_l < p_{l+1} \leq p_{l_m}$, $w_1 \leq w_s < w_{s+1} \leq w_{s_m}$, (p_l, x_l) and (w_s, T_s) represent the break points of (6.3) and (6.4), respectively, and l_m, s_m are the numbers of the piecewise-linear functions in $\varphi(\cdot)$ and $\phi(\cdot)$ respectively.

The linear system G is defined as

$$G\left(z^{-1}\right) = \frac{B\left(z^{-1}\right)}{F\left(z^{-1}\right)} z^{-n_k} \tag{6.5}$$

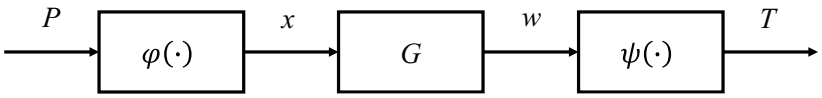

Figure 6.4: HW model framework for P-T stage

$$\begin{cases} B\left(z^{-1}\right) = b_1 z^{-1} + \cdots + b_m z^{-m} \\ F\left(z^{-1}\right) = 1 + p_1 z^{-1} + \cdots + p_n z^{-n} \end{cases} \tag{6.6}$$

in which z^{-1} represents the delay operator. n_k represents the input delay. m and n are the orders of $B\left(z^{-1}\right)$ and $F\left(z^{-1}\right)$, respectively. $b_1, \ldots, b_m$ and $p_1, \ldots, p_n$ are the coefficients of $B\left(z^{-1}\right)$ and $F\left(z^{-1}\right)$.

To identify the parameters in the HW model, experiments using inputs with different power efficiency P are executed in advance. P can be given by equation (4.20). By setting different values for Amp and T_h, different power efficiency P can be generated.

It should be noted that the modeling gets more accurate with the increasing of l_m, s_m, m, n and n_k. However, the computation load will increase as well. In order to make a trade-off between the modeling accuracy and the computation load, $l_m = s_m = 25$, $m = 2$, $n = 3$ and $n_k = 1$ are selected in this paper. According to the experimental results, the undetermined parameters in the HW model are identified by using the iterative estimation scheme based on the nonlinear least squares algorithm [131]. As a result, the breakpoints of the piecewise-linear functions are listed in Table 6.1, and G is given by

$$G\left(z^{-1}\right) = \frac{z^{-1} - 0.999z^{-1}}{1 - 2.991z^{-1} + 2.981z^{-2} - 0.991z^{-3}} z^{-1} \tag{6.7}$$

In experiments, different T_h is used to obtain different power efficiency P. Figure 6.5 shows the comparisons of the model predictions and experimental results with different controlled powers. The subplots (a), (b), (c) and (d) correspond to the situations $T_h = 9$ s, $T_h = 13$ s, $T_h = 17$ s and $T_h = 21$ s, respectively. Moreover, the modelling error of each test validation,

Table 6.1: Breakpoints of piecewise-linear functions

l	(p_l, x_l)	s	(w_s, D_s)
1	$(0.0693, 1.9241)$	1	$(-1.3448 \times 10^5, -232.7717)$
2	$(0.1384, 7.5642)$	2	$(-1.2279 \times 10^5, -215.2135)$
3	$(0.2077, 8.1902)$	3	$(-1.1110 \times 10^5, -195.1194)$
4	$(0.2769, 10.8081)$	4	$(-9.9416 \times 10^5, -172.1058)$
5	$(0.3462, 12.7843)$	5	$(-8.7727 \times 10^4, -146.5579)$
6	$(0.4154, 16.6276)$	6	$(-7.6039 \times 10^4, -118.5106)$
7	$(0.4845, 23.5522)$	7	$(-6.4350 \times 10^4, -89.8077)$
8	$(0.5538, 14.6329)$	8	$(-5.2662 \times 10^4, -54.2228)$
9	$(0.6231, 1.9441)$	9	$(-4.0973 \times 10^4, -36.1348)$
10	$(0.6924, -14.6967)$	10	$(-2.9285 \times 10^4, 2.3216)$
11	$(0.7616, -23.0358)$	11	$(-1.7596 \times 10^4, 12.5146)$
12	$(0.8308, -28.7578))$	12	$(-5.9077 \times 10^3, 24.3506)$
13	$(0.9001, -29.6911))$	12	$(5.7808 \times 10^3, 33.4893)$
14	$(0.9692, -16.8626)$	14	$(1.7469 \times 10^4, 41.9934)$
15	$(1.0385, -9.7461)$	14	$(2.9158 \times 10^4, 49.3548)$
16	$(1.1078, -2.5223)$	16	$(4.0846 \times 10^4, 55.6388)$
17	$(1.1768, 17.0742)$	17	$(5.2535 \times 10^4, 62.9257)$
18	$(1.2461, 18.2290)$	18	$(6.4223 \times 10^4, 69.2049)$
19	$(1.1353, 12.8986)$	19	$(7.5912 \times 10^4, 75.4492)$
20	$(1.3847, -0.4028)$	20	$(8.7600 \times 10^4, 81.7395)$
21	$(1.4538, 0.5624)$	21	$(9.9289 \times 10^4, 88.0169)$
22	$(1.4999, -0.0237)$	22	$(1.1095 \times 10^5, 87.6377)$
23	$(1.6681, 0.4621)$	23	$(1.2267 \times 10^5, 52.5084)$
24	$(1.8014, 1.1874)$	24	$(1.3435 \times 10^5, 23.7485)$
25	$(1.8192, 1.2210)$	25	$(1.4604 \times 10^5, -2.0808)$

which is the mean of the absolute value of the error, is 0.330, 0.280, 0.412 and 0.518 respectively. It can be seen that the model predictions match the experimental results very well. So, it can be concluded that the established HWW model is effective, and can be used to tune the parameters of the inner loop controller in the simulation environment.

The steps of parameter tuning are as follows. First, we set the expected performance of the inner loop control system. That is, the expected values of the rise time corresponding to a certain rise, overshoot, undershoot, settling time and settling of the inner loop control system are given in advance. Then, we use Simulink Design Optimization Tool to tune the parameters of the inner loop controller. By employing the iterative optimization algorithm, we can obtain the optimized values for controller parameters by Simulink.

6.4 Design of Feed-Forward Controller and Outer Loop Controller

The outer loop controller is an error feedback controller in parallel with a feed-forward controller. This feed-forward controller is an inverse model of the T-d model. Here, we use the model presented in Chapter 4 as a basis to give the relationship between the displacement d and the temperature T of the LCE actuator.

Since in this chapter we use the displacement d instead of deformation coefficient λ to represent the deformation of the LCE actuator, we re-write equation (3.1) as follows:

$$d = L_0 (1 - \lambda) \tag{6.8}$$

The relationship between the deformation coefficient λ and the temperature T can be given by equation (4.17). Thus, equations (6.8) and (4.17) together give the relationship between the displacement d and the temperature T, its inverse relationship can then be obtained numerically. To obtain the inverse model, we calculate the relationship between T and d based on (6.8) and (4.17) for command signals in a certain range to obtain a

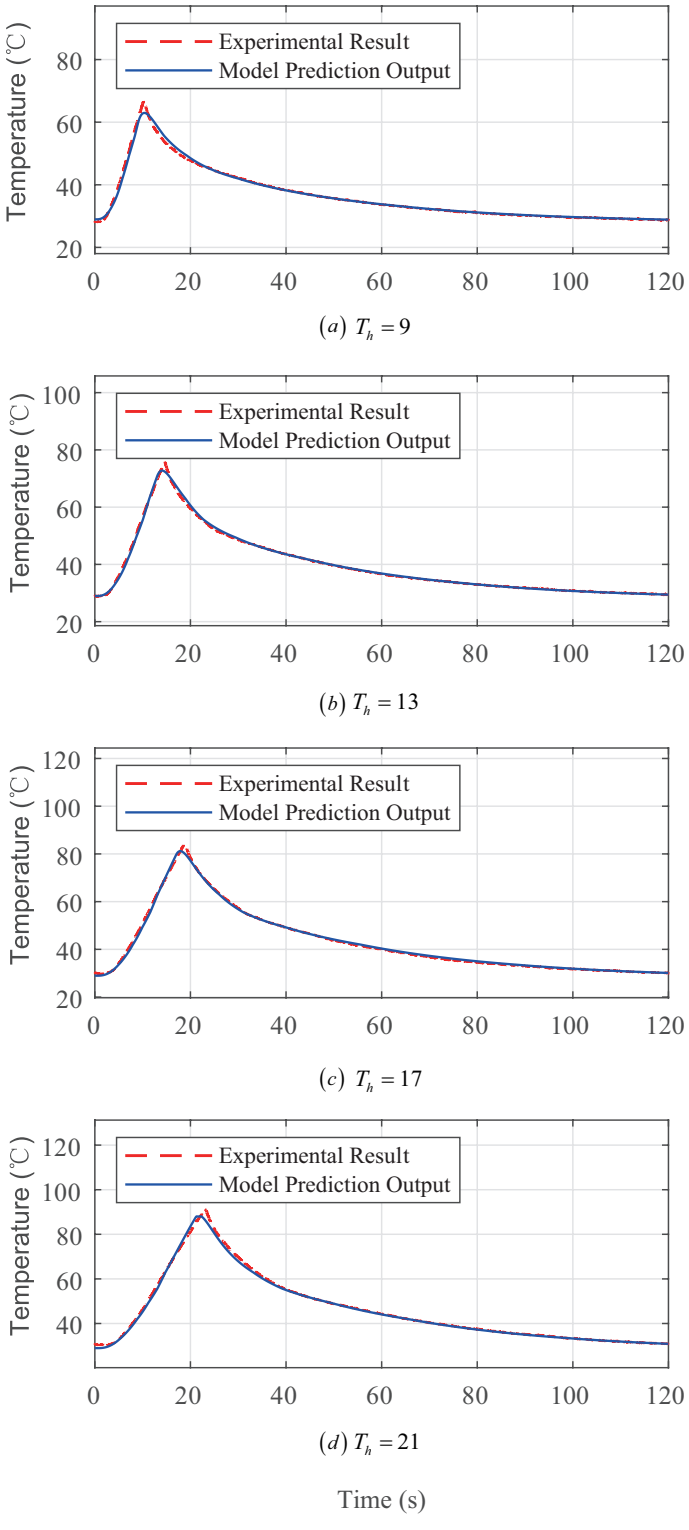

Figure 6.5: Comparisons of model prediction outputs and experimental results

numerical chart. Then, for a selected positioning control target d_d, we look up the range of the corresponding temperature in the chart. The middle value of this range is selected as the target value T_d of the temperature.

Similar to the design of the inner loop controller, for the outer loop controller, we also use the PID control strategy. The outer loop controller is given as follows

$$C_{out}(s) = K_p^{out} + K_i^{out}\frac{1}{s} + K_d^{out}\frac{N_{out}}{1 + N_{out}\frac{1}{s}} \tag{6.9}$$

in which K_p^{out}, K_i^{out}, K_d^{out} and N_{out} are the parameters of the outer loop controller.

Since the outer loop controller works in cooperation with the feed-forward controller, the control effectiveness is not very sensitive to the changes of the values of its parameters. Taken this into consideration, parameters of the outer loop controller are directly tuned by using the experimental tuning method. Here, the tuning principles are as follows:

(1) When the overshoot is large, the value of K_p^{out} should be decreased.

(2) When the rise time is long, the value of K_p^{out} should be increased.

(3) When the steady-state error is large, the value of K_i^{out} should be increased.

(4) When there exhibits obvious shake in the curves of experiments, the value of K_d^{out} should be decreased.

6.5 Experimental Realization and Parameter Tuning

In this section, positioning control experiments are carried out. We use the filters, inner and outer loop controllers designed in the last section to perform parameter tuning. We first tune the parameters of the inner loop controller by employing the simulation-experiment combined tuning method, and the outer loop controller as well as the filters by using the experimental tuning method. Then, double closed-loop control experiments with different target positions are performed.

6.5.1 Experimental Setting and Parameter Tuning of Controllers

We perform the positioning control experiments with different target positions for the LCE actuator. Since the deformation of the LCE actuator has a limit, the values of the target position should not exceed this limit. In our experiments, we have tested and found out that this deformation limit for the LCE actuator is 3.0 mm. Thus, we set the following target positions for different sets of experiments: 1.0 mm, 1.5 mm, 2.0 mm, 2.5 mm and 3.0 mm. The goal of the positioning control is to control the movable edge of the LCE actuator to its target position with a fast response and a small steady-state error.

The expected values for parameters that evaluate the performance of the inner loop control system are set as: 5 s rise time for 80% rise, 15% overshoot, 5% undershoot, 16 s settling time and 7% settling. Moreover, due to the limitation of the programmable laser, the output of the inner loop controller should to less than 10 W. The environment temperature is 28 °C.

Values of parameters of the inner loop controller are tuned by employing the iterative optimization algorithm embedded in Simulink Design Optimization Tool of Simulink. The corresponding tuning results of the parameters of the inner loop controller are

$$\begin{cases} K_p^{in} = 0.062, K_i^{in} = 0.022 \\ K_d^{in} = 0.002, N_{in} = 100 \end{cases} \tag{6.10}$$

Due to modeling errors and disturbances, the parameters in (6.10) still need to be re-tuned in order to obtain good positioning control performance in practical experiments. Through repeatedly tuning the values of the parameters of the inner loop controller and implementing the experiment, the parameters of the inner loop controller are finally selected as

$$\begin{cases} K_p^{in} = 0.05, K_i^{in} = 0.01 \\ K_d^{in} = 0.001, N_{in} = 100 \end{cases} \tag{6.11}$$

Meanwhile, parameters of the outer loop controller are directly tuned through practical experiments according to the tuned principles given in previous section. The tuning results

of the outer loop controller are

$$\begin{cases} K_p^{out} = 0.039, K_i^{out} = 0.013 \\ K_d^{out} = 0.002, N_{out} = 100 \end{cases} \tag{6.12}$$

According to the inverse model and the target positions, outputs of the feed-forward controller are calculated, the results are 48.43 °C, 50.22 °C, 53.14 °C, 56.90 °C and 61.29 °C for $d_d = 1.0$ mm, 1.5 mm, 2.0 mm, 2.5 mm and 3.0 mm, respectively. Moreover, considering that the maximum sampling frequency of the programmable laser is 100 Hz, the control period of the practical experiment is set to be 0.01 s to prevent data distortion and to obtain accurate experimental results.

To illustrate the effectiveness of the proposed control structure, we use RMSEs of the experimental results to evaluate the control performance quantitatively. Here, the RMSE of a data set is calculated as follows:

$$\sigma = \frac{1}{N}\sqrt{\sum_{j=1}^{N}(d_d - d_j)^2} \times 100\% \tag{6.13}$$

in which N is the total number of data points, and d_j is the displacement value at the j-th sampling point.

6.5.2 Double Closed-loop Control Experiments

Based on the tuned parameters of controllers and filters, the proposed double closed-loop control structure is employed to achieve the positioning control of the LCE actuator. The control results are shown in Figures 6.6 to 6.10. Subplots (a), (b), (c) and (d) show the actual displacement and target position, the change of the temperature of the LCE actuator, the controlled power of the programmable laser and the percentage of the position control error, respectively. Here, the percentage of the position control error is calculated by dividing the position control error by the target position.

Figures 6.6 to 6.10 show that the positioning control objective of the LCE actuator can be realized based on the double closed-loop control structure for different target positions.

Table 6.2: RMSEs with different control structures

d_d (mm)	σ for double loop (%)	σ for single loop (%)
1.0	1.59	2.52
1.5	1.74	2.31
2.0	2.15	2.76
2.5	1.81	2.18
3.0	1.94	2.55

These figures also show that the temperature of the LCE actuator responds within 10 s to reach the target temperature calculated from the feed-forward controller. Meanwhile, since the high frequency noises in the measuring results of the laser displacement sensor and thermal camera are filtered out, the shakes of the controlled power and the LCE actuator are restrained.

To evaluate the performance of the control, we calculate the RMSE of the positioning control after 30 s. Here, 30 s is the time it takes for the displacement to become relatively stable in experiments with single loop structure. For double closed-loop structure, such a time is much shorter. But for the purpose of comparison with single loop structure, we use 30 s here to calculate RMSEs for all experiments. We also gather the rise time of each experiment. The results are shown in Table 6.2 and 6.3. From these tables, we can see that the maximum value of RMSEs for all experiments is less than 2.15%, and the maximum rise time is less than 5.12 s, this shows the effectiveness of the proposed control structure.

6.5.3 Comparisons with Single Loop Controllers

To demonstrate the advantages of the proposed double closed-loop control structure, we perform positioning control for the LCE actuator using conventional single closed-loop control structure, which is the positioning control method that is mostly adopted to achieve the the positioning control for actuators based on conventional electro-driven smart materials. The

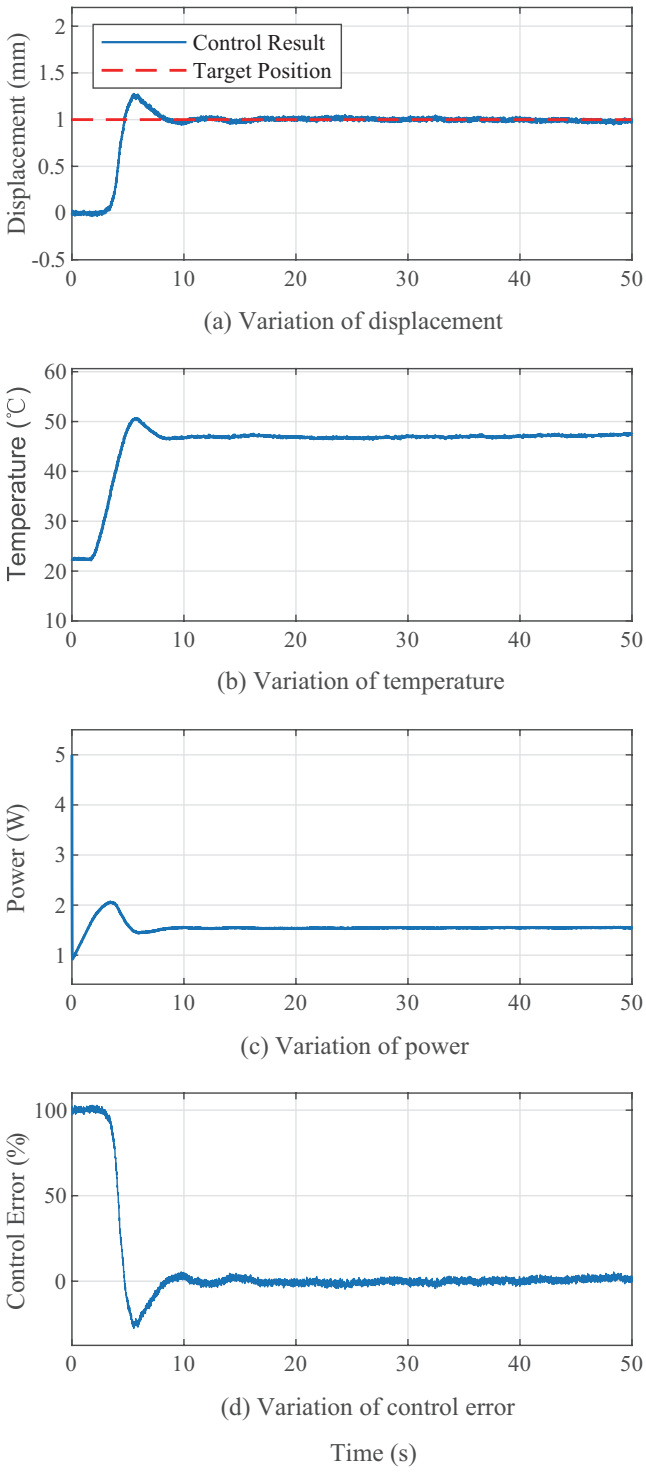

Figure 6.6: Double closed-loop control result with target position 1.0 mm

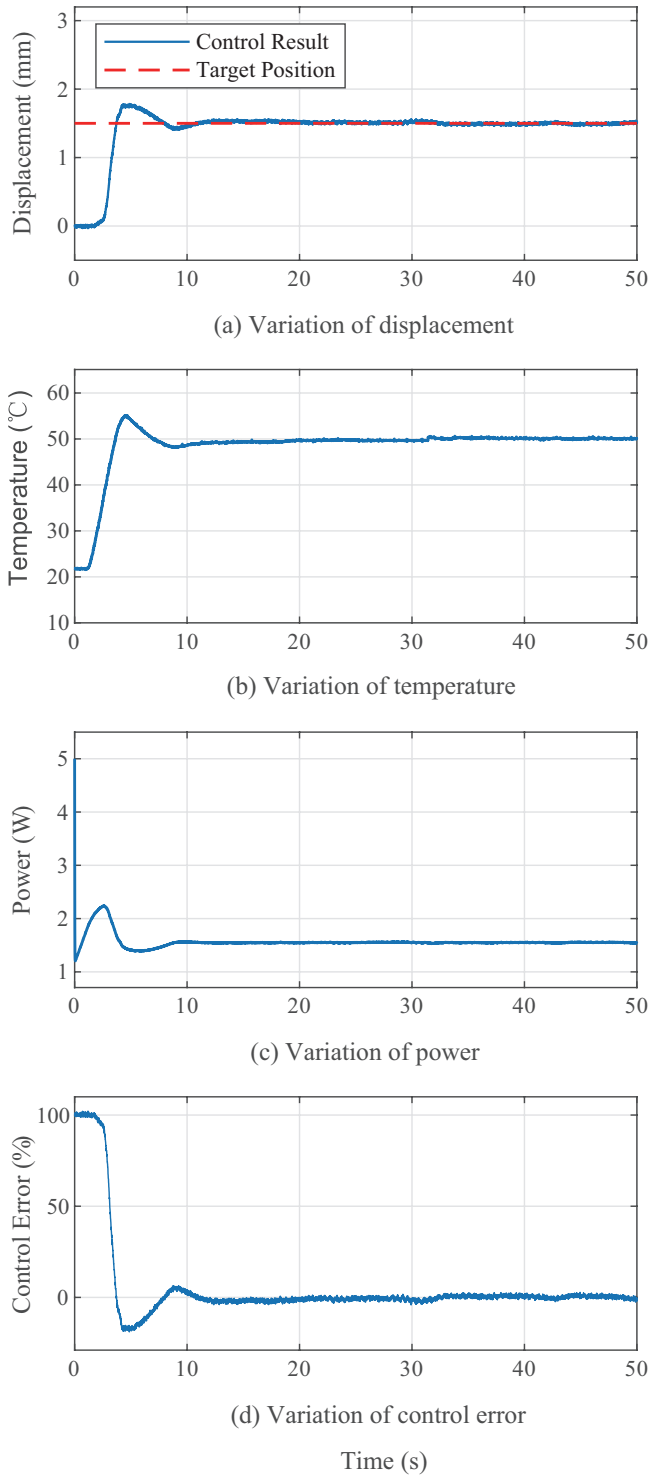

Figure 6.7: Double closed-loop control result with target position 1.5 mm

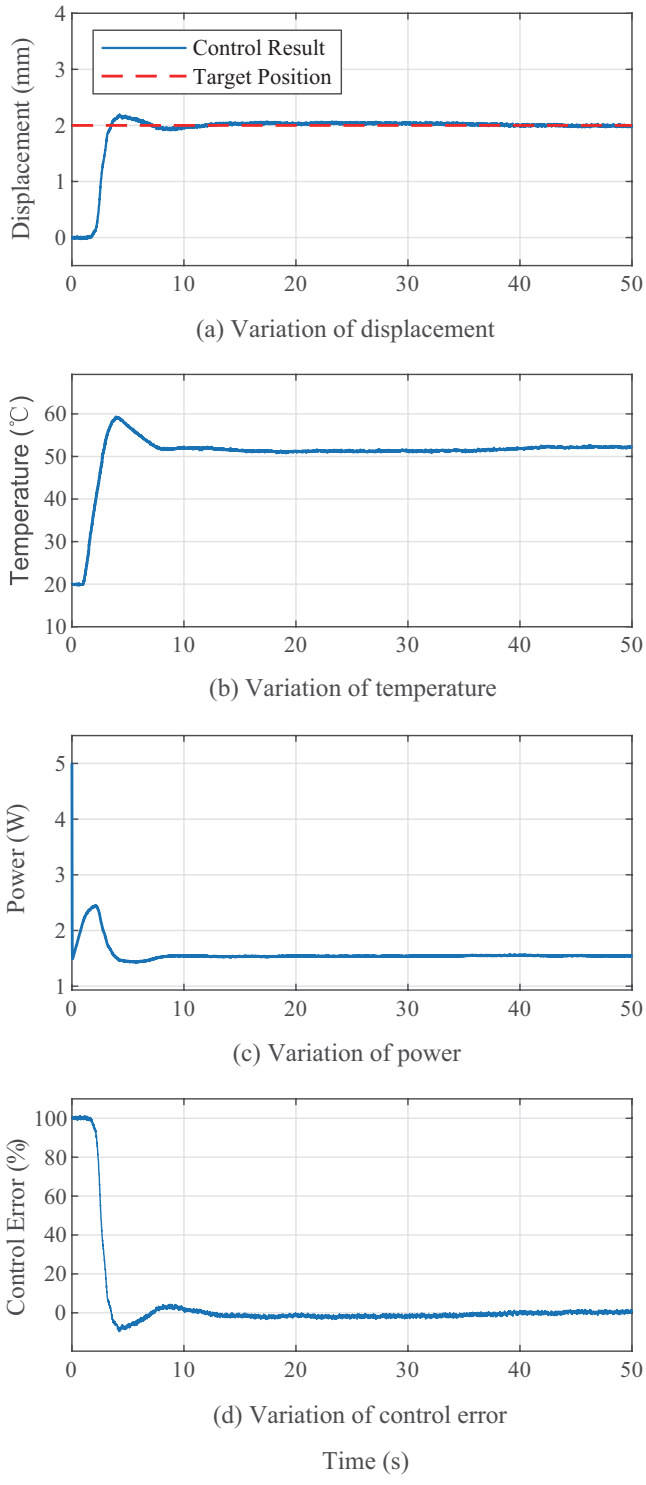

Figure 6.8: Double closed-loop control result with target position 2.0 mm

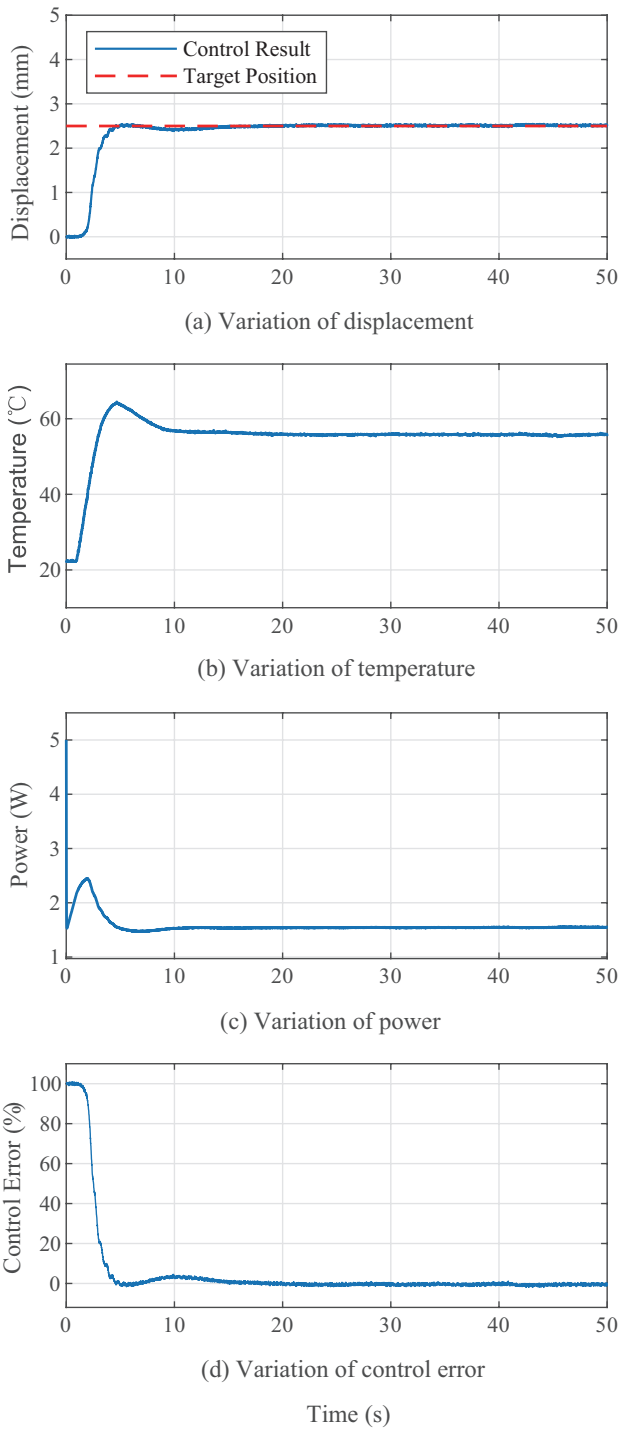

Figure 6.9: Double closed-loop control result with target position 2.5 mm

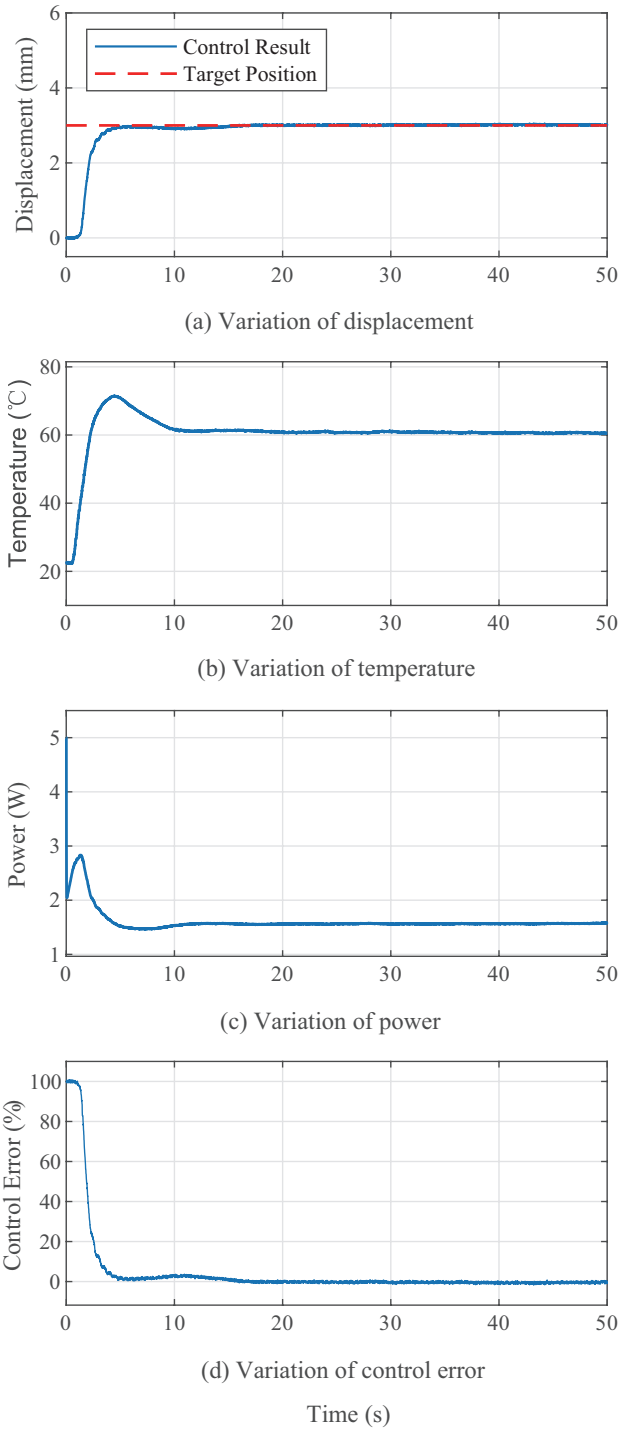

Figure 6.10: Double closed-loop control result with target position 3.0 mm

Table 6.3: Rise times with different control structures

d_d (mm)	Rise time for double loop (s)	Rise time for single loop (s)
1.0	5.12	20.97
1.5	4.23	19.88
2.0	4.15	17.12
2.5	4.87	16.08
3.0	4.96	14.95

control output of the PID controller is directly calculated according to the positioning control error. Comparing with the double closed-loop control structure, the feedback channel for the temperature measurement is ignored in the single loop control structure. Moreover, there is no feed-forward channel based on the inverse model of the LCE actuator. So, the single loop control structure has a model-free structure.

Experiments of single closed-loop control structure with target positions set at 1.0 mm, 1.5 mm, 2.0 mm, 2.5 mm and 3.0 mm are performed. Through repeated tuning the parameters of the PID controller in experiments, a set of optimized parameters is obtained, given as $K_p = 5.837$, $K_i = 0.192$, $K_d = 0.011$ and $N_s = 100$. Figure 6.11 to 6.13 give the examples of the experimental results with target position set to be 1.0 mm, 2.0 mm and 3.0 mm, respectively. These figures show that the positioning control of the photo-responsive LCE actuator can still be realized by employing the single loop control structure. Meanwhile, RMSEs and rise times for all experiments are listed in Table 6.2 and 6.3, in comparisons with results from the proposed double closed-loop control structure. It can be shown from the tables that the proposed double closed-loop control structure has an overall better results than the conventional single closed-loop control structure, specific details are as follows:

(1) In the initial phase of the position control, the temperature of the LCE actuator changes very slowly, so the rise time when using the signal closed-loop control structure is much longer than using the double closed-loop control structure. This is mainly because the

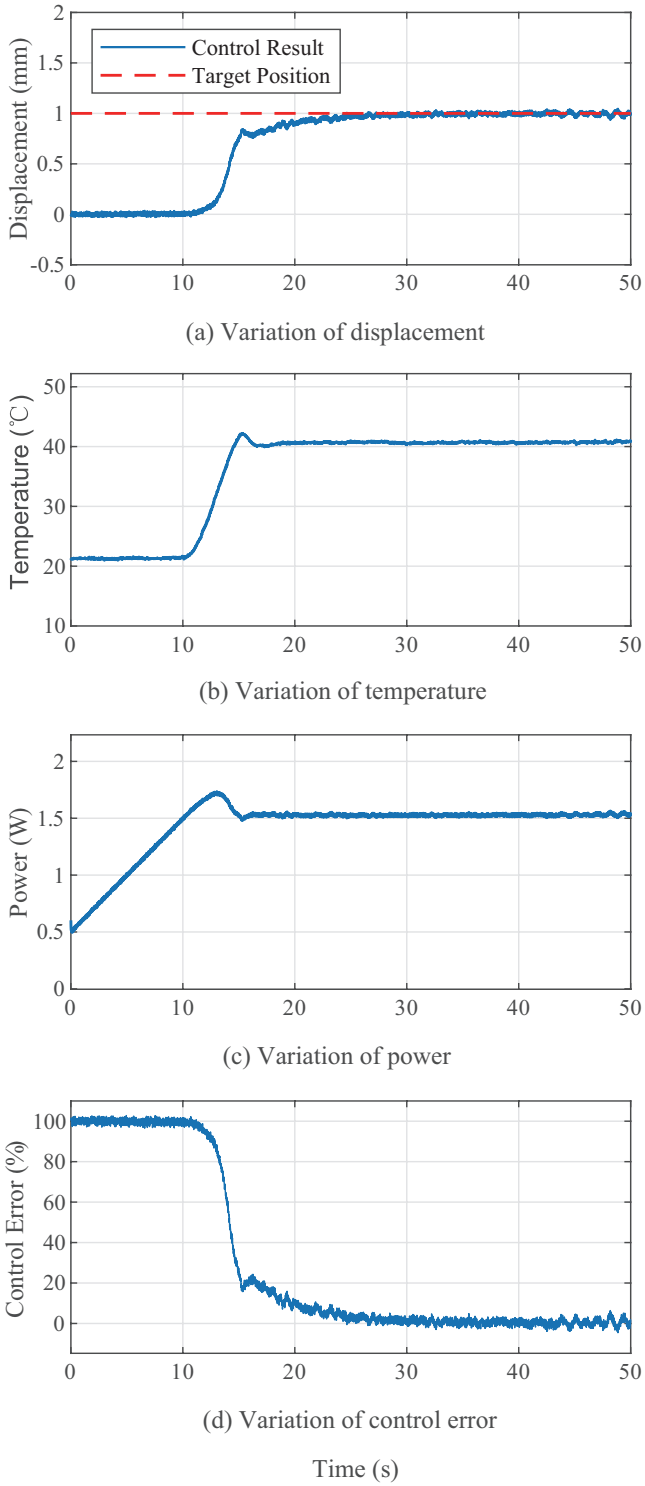

Figure 6.11: Single closed-loop control result with target position 1.0 mm

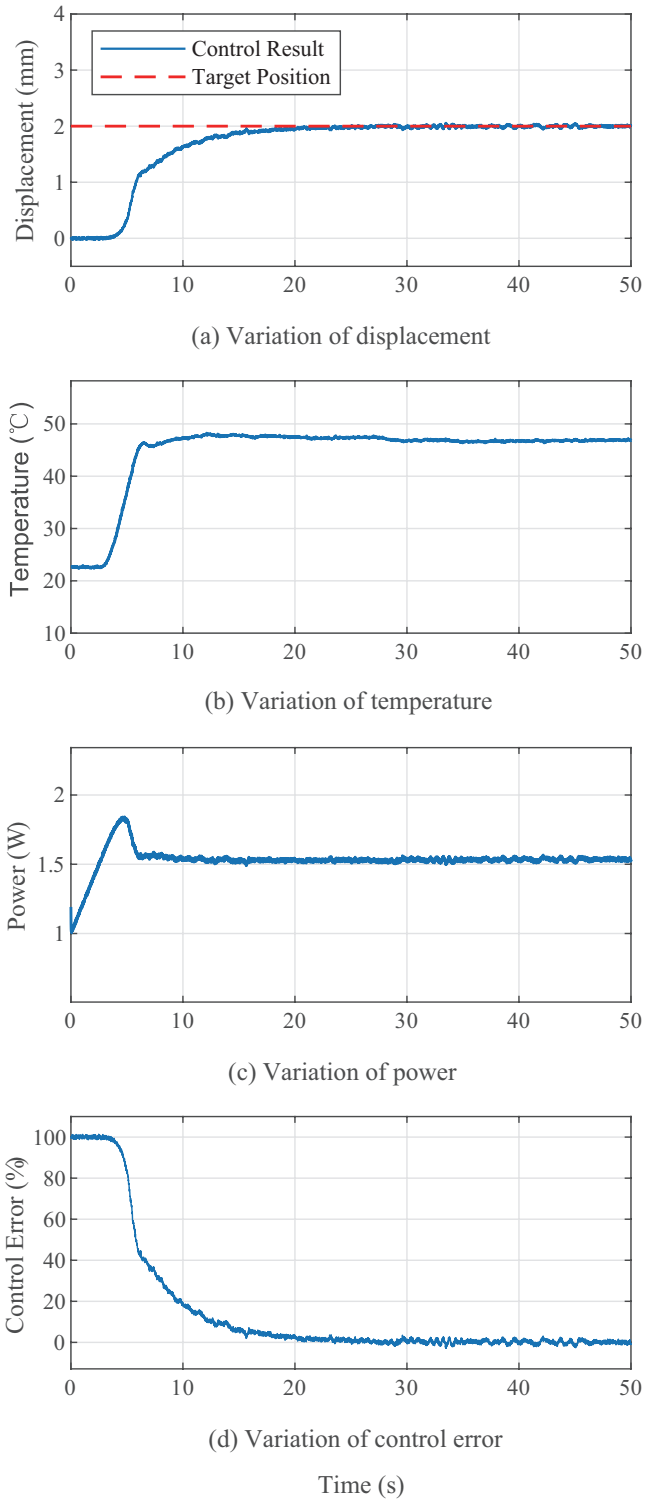

Figure 6.12: Single closed-loop control result with target position 2.0 mm

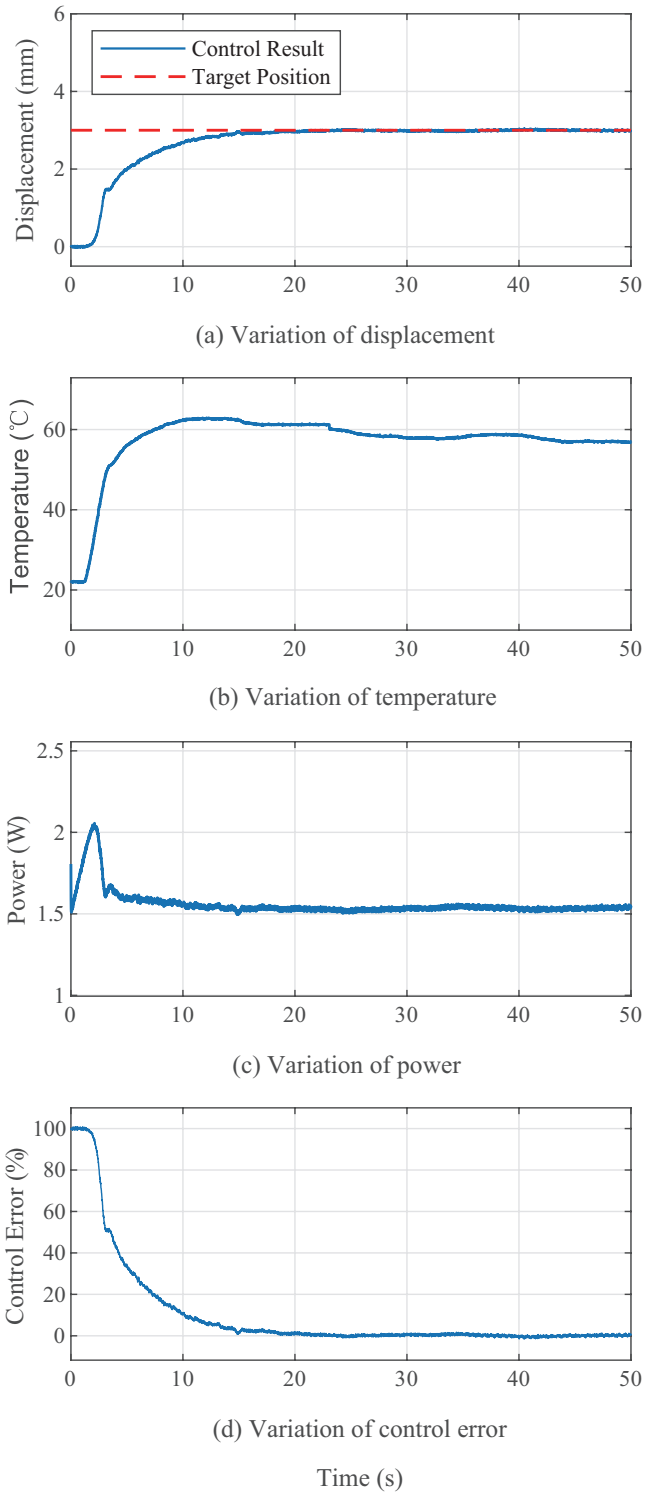

Figure 6.13: Single closed-loop control result with target position 3.0 mm

single closed-loop control strategy does not have the feed-forward channel and the inner loop control.

(2) The RMSEs from the single closed-loop control structure are higher than the results from the double closed-loop control structure, which shows that the proposed double closed loop control structure can achieve control targets with higher accuracy.

To conclude, when compared with the single closed-loop control structure, the double closed-loop control structure can achieve the positioning control target with much faster convergence. Meanwhile, the double closed-loop control structure also has better precision than the single closed-loop control structure.

It should be also noted that for the double closed-loop control structure, we can see that overshoots occur in the displacement and temperature curves, which is a situation that does not occur when we use single closed-loop control structure. This means that there's still room to make the performance of the controller based on the double closed-loop control structure even more superior by eliminating the overshoots in the deformation process. This will be carried out in our future researches.

6.6 Concluding Remarks

In this chapter, a positioning control scheme for the photo-responsive LCE actuator is proposed based on a double closed-loop control structure with a feed-forward controller. For this structure, the inner loop uses a PID controller to control the temperature of the LCE actuator, the parameters of the inner loop controller are tuned using a stimulation-experiment combined method based on the HW model. Meanwhile, the outer loop consists of a PID controller and a feed-forward controller, the feed-forward controller is a numerical inverse model of a physics-based model of the T-d stage, which calculates the target temperature for the inner loop based on the positioning control objective. Parameters of the outer loop controller are directly tuned through experiments. Based on the proposed control strategy,

experiments are carried out with different control target. Compared with conventional single closed-loop control method, the proposed double closed-loop structure is faster in response, and has smaller control errors.

Chapter 7

Discussion on Possible Soft Robot Application Designs Based on LCE actuator

As has been discussed, LCE has unique features which are totally different from conventional eletro-driven smart materials. These features have the potential of leading to design novelty in LCE-based soft robots. In this chapter, we want to discuss the features that we can utilize from LCE's deformation characteristics to come up with a certain guideline for the design of LCE-based soft robot applications. These guidelines should provide a general guidance on LCE-based soft robot design. Then, two specific designs on LCE-based soft robots are introduced as examples of possible applications, their respective working principles are also introduced with details.

7.1 Design Guidelines for LCE-based Soft Robots

It is only natural that the idea of light-induced deformation would lead to the idea of heliotropism, which is a direct inspiration from biological systems which utilizes the solar energy

for its own benefits. [132] is a typical example of this work, in which an artificial heliotropism is designed for solar cells. In this work, the system collects solar energy from the sun and the actuator bend due to light-induced deformation to make the plant lean forward to the direction of the sun. It is indeed inspiring that such light-driven actuators can utilize natural energy sources such as the sunlight. However, it should be noted that collecting solar energy is rather a relatively slow process, which lead to slow response as well.

Besides the energy source, since LCE usually appear as thin films of single or multiple layers. It is only natural to utilized its body softness to mimic biological systems such as caterpillars [133], snails [134], inchworms [135], etc.. Take [133] for example, a single strip of LCE with carefully designed alignment distribution is designed to obtain a caterpillar-like device with certain geometry, such a geometry was enabled by anisotropic thermal expansion that is generated by photopolymerization at elevated temperatures. Under operation, due to the friction difference between the contact surface as well as asymmetric defects created during fabrication, the device succeed in moving towards a certain direction when constantly turning on and off the light stimulation.

Just like [133], there are multiple common points in many LCE-based soft robot applications. One is the utilization of molecule orientation. By setting a specific orientation distribution during the fabrication of the LCE films, certain geometries can be realized to achieve various shapes for different soft robot designs. Another very important consideration is the utilization of asymmetry in design. eg. In [133], the asymmetry of the contact surface leads to the moving pattern of the device. In [1], the LCE polymer was fabricated with a certain asymmetric shape which allows it to swim toward a certain direction when stimulated in water. In [136], the plant is supported by a two-legged structure made of LCE on adhesive PVC tapes, and the bending of the legs under sunlight originates from the difference in length of the two adhered layers.

Another important feature of LCE-based soft robots is the flexibility brought by the chemical features of LCE. A typical example of this feature is the stimulation source. Chemical modification of different methods allow LCE to react to different wavelength such as

green light [1, 134], blue light [137], visible light [132, 133], etc.. This material can even be doped to be responsive under light of different wavelengthes to achieve complicated motions [101]. Such flexibility in design offers promising features for photo-responsive soft robot applications.

7.2 Designs of LCE-based Soft Robots

In this section, a light-controlled two-legged walking robot based on the photo-responsive LCE actuator is established. The schematic of the robot as well as its working principle is shown in Figure 7.1. Figure 7.1(a) depicts the working principle of this robot and Figure 7.1(b) gives the basic structure of each leg. Each leg is consisted of a spring, the outer shell of the leg, and the LCE membrane synthesized into the outer shell, which acts as the actuator that produce the source of locomotion. The contact of left and right legs are design asymmetrically so the friction when moving to the right direction is much smaller than the friction when moving to the left direction. This asymmetry in design can ensure the device to walk towards a certain direction under stimulation.

The walking cycle of the proposed device is given by Figure 7.1a. Under room temperature, both legs are stretched out due to the elasticity of the spring. Then, laser light is produced to scan the right leg, which cause the LCE membrane on that leg to shrink along its length. This shortens the total length of the right leg, due to the friction difference between the two legs, the right leg will drag the left leg to move rightwards. Then, the light stimulation is turned off, the length of the right leg will recover due to the spring. Then, due to the friction difference between the two legs, the right leg will be pushed by the left leg to move rightwards. So, as a result of this whole cycle, the system takes a step to the right, and the walking locomotion is achieved.

Figure 7.2 shows the design of a light-controlled rolling robot. Figure 7.2(a) depicts the locomotion principle and Figure 7.2(b) gives the basic designed structure. The whole robot is has a ring-shaped structure separated into five segments. Normally, the center of mass of the

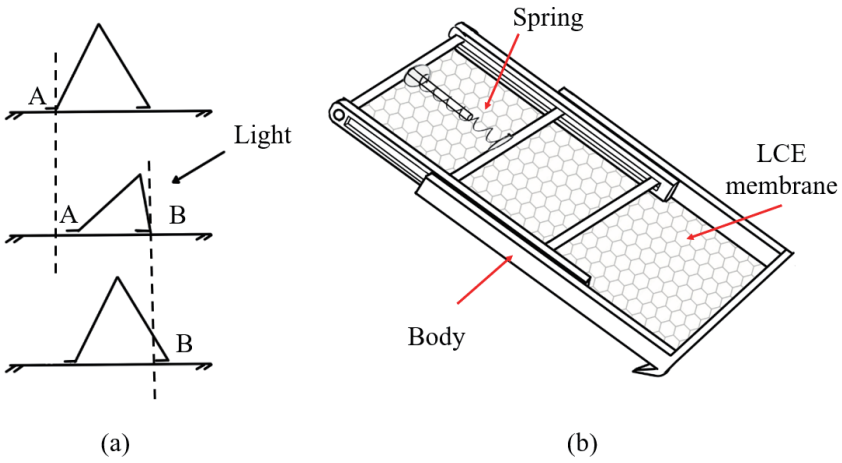

Figure 7.1: Two-legged light controlled LCE walking robot

system is at the center of the circle, when a certain part of the robot is stimulated by light, that segment will deform, which causes the center of mass to move away from the system's center, which produce a torque relative to its geometric center. Such a torque would cause the device to roll toward the direction of the light. If the relative position of the stimulation light and the device is kept constant, the rolling of the device will change the segment that is stimulated by the light, this change will cause further deformation which would keep the device to roll forward.

Design difficulties of these two devices are two-fold. One challenge lies in the integration of the LCE film with the outer shell. It is important to figure out a suitable integration method to make the LCE film work smoothly with the outer shell. Another difficulty lies in the existence of internal frictions, which prevents the device from smoothly working. Since the maximum force that can be produced by a single layer of LCE strip is very limited, it is likely that single-layered LCE actuator is not enough to trigger the desired locomotion. To solve this problem, one possible solution is to chemically adjust the LCE to make it stiffer. Another solution is to stack multiple LCE layers to increase the maximum load of the actuator. These are possible works that can be carried out in the future.

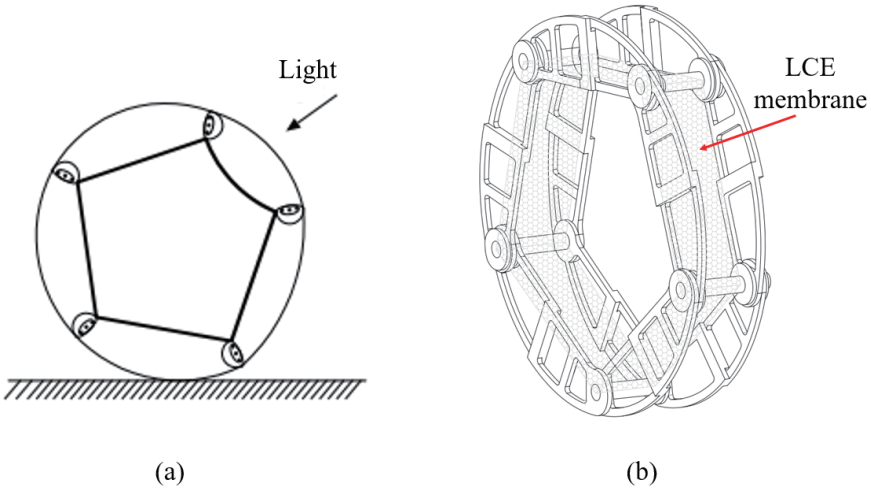

Figure 7.2: Light controlled LCE rolling robot

7.3 Concluding Remarks

Inspired by the unique deformation features of the photo-responsive LCE actuator, the crucial points that can be realized during the design for LCE-based soft robots are discussed, including the utilization of the light source in nature, taking advantage of body softness to mimic biological systems, the utilization of asymmetry in design, the importance of molecule orientation for shape forming, the flexibility in design brought by chemical features, etc.. Then, designs of a light-controlled two-legged walking robot as well as a light-controlled rolling robot are introduced, their working principles are presented and the main challenges in the design are discussed. Based on these presented discussions, possible future works on LCE-based soft robot applications can be carried out.

Chapter 8

Conclusions and Future Work

This chapter provides a brief summary on the works and contributions presented in the dissertation. Possible future works are recommended based on the current works, and related publications are introduced.

8.1 Concluding Remarks

The photo-responsive LCE actuator is a promising candidate to be utilized for possible light-controlled applications. The nature of LCE suggests soft robot applications that are totally different from conventional electro-driven ones. However, since LCE has a complex hysteretic deformation characteristic which is highly dependant on environmental factors, the modeling and control of the LCE actuator is very challenging. This dissertation has made an extensive study on the modeling and control of the photo-responsive LCE actuator to lay a foundation for the development of LCE soft robot applications. The major contributions of the dissertation research are summarized as follows.

(1) Based on the deformation mechanism of the photo-responsive LCE actuator, an experimental platform is established to study the modeling and control of the photo-responsive LCE actuator. This setup uses a computer to send a command signal as the input of the

system. The input controls the power efficiency of the laser light, which stimulates the LCE actuator to heat it up. Based on the multi-step nature of LCE's deformation. The setup not only measures the output displacement, but also the temperature of the LCE actuator as an intermediate variable. This ensures a thorough study and analysis on the deformation of the photo-responsive LCE actuator.

(2) Physical process of the LCE actuator is analyzed to give a basic modeling scheme for the temperature-deformation relationship. In this scheme, the average order parameter is introduced as an intermediate variable to quantitatively represent the phase transition of LCE molecules. Then, the relationship between the temperature and the average order parameter, and the relationship between the average order parameter and LCE's deformation are calculated, respectively. These two relationships combine to give the overall model for the deformation of the LCE actuator.

(3) Based on the proposed modeling scheme, a basic model is developed to give a relatively simple equation for temperature-deformation relationship by assuming that the phase transition of LCE molecules is under dynamic equilibrium. This model also works to reflect the physical nature of the LCE actuator, and can be utilized as a basis for developing more advanced models or control strategies. Model parameters are identified using nonlinear least squares method.

(4) Based on the basic model, an improved model is established by considering the dynamic process of the phase transition of LCE molecules during the deformation process. This improved model gives a complete physical description of LCE's hysteresis, and describe the temperature-deformation relationship with a dynamic equation that reflects the actual physics of LCE's hysteresis. This improved model can describe the deformation of the LCE actuator with high accuracy. Model parameters are identified using a two-step parameter identification strategy based on DE algorithm and nonlinear least squares method with efficiency.

(5) Considering the multi-step nature of the positioning control of the LCE actuator, a positioning control scheme for the photo-responsive LCE actuator is proposed based on

the double closed-loop control structure with a feed-forward controller. This scheme uses the feed-forward controller as an inverse compensation module to compensate for the hysteresis of the LCE actuator. Meanwhile, the double closed-loop control structure controls the temperature and the deformation of the LCE actuator simultaneously to reduce control errors.

(6) Based on the positioning control scheme, controllers are designed for the positioning control of the photo-responsive LCE actuator. Filters are designed to mitigate external noises. The feed-forward controller is designed based on the inverse model of the basic model that is presented in the modeling part. Inner and outer loop controllers are designed as PID controllers to achieve the positioning control target with precision. Parameters are tuned based on an experiment-stimulation combined method. Experimental results show that this presented double closed-loop structure works well and has faster response time and smaller control error than conventional single loop structure.

(7) Designs on LCE based soft robots are discussed. Design guidelines are given to suggest possible ideas on LCE based soft robot design. As a demonstration of the guidelines, designs of a light controlled two-legged walking robot and a rolling robot are presented, difficulties and possible future working directions are discussed.

8.2 Recommendations for Future Works

As the continuation of the studies in this dissertation research, the following research topics in this area can be conducted in the future.

(1) Based on the physics based model, it is desirable to design phenomenological based models to reduce computational burden.

(2) Future studies on the control of photo-responsive LCE actuator can aim to design advanced controllers to perform more complicated control tasks and achieve better control performances.

(3) It is desirable to realize LCE-based soft robot applications utilizing its positioning control. Meanwhile, we want to solve the difficulties in the two-legged walking robot and rolling robot that are presented in Chapter 7.

8.3 Publications

Several papers reporting results of this dissertation research have been published/submitted in journals and well-known international conferences as listed below. These papers were written under the guidance of my supervisor, Dr. C.-Y. Su. Other co-authors of some of the papers contributed partially through extensive discussions with remarkable recommendations, initial simulations, or the combinations of the above.

[1] Wu, J., Ye, W., Wang, Y., & Su, C. Y. (2021). Modeling of Photo-responsive Liquid Crystal Elastomer Actuators. *Information Sciences*, 560, 441-455.

[2] Wu, J., Ye, W., Wang, Y., & Su, C. Y. (2021). A General Position Control Method for Planar Underactuated Manipulators With Second-Order Nonholonomic Constraints. *IEEE Transactions on Cybernetics*, 51 (9), 4733-4742.

[3] Wu, J., She, J., Wang, Y., & Su, C. Y. (2020). Position and Posture Control of Planar Four-Link Underactuated Manipulator Based on Neural Network Model. *IEEE Transactions on Industrial Electronics*, 67(6), 4721-4728.

[4] Wu, J., Wang, Y., Ye, W., & Su, C. Y. (2019). Control strategy based on Fourier transformation and intelligent optimization for planar Pendubot. *Information Sciences*, 491, 279-288.

[5] Wu, J., Ye, W., Wang, Y., & Su, C. Y. Modeling Based on a Two-step Parameter Identification Strategy for Liquid Crystal Elastomer Actuator Considering Dynamic Phase Transition Process. *IEEE Transactions on Cybernetics*, Submitted.

[6] Wu, J., Ye, W., Wang, Y., & Su, C. Y. Positioning Control of Liquid Crystal Elastomer Actuator Based on Double Closed-Loop System Structure. *Control Engineering Practice*,

Submitted.

[7] Wu, J., Wang, Y., & Ye, W. (2019, July). A One-Stage Control Strategy for Planar Underactuated Manipulators. In 2019 IEEE 4th International Conference on Advanced Robotics and Mechatronics (ICARM) (pp. 697-701). IEEE.

[8] Ye, W., Aghili, F., & Wu, J. (2019, July). Adaptive Control of a Class of Nonlinear Systems with Unknown Prandtl-Ishlinskii Hysteresis. In 2019 IEEE 4th International Conference on Advanced Robotics and Mechatronics (ICARM) (pp. 1010-1015). IEEE.

[9] Xiao, H., Wu, J., Ye, W., & Wang, Y. (2020, December). Dynamic Modeling for Dielectric Elastomer Actuators Based on LSTM Deep Neural Network. In 2020 5th International Conference on Advanced Robotics and Mechatronics (ICARM) (pp. 119-124). IEEE.

[10] Huang, P., Wu, J., Ye, W., & Wang, Y. (2020, December). Study of Soft Force and Displacement Sensor Based on Dielectric Elastomer. In 2020 5th International Conference on Advanced Robotics and Mechatronics (ICARM) (pp. 414-418). IEEE.

[11] Xiao, H., Wu, J., Ye, W., & Wang, Y. (2020). Dynamic Modeling of Dielectric Elastomer Actuators Based on Thermodynamic Theory. *Mechanics of Advanced Materials and Structures*, doi: 10.1080/15376494.2020.1829757.

[12] Wang, Y., Wu, J., Ye, W., Huang, P., Ohnishi, K., & Su, C. (2021). Dielectric Elastomer Intelligent Devices for Soft Robots. *Studies in Systems, Decision and Control Series No. 329, Developments in Advanced Control and Intelligent Automation for Complex Systems* (pp. 311-339), Springer.

[13] Huang, P., Wu, J., Zhang, P., Wang, Y., & Su, C. Y. (2021). Dynamic Modeling and Tracking Control for Dielectric Elastomer Actuator with Model Predictive Controller. *IEEE Transactions on Industrial Electronics*, doi: 10.1109/TIE.2021.3063976

Bibliography

[1] M. Camacho-Lopez, H. Finkelmann, P. Palffy-Muhoray, and M. Shelley, "Fast liquid-crystal elastomer swims into the dark," *Nature Materials*, vol. 3, no. 5, pp. 307–310, 2004.

[2] B. Siciliano, O. Khatib, and T. Kröger, *Springer Handbook of Robotics*, vol. 200. Springer, 2008.

[3] J. J. Craig, *Introduction to Robotics: Mechanics and Control, 3/E*. Pearson Education India, 2009.

[4] K. M. Lynch and F. C. Park, *Modern Robotics*. Cambridge University Press, 2017.

[5] T. Hsia, "Adaptive control of robot manipulators-a review," in *Proceedings. 1986 IEEE International Conference on Robotics and Automation*, vol. 3, pp. 183–189, IEEE, 1986.

[6] C. Abdallah, D. M. Dawson, P. Dorato, and M. Jamshidi, "Survey of robust control for rigid robots," *IEEE Control Systems Magazine*, vol. 11, no. 2, pp. 24–30, 1991.

[7] D. Rus and M. T. Tolley, "Design, fabrication and control of soft robots," *Nature*, vol. 521, no. 7553, pp. 467–475, 2015.

[8] A. Bicchi, G. Tonietti, and E. Piaggio, "Design, realization and control of soft robot arms for intrinsically safe interaction with humans," in *Proc. IARP/RAS Workshop on Technical Challenges for Dependable Robots in Human Environments*, pp. 79–87, 2002.

[9] C. Lee, M. Kim, Y. J. Kim, N. Hong, S. Ryu, H. J. Kim, and S. Kim, "Soft robot review," *International Journal of Control, Automation and Systems*, vol. 15, no. 1, pp. 3–15, 2017.

[10] C. Laschi, M. Cianchetti, B. Mazzolai, L. Margheri, M. Follador, and P. Dario, "Soft robot arm inspired by the octopus," *Advanced Robotics*, vol. 26, no. 7, pp. 709–727, 2012.

[11] N. Gariya and P. Kumar, "A review on soft materials utilized for the manufacturing of soft robots," *Materials Today: Proceedings*, 2021.

[12] D. Trivedi, C. D. Rahn, W. M. Kier, and I. D. Walker, "Soft robotics: Biological inspiration, state of the art, and future research," *Applied Bionics and Biomechanics*, vol. 5, no. 3, pp. 99–117, 2008.

[13] C. Lee, M. Kim, Y. J. Kim, N. Hong, S. Ryu, H. J. Kim, and S. Kim, "Soft robot review," *International Journal of Control, Automation and Systems*, vol. 15, no. 1, pp. 3–15, 2017.

[14] T. Li, K. Nakajima, M. Calisti, C. Laschi, and R. Pfeifer, "Octopus-inspired sensorimotor control of a multi-arm soft robot," in *2012 IEEE International Conference on Mechatronics and Automation*, pp. 948–955, IEEE, 2012.

[15] T. TolleyMichael, F. ShepherdRobert, C. GallowayKevin, J. WoodRobert, M. WhitesidesGeorge, *et al.*, "A resilient, untethered soft robot," *Soft Robotics*, 2014.

[16] A. Miriyev, K. Stack, and H. Lipson, "Soft material for soft actuators," *Nature communications*, vol. 8, no. 1, pp. 1–8, 2017.

[17] L. Tiefeng, L. Guorui, L. Yiming, C. Tingyu, Y. Xuxu, and H. Zhilong, "Review of materials and structures in soft robotics," *Chinese Journal of Theoretical and Applied Mechanics*, vol. 48, no. 4, pp. 756–766, 2016.

[18] J. Cao, L. Qin, J. Liu, Q. Ren, C. C. Foo, H. Wang, H. P. Lee, and J. Zhu, "Untethered soft robot capable of stable locomotion using soft electrostatic actuators," *Extreme Mechanics Letters*, vol. 21, pp. 9–16, 2018.

[19] C. Christianson, C. Bayag, G. Li, S. Jadhav, A. Giri, C. Agba, T. Li, and M. T. Tolley, "Jellyfish-inspired soft robot driven by fluid electrode dielectric organic robotic actuators," *Frontiers in Robotics and AI*, vol. 6, p. 126, 2019.

[20] C. Majidi, R. Kramer, and R. Wood, "A non-differential elastomer curvature sensor for softer-than-skin electronics," *Smart Materials and Structures*, vol. 20, no. 10, p. 105017, 2011.

[21] M. Kaltenbrunner, T. Sekitani, J. Reeder, T. Yokota, K. Kuribara, T. Tokuhara, M. Drack, R. Schwödiauer, I. Graz, S. Bauer-Gogonea, *et al.*, "An ultra-lightweight design for imperceptible plastic electronics," *Nature*, vol. 499, no. 7459, p. 458, 2013.

[22] J. A. Rogers, T. Someya, and Y. Huang, "Materials and mechanics for stretchable electronics," *science*, vol. 327, no. 5973, pp. 1603–1607, 2010.

[23] C. D. Onal and D. Rus, "Autonomous undulatory serpentine locomotion utilizing body dynamics of a fluidic soft robot," *Bioinspiration & Biomimetics*, vol. 8, no. 2, p. 026003, 2013.

[24] C. D. Onal, X. Chen, G. M. Whitesides, and D. Rus, "Soft mobile robots with on-board chemical pressure generation," in *Robotics Research*, pp. 525–540, Springer, 2017.

[25] S. Xu, Y. Zhang, J. Cho, J. Lee, X. Huang, L. Jia, J. A. Fan, Y. Su, J. Su, H. Zhang, *et al.*, "Stretchable batteries with self-similar serpentine interconnects and integrated wireless recharging systems," *Nature Communications*, vol. 4, no. 1, pp. 1–8, 2013.

[26] M. Calisti, M. Giorelli, G. Levy, B. Mazzolai, B. Hochner, C. Laschi, and P. Dario, "An octopus-bioinspired solution to movement and manipulation for soft robots," *Bioinspiration & Biomimetics*, vol. 6, no. 3, p. 036002, 2011.

[27] H. Rodrigue, W. Wang, M.-W. Han, T. J. Kim, and S.-H. Ahn, "An overview of shape memory alloy-coupled actuators and robots," *Soft Robotics*, vol. 4, no. 1, pp. 3–15, 2017.

[28] S. Seok, C. D. Onal, K.-J. Cho, R. J. Wood, D. Rus, and S. Kim, "Meshworm: a peristaltic soft robot with antagonistic nickel titanium coil actuators," *IEEE/ASME Transactions on Mechatronics*, vol. 18, no. 5, pp. 1485–1497, 2012.

[29] R. V. Martinez, J. L. Branch, C. R. Fish, L. Jin, R. F. Shepherd, R. M. Nunes, Z. Suo, and G. M. Whitesides, "Robotic tentacles with three-dimensional mobility based on flexible elastomers," *Advanced Materials*, vol. 25, no. 2, pp. 205–212, 2013.

[30] C.-P. Chou and B. Hannaford, "Measurement and modeling of mckibben pneumatic artificial muscles," *IEEE Transactions on Robotics and Automation*, vol. 12, no. 1, pp. 90–102, 1996.

[31] T. Mirfakhrai, J. D. Madden, and R. H. Baughman, "Polymer artificial muscles," *Materials Today*, vol. 10, no. 4, pp. 30–38, 2007.

[32] M. Cianchetti, "Fundamentals on the use of shape memory alloys in soft robotics," *Interdisciplinary Mechatronics*, pp. 227–254, 2013.

[33] C. Laschi and M. Cianchetti, "Soft robotics: New perspectives for robot bodyware and control," *Frontiers in Bioengineering and Biotechnology*, vol. 2, p. 3, 2014.

[34] M. Bengisu and M. Ferrara, *Materials that Move: Smart Materials, Intelligent Design*. Springer, 2018.

[35] Z. Li, X. Zhang, G.-Y. Gu, X. Chen, and C.-Y. Su, "A comprehensive dynamic model for magnetostrictive actuators considering different input frequencies with mechanical loads," *IEEE Transactions on Industrial Informatics*, vol. 12, no. 3, pp. 980–990, 2016.

[36] N. Bira, P. Dhagat, and J. R. Davidson, "A review of magnetic elastomers and their role in soft robotics," *Frontiers in Robotics and AI*, vol. 7, p. 146, 2020.

[37] A. Benouhiba, K. Rabenorosoa, P. Rougeot, M. Ouisse, and N. Andreff, "A multisegment electro-active polymer based milli-continuum soft robots," in *2018 IEEE/RSJ International Conference on Intelligent Robots and Systems (IROS)*, pp. 7500–7506, IEEE, 2018.

[38] W.-B. Li, W.-M. Zhang, H.-X. Zou, Z.-K. Peng, and G. Meng, "A fast rolling soft robot driven by dielectric elastomer," *IEEE/ASME Transactions on Mechatronics*, vol. 23, no. 4, pp. 1630–1640, 2018.

[39] T. Guin, M. J. Settle, B. A. Kowalski, A. D. Auguste, R. V. Beblo, G. W. Reich, and T. J. White, "Layered liquid crystal elastomer actuators," *Nature Communications*, vol. 9, no. 1, pp. 1–7, 2018.

[40] Q. He, Z. Wang, Y. Wang, A. Minori, M. T. Tolley, and S. Cai, "Electrically controlled liquid crystal elastomer-based soft tubular actuator with multimodal actuation," *Science Advances*, vol. 5, no. 10, p. eaax5746, 2019.

[41] M. Wang, Z.-W. Cheng, B. Zuo, X.-M. Chen, S. Huang, and H. Yang, "Liquid crystal elastomer electric locomotives," *ACS Macro Letters*, vol. 9, no. 6, pp. 860–865, 2020.

[42] M. Duduta, D. R. Clarke, and R. J. Wood, "A high speed soft robot based on dielectric elastomer actuators," in *2017 IEEE International Conference on Robotics and Automation (ICRA)*, pp. 4346–4351, IEEE, 2017.

[43] C. Huang, J.-a. Lv, X. Tian, Y. Wang, Y. Yu, and J. Liu, "Miniaturized swimming soft robot with complex movement actuated and controlled by remote light signals," *Scientific Reports*, vol. 5, no. 1, pp. 1–8, 2015.

[44] H. Jin, E. Dong, M. Xu, C. Liu, G. Alici, and Y. Jie, "Soft and smart modular structures actuated by shape memory alloy (sma) wires as tentacles of soft robots," *Smart Materials and Structures*, vol. 25, no. 8, p. 085026, 2016.

[45] X. Tan and J. S. Baras, "Modeling and control of hysteresis in magnetostrictive actuators," *Automatica*, vol. 40, no. 9, pp. 1469–1480, 2004.

[46] P. Huang, J. Wu, P. Zhang, Y. Wang, and C.-Y. Su, "Dynamic modeling and tracking control for dielectric elastomer actuator with model predictive controller," *IEEE Transactions on Industrial Electronics*, 2021.

[47] Y. Bar-Cohen, *Electroactive Polymer (EAP) Actuators as Artificial Muscles: Reality, Potential, and Challenges*, vol. 136. SPIE Press Bellingham, WA, 2004.

[48] S. Qi, H. Guo, J. Fu, Y. Xie, M. Zhu, and M. Yu, "3d printed shape-programmable magneto-active soft matter for biomimetic applications," *Composites Science and Technology*, vol. 188, p. 107973, 2020.

[49] M. Warner and E. M. Terentjev, *Liquid Crystal Elastomers*, vol. 120. Oxford University Press, 2007.

[50] C. Ohm, M. Brehmer, and R. Zentel, "Liquid crystalline elastomers as actuators and sensors," *Advanced Materials*, vol. 22, no. 31, pp. 3366–3387, 2010.

[51] M. Rogóż, H. Zeng, C. Xuan, D. S. Wiersma, and P. Wasylczyk, "Light-driven soft robot mimics caterpillar locomotion in natural scale," *Advanced Optical Materials*, vol. 4, no. 11, pp. 1689–1694, 2016.

[52] V. Hassani, T. Tjahjowidodo, and T. N. Do, "A survey on hysteresis modeling, identification and control," *Mechanical Systems and Signal Processing*, vol. 49, no. 1-2, pp. 209–233, 2014.

[53] G. Bertotti, *Hysteresis in Magnetism: For Physicists, Materials Scientists, and Engineers*. Gulf Professional Publishing, 1998.

[54] R. A. Kerner and B. P. Rand, "Linking chemistry at the tio2/ch3nh3pbi3 interface to current-voltage hysteresis," *The Journal of Physical Chemistry Letters*, vol. 8, no. 10, pp. 2298–2303, 2017.

[55] D. Hughes and J. T. Wen, "Preisach modeling of piezoceramic and shape memory alloy hysteresis," *Smart Materials and Structures*, vol. 6, no. 3, p. 287, 1997.

[56] J. J. Tyson and B. Novak, "Regulation of the eukaryotic cell cycle: Molecular antagonism, hysteresis, and irreversible transitions," *Journal of Theoretical Biology*, vol. 210, no. 2, pp. 249–263, 2001.

[57] M. Göcke, "Various concepts of hysteresis applied in economics," *Journal of Economic Surveys*, vol. 16, no. 2, pp. 167–188, 2002.

[58] I. D. Mayergoyz, *Mathematical Models of Hysteresis and Their Applications*. Academic Press, 2003.

[59] J. Oh and D. S. Bernstein, "Semilinear duhem model for rate-independent and rate-dependent hysteresis," *IEEE Transactions on Automatic Control*, vol. 50, no. 5, p-p. 631–645, 2005.

[60] L. Ma, W. Li, Q. Wang, X. Zhang, Y. Jin, H. Huang, Y. Liu, Y. Yu, and Y. Ma, "Identification of the bouc-wen hysteresis model for piezoelectric actuated micro/nano electromechanical system," *Journal of Computational and Theoretical Nanoscience*, vol. 10, no. 4, pp. 983–988, 2013.

[61] G.-Y. Gu, L.-M. Zhu, C.-Y. Su, H. Ding, and S. Fatikow, "Modeling and control of piezo-actuated nanopositioning stages: A survey," *IEEE Transactions on Automation Science and Engineering*, vol. 13, no. 1, pp. 313–332, 2014.

[62] S.-L. Xie, H.-T. Liu, J.-P. Mei, and G.-Y. Gu, "Modeling and compensation of asymmetric hysteresis for pneumatic artificial muscles with a modified generalized prandtl-ishlinskii model," *Mechatronics*, vol. 52, pp. 49–57, 2018.

[63] J. C. Slaughter, M. J. Dapino, R. C. Smith, and A. B. Flatau, "Modeling of a terfenol-d ultrasonic transducer," in *Smart Structures and Materials 2000: Smart Structures and Integrated Systems*, vol. 3985, pp. 366–377, International Society for Optics and Photonics, 2000.

[64] Q.-Y. Liu, X. Luo, H.-Y. Zhu, Y.-W. Han, and J.-X. Liu, "Modeling plastic deformation effect on the hysteresis loops of ferromagnetic materials based on modified jiles-atherton model," *Acta Physica Sinica*, vol. 66, no. 10, p. 107501, 2017.

[65] R. C. Smith and Z. Ounaies, "A domain wall model for hysteresis in piezoelectric materials," *Journal of Intelligent Material Systems and Structures*, vol. 11, no. 1, pp. 62–79, 2000.

[66] W. J. Xu, N. N. Duan, S. H. Wang, Y. G. Guo, and J. G. Zhu, "Modeling the stress dependence of magnetic hysteresis based on stoner-wohlfarth theory," in *2015 IEEE International Conference on Applied Superconductivity and Electromagnetic Devices (ASEMD)*, pp. 378–379, IEEE, 2015.

[67] D. L. Atherton and J. Beattie, "A mean field stoner-wohlfarth hysteresis model," *IEEE Transactions on Magnetics*, vol. 26, no. 6, pp. 3059–3063, 1990.

[68] J. W. Macki, P. Nistri, and P. Zecca, "Mathematical models for hysteresis," *SIAM Review*, vol. 35, no. 1, pp. 94–123, 1993.

[69] G. Wang and G. Chen, "Identification of piezoelectric hysteresis by a novel duhem model based neural network," *Sensors and Actuators A: Physical*, vol. 264, pp. 282–288, 2017.

[70] M. Ismail, F. Ikhouane, and J. Rodellar, "The hysteresis bouc-wen model, a survey," *Archives of Computational Methods in Engineering*, vol. 16, no. 2, pp. 161–188, 2009.

[71] M. A. Krasnosel'skii and A. V. Pokrovskii, *Systems with Hysteresis*. Springer Science & Business Media, 2012.

[72] Z. Li, X. Zhang, C.-Y. Su, and T. Chai, "Nonlinear control of systems preceded by preisach hysteresis description: A prescribed adaptive control approach," *IEEE Transactions on Control Systems Technology*, vol. 24, no. 2, pp. 451–460, 2015.

[73] P.-B. Nguyen, S.-B. Choi, and B.-K. Song, "A new approach to hysteresis modelling for a piezoelectric actuator using preisach model and recursive method with an application to open-loop position tracking control," *Sensors and Actuators A: Physical*, vol. 270, pp. 136–152, 2018.

[74] M. Zhou, S. He, B. Hu, and Q. Zhang, "Modified kp model for hysteresis of magnetic shape memory alloy actuator," *IETE Technical Review*, vol. 32, no. 1, pp. 29–36, 2015.

[75] Y. Liu and M. Zhou, "Kp model for hysteresis of piezoelectric ceramic actuators," in *2015 Chinese Automation Congress (CAC)*, pp. 253–257, IEEE, 2015.

[76] A. Dargahi, S. Rakheja, and R. Sedaghati, "Development of a field dependent prandtl-ishlinskii model for magnetorheological elastomers," *Materials & Design*, vol. 166, p. 107608, 2019.

[77] S. Xie, J. Mei, H. Liu, and Y. Wang, "Hysteresis modeling and trajectory tracking control of the pneumatic muscle actuator using modified prandtl-ishlinskii model," *Mechanism and Machine Theory*, vol. 120, pp. 213–224, 2018.

[78] G. Tao and P. V. Kokotovic, "Adaptive control of plants with unknown hystereses," *IEEE Transactions on Automatic Control*, vol. 40, no. 2, pp. 200–212, 1995.

[79] Z. Li, X. Zhang, G.-Y. Gu, X. Chen, and C.-Y. Su, "A comprehensive dynamic model for magnetostrictive actuators considering different input frequencies with mechanical loads," *IEEE Transactions on Industrial Informatics*, vol. 12, no. 3, pp. 980–990, 2016.

[80] G. Tao and P. V. Kokotovic, "Adaptive control of plants with unknown hystereses," *IEEE Transactions on Automatic Control*, vol. 40, no. 2, pp. 200–212, 1995.

[81] X. Chen, T. Hisayama, and C.-Y. Su, "Pseudo-inverse-based adaptive control for uncertain discrete time systems preceded by hysteresis," *Automatica*, vol. 45, no. 2, pp. 469–476, 2009.

[82] Y. Li and Q. Xu, "Adaptive sliding mode control with perturbation estimation and pid sliding surface for motion tracking of a piezo-driven micromanipulator," *IEEE Transactions on Control Systems Technology*, vol. 18, no. 4, pp. 798–810, 2009.

[83] C.-Y. Su, Q. Wang, X. Chen, and S. Rakheja, "Adaptive variable structure control of a class of nonlinear systems with unknown prandtl-ishlinskii hysteresis," *IEEE Transactions on Automatic Control*, vol. 50, no. 12, pp. 2069–2074, 2005.

[84] X. Zhang, Y. Lin, and J. Wang, "High-gain observer based decentralised output feedback control for interconnected nonlinear systems with unknown hysteresis input," *International Journal of Control*, vol. 86, no. 6, pp. 1046–1059, 2013.

[85] X. Zhang and Y. Lin, "An adaptive output feedback dynamic surface control for a class of nonlinear systems with unknown backlash-like hysteresis," *Asian Journal of Control*, vol. 15, no. 2, pp. 489–500, 2013.

[86] R. B. Gorbet, K. A. Morris, and D. W. Wang, "Passivity-based stability and control of hysteresis in smart actuators," *IEEE Transactions on Control Systems Technology*, vol. 9, no. 1, pp. 5–16, 2001.

[87] S. Mittal and C.-H. Menq, "Hysteresis compensation in electromagnetic actuators through preisach model inversion," *IEEE/ASME Transactions on Mechatronics*, vol. 5, no. 4, pp. 394–409, 2000.

[88] Z. Li, C.-Y. Su, and T. Chai, "Compensation of hysteresis nonlinearity in magnetostrictive actuators with inverse multiplicative structure for preisach model," *IEEE Transactions on Automation Science and engineering*, vol. 11, no. 2, pp. 613–619, 2013.

[89] W. S. Galinaitis and R. C. Rogers, "Control of a hysteretic actuator using inverse hysteresis compensation," in *Smart Structures and Materials 1998: Mathematics and Control in Smart Structures*, vol. 3323, pp. 267–277, International Society for Optics and Photonics, 1998.

[90] S. Liu, C.-Y. Su, and Z. Li, "Robust adaptive inverse control of a class of nonlinear systems with prandtl-ishlinskii hysteresis model," *IEEE Transactions on Automatic Control*, vol. 59, no. 8, pp. 2170–2175, 2014.

[91] X. Tan and J. S. Baras, "Adaptive identification and control of hysteresis in smart materials," *IEEE Transactions on Automatic Control*, vol. 50, no. 6, pp. 827–839, 2005.

[92] C. Visone, "Hysteresis modelling and compensation for smart sensors and actuators," in *Journal of Physics: Conference Series*, vol. 138, p. 012028, IOP Publishing, 2008.

[93] M. Al Janaideh and P. Krejčí, "Inverse rate-dependent prandtl-ishlinskii model for feedforward compensation of hysteresis in a piezomicropositioning actuator," *IEEE/ASME Transactions on Mechatronics*, vol. 18, no. 5, pp. 1498–1507, 2012.

[94] J.-C. Shen, W.-Y. Jywe, H.-K. Chiang, and Y.-L. Shu, "Precision tracking control of a piezoelectric-actuated system," *Precision Engineering*, vol. 32, no. 2, pp. 71–78, 2008.

[95] M. Al Janaideh, S. Rakheja, and C.-Y. Su, "An analytical generalized prandtl-ishlinskii model inversion for hysteresis compensation in micropositioning control," *IEEE/ASME Transactions on Mechatronics*, vol. 16, no. 4, pp. 734–744, 2010.

[96] M. Al Janaideh, S. Rakheja, and C.-Y. Su, "A generalized prandtl-ishlinskii model for characterizing the hysteresis and saturation nonlinearities of smart actuators," *Smart Materials and Structures*, vol. 18, no. 4, p. 045001, 2009.

[97] S. Cao, B. Wang, J. Zheng, W. Huang, L. Weng, and W. Yan, "Hysteresis compensation for giant magnetostrictive actuators using dynamic recurrent neural network," *IEEE Transactions on Magnetics*, vol. 42, no. 4, pp. 1143–1146, 2006.

[98] B. K. Nguyen and K. K. Ahn, "Feedforward control of shape memory alloy actuators using fuzzy-based inverse preisach model," *IEEE Transactions on Control Systems Technology*, vol. 17, no. 2, pp. 434–441, 2008.

[99] Y. Cao, L. Cheng, X. Chen, and J. Peng, "An inversion-based model predictive control with an integral-of-error state variable for piezoelectric actuators," *IEEE/ASME Transactions on Mechatronics*, vol. 18, no. 3, pp. 895–904, 2012.

[100] X. Zhang, Z. Li, C.-Y. Su, Y. Lin, and Y. Fu, "Implementable adaptive inverse control of hysteretic systems via output feedback with application to piezoelectric positioning stages," *IEEE Transactions on Industrial Electronics*, vol. 63, no. 9, pp. 5733–5743, 2016.

[101] X. Lu, H. Zhang, G. Fei, B. Yu, X. Tong, H. Xia, and Y. Zhao, "Liquid-crystalline dynamic networks doped with gold nanorods showing enhanced photocontrol of actuation," *Advanced Materials*, vol. 30, no. 14, p. 1706597, 2018.

[102] O. M. Wani, H. Zeng, and A. Priimagi, "A light-driven artificial flytrap," *Nature Communications*, vol. 8, no. 1, pp. 1–7, 2017.

[103] X. Lu, S. Guo, X. Tong, H. Xia, and Y. Zhao, "Tunable photocontrolled motions using stored strain energy in malleable azobenzene liquid crystalline polymer actuators," *Advanced Materials*, vol. 29, no. 28, p. 1606467, 2017.

[104] C. Ahn, X. Liang, and S. Cai, "Bioinspired design of light-powered crawling, squeezing, and jumping untethered soft robot," *Advanced Materials Technologies*, vol. 4, no. 7, p. 1900185, 2019.

[105] Y. Zhang, C. Xuan, Y. Jiang, and Y. Huo, "Continuum mechanical modeling of liquid crystal elastomers as dissipative ordered solids," *Journal of the Mechanics and Physics of Solids*, vol. 126, pp. 285–303, 2019.

[106] J. Wu, W. Ye, Y. Wang, and C.-Y. Su, "Modeling of photo-responsive liquid crystal elastomer actuators," *Information Sciences*, vol. 560, pp. 441–455, 2021.

[107] R. L. Selinger, B. L. Mbanga, and J. V. Selinger, "Modeling liquid crystal elastomers: Actuators, pumps, and robots," in *Emerging Liquid Crystal Technologies III*, vol. 6911, p. 69110A, International Society for Optics and Photonics, 2008.

[108] A. Konya, V. Gimenez-Pinto, and R. L. Selinger, "Modeling defects, shape evolution, and programmed auto-origami in liquid crystal elastomers," *Frontiers in Materials*, vol. 3, p. 24, 2016.

[109] M.-H. Li and P. Keller, "Artificial muscles based on liquid crystal elastomers," *Philosophical Transactions of the Royal Society A: Mathematical, Physical and Engineering Sciences*, vol. 364, no. 1847, pp. 2763–2777, 2006.

[110] W. Greiner, L. Neise, and H. Stöcker, *Thermodynamics and Statistical Mechanics*. Springer Science & Business Media, 2012.

[111] J. Wu, J. Wang, and Z. You, "An overview of dynamic parameter identification of robots," *Robotics and Computer-Integrated Manufacturing*, vol. 26, no. 5, pp. 414–419, 2010.

[112] J. Jin and N. Gans, "Parameter identification for industrial robots with a fast and robust trajectory design approach," *Robotics and Computer-Integrated Manufacturing*, vol. 31, pp. 21–29, 2015.

[113] S. N. Kumpati, P. Kannan, *et al.*, "Identification and control of dynamical systems using neural networks," *IEEE Transactions on Neural Networks*, vol. 1, no. 1, pp. 4–27, 1990.

[114] J. Wu, W. Ye, Y. Wang, and C.-Y. Su, "A general position control method for planar underactuated manipulators with second-order nonholonomic constraints," *IEEE Transactions on Cybernetics*, vol. 51, no. 9, pp. 4733-4742, 2021.

[115] P. C. Hansen, V. Pereyra, and G. Scherer, *Least Squares Data Fitting with Applications*. JHU Press, 2013.

[116] S. Gratton, A. S. Lawless, and N. K. Nichols, "Approximate gauss-newton methods for nonlinear least squares problems," *SIAM Journal on Optimization*, vol. 18, no. 1, pp. 106–132, 2007.

[117] R. Arablouei, S. Werner, and K. Doğançay, "Analysis of the gradient-descent total least-squares adaptive filtering algorithm," *IEEE Transactions on Signal Processing*, vol. 62, no. 5, pp. 1256–1264, 2014.

[118] A. Ranganathan, "The levenberg-marquardt algorithm," *Tutoral on LM Algorithm*, vol. 11, no. 1, pp. 101–110, 2004.

[119] S. Liu, C.-Y. Su, and Z. Li, "Robust adaptive inverse control of a class of nonlinear systems with prandtl-ishlinskii hysteresis model," *IEEE Transactions on Automatic Control*, vol. 59, no. 8, pp. 2170–2175, 2014.

[120] J. Zhou, C. Wen, and T. Li, "Adaptive output feedback control of uncertain nonlinear systems with hysteresis nonlinearity," *IEEE Transactions on Automatic Control*, vol. 57, no. 10, pp. 2627–2633, 2012.

[121] Y. Yang, X. Cheng, J. Cheng, D. Jiang, and S. Li, "Improved alopex-based evolutionary algorithm by gaussian copula estimation of distribution algorithm and its application to the butterworth filter design," *International Journal of Systems Science*, vol. 49, pp. 160–178, 2018.

[122] Z. D. Milosavljevic, "Design of generalized chebyshev filters with asymmetrically located transmission zeros," *IEEE Transactions on Microwave Theory and Techniques*, vol. 53, no. 7, pp. 2411–2415, 2005.

[123] V. Utkin, "Discussion aspects of high-order sliding mode control," *IEEE Transactions on Automatic Control*, vol. 61, no. 3, pp. 829–833, 2015.

[124] S. I. Islam, C. Lim, and P. Shi, "Functional observer-based fuzzy controller design for continuous nonlinear systems," *International Journal of Systems Science*, vol. 49, pp. 1047 – 1060, 2018.

[125] Y. Su and C. Zheng, "Pid control for global finite-time regulation of robotic manipulators," *International Journal of Systems Science*, vol. 48, no. 3, pp. 547–558, 2017.

[126] Y. Chu, J. Fei, and S. Hou, "Adaptive global sliding-mode control for dynamic systems using double hidden layer recurrent neural network structure," *IEEE Transactions on Neural Networks and Learning Systems*, vol. 31, no. 4, pp. 1297–1309, 2019.

[127] H.-T. Hsu, H.-W. Yao, K. A. Zaki, and A. E. Atia, "Computer-aided diagnosis and tuning of cascaded coupled resonators filters," *IEEE Transactions on Microwave Theory and Techniques*, vol. 50, no. 4, pp. 1137–1145, 2002.

[128] G. D. Mitsis, M. G. Markakis, and V. Z. Marmarelis, "Nonlinear modeling of the dynamic effects of infused insulin on glucose: Comparison of compartmental with volterra models," *IEEE Transactions on Biomedical Engineering*, vol. 56, no. 10, pp. 2347–2358, 2009.

[129] Z. Xiao, X. Jing, and L. Cheng, "Parameterized convergence bounds for volterra series expansion of narx models," *IEEE Transactions on Signal Processing*, vol. 61, no. 20, pp. 5026–5038, 2013.

[130] K. Hammar, T. Djamah, and M. Bettayeb, "Nonlinear system identification using fractional hammerstein-wiener models," *Nonlinear Dynamics*, vol. 98, pp. 2327–2338, 2019.

[131] T. F. Coleman and Y. Y. Li, "An interior trust region approach for nonlinear minimization subject to bounds," *SIAM Journal on Optimization*, vol. 6, no. 2, pp. 418–445, 1996.

[132] C. Li, Y. Liu, X. Huang, and H. Jiang, "Direct sun-driven artificial heliotropism for solar energy harvesting based on a photothermomechanical liquid-crystal elastomer nanocomposite," *Advanced Functional Materials*, vol. 22, no. 24, pp. 5166–5174, 2012.

[133] H. Zeng, O. M. Wani, P. Wasylczyk, and A. Priimagi, "Light-driven, caterpillar-inspired miniature inching robot," *Macromolecular Rapid Communications*, vol. 39, no. 1, p. 1700224, 2018.

[134] M. Rogóż, K. Dradrach, C. Xuan, and P. Wasylczyk, "A millimeter-scale snail robot based on a light-powered liquid crystal elastomer continuous actuator," *Macromolecular Rapid Communications*, vol. 40, no. 16, p. 1900279, 2019.

[135] M. Yamada, M. Kondo, R. Miyasato, Y. Naka, J.-i. Mamiya, M. Kinoshita, A. Shishido, Y. Yu, C. J. Barrett, and T. Ikeda, "Photomobile polymer materials-various three-dimensional movements," *Journal of Materials Chemistry*, vol. 19, no. 1, pp. 60–62, 2009.

[136] Y. Yan, Y. Zhao, Y. Alsaid, B. Yao, Y. Zhang, S. Wu, and X. He, "Artificial phototropic systems for enhanced light harvesting based on a liquid crystal elastomer," *Advanced Intelligent Systems*, p. 2000234, 2021.

[137] H. Zeng, O. M. Wani, P. Wasylczyk, R. Kaczmarek, and A. Priimagi, "Self-regulating iris based on light-actuated liquid crystal elastomer," *Advanced Materials*, vol. 29, no. 30, p. 1701814, 2017.